ChemSusChem

Review
doi.org/10.1002/cssc.202501366

Chemistry Europe
European Chemical Societies Publishing

www.chemsuschem.org

Recent Advances in Microenvironment Engineering for Selective Electrochemical C–N Coupling

Jianping Bai, Xinhai Cai, Xin Liu, Nirala Singh,* and Libo Yao*

Electrochemical C–N coupling via the coreduction of CO_2 and nitrogenous species (N_2/NO_x) presents a sustainable route to synthesize value-added C–N compounds under mild conditions. However, competing pathways and mismatched intermediate kinetics hinder the selective formation of products like urea, amines, and amides. Recent advances reveal that rational modulation of the electrochemical microenvironment can effectively steer reaction pathways and stabilize coupling-relevant intermediates. This review systematically summarizes how microenvironment engineering, originally developed for CO_2 and NO_x reduction reactions, can be leveraged to enhance C–N coupling efficiency and selectivity. The key strategies are categorized into 1) catalyst-centered design (e.g., ligand coordination, defect engineering, and morphology control), 2) ionic and electrolyte modifications (e.g., cation/pH effects), and 3) dynamic approaches such as pulsed electrolysis. These methods shape local fields, surface coverage, and mass transport properties, ultimately directing reactants toward cross-coupling over competing routes. By drawing parallels with well-established CO_2RR/NO_xRR systems and showcasing emerging examples in C–N coupling, the central role of microenvironment control is highlighted. Finally, a perspectives on strategies to further improve activity, selectivity, and atom economy in future C–N coupling systems are offered.

1. Introduction

Carbon dioxide (CO_2) from human activities is a leading driver of climate change, causing global warming and widespread ecological disruptions.[1,2] Meanwhile, reactive nitrogen species like nitrate (NO_3^-) and nitrite (NO_2^-) from agricultural runoff and/or industrial effluents contaminate water resources, leading to eutrophication and biodiversity loss.[3] Due to the severity of these environmental threats, advanced strategies are critically needed to simultaneously reduce carbon and nitrogen pollutants. One promising approach is to convert these waste compounds into useful products, both mitigating their impact and repurposing them as valuable resources.[4] This can be achieved through electrochemical C–N coupling, which offers a sustainable and environmentally friendly alternative to traditional methods. Unlike conventional processes to form C–N compounds—such as producing urea through high-temperature, high-pressure reactions between CO_2 and ammonia, or using toxic reagents—the electrochemical C–N coupling reaction operates at mild conditions and can be driven by renewable electricity.[5,6] This method provides a more sustainable and environmentally friendly pathway for producing C–N chemicals.[7]

Research in electrochemical C–N coupling has advanced rapidly in recent years, building on the extensive knowledge base from the electrochemical CO_2 reduction reaction (CO_2RR) and nitrogen reduction (nitrogen oxides and N_2 reduction reactions).[8,9] Significant progress has been made in elucidating possible coupling mechanisms, developing efficient catalysts, and demonstrating the electrosynthesis of diverse C–N products. Nevertheless, forming a C—N bond via coreduction of CO_2 and a nitrogen species involves three intertwined pathways (the CO_2RR, the N-species reduction, and the C–N coupling step itself) and the concerted transfer of multiple protons and electrons involving C, N, O, and H atoms.[10,11] Taking urea ($CO(NH_2)_2$) synthesis as an example, theoretical and experimental studies have proposed many possible coupling routes, and the exact pathway depends on the nitrogen feed (e.g., N_2 vs. NO_x), as well as the catalyst.[7,12]

However, in practice, when CO_2 and a nitrogen source are coreduced, each tends to undergo its own individual reduction pathways, and only a fraction of the generated intermediates end up in the cross-coupling route.[13,14] This competition results in low yields and energy efficiency for the desired C–N products.[15,16] Addressing this issue requires reaction systems that favor the C—N bond-forming pathway over the competing routes.[17] One approach is the design of catalysts that selectively stabilize the key C–N coupling intermediates and lower the barrier for their combination, thereby channeling more of the reactants toward the C–N product.[18,19]

In addition to catalyst design, another emerging strategy to enhance C–N coupling outcomes is the modulation of the

J. Bai, X. Cai, L. Yao
National Key Laboratory of Materials-Oriented Chemical Engineering
College of Chemical Engineering
Nanjing Tech University
Nanjing 211816, China
E-mail: yaolibo915@njtech.edu.cn

X. Liu
Department of Chemistry
Colorado State University
Fort Collins, Colorado 80523, USA

N. Singh
Department of Chemical Engineering
University of Michigan
Ann Arbor, Michigan 48109, USA
E-mail: snirala@umich.edu

electrochemical microenvironment.[20] In electrochemistry, the term "microenvironment" refers to the local conditions in the vicinity of the catalyst's active sites. Tuning this microenvironment can significantly influence reaction pathways, the stability of intermediates, and overall product selectivity. Notably, in CO_2RR and NO_x reduction reaction (NO_xRR), microenvironment engineering has enabled greater control over product distributions and improved catalytic activity/stability by optimizing local pH, reactant availability, and ion gradients near the electrode.[21,22] By contrast, the role of microenvironment in C–N coupling remains relatively unexplored. Learning how to manipulate the local reaction environment to stabilize cross-coupling intermediates, mitigate side reactions, and promote C—N bond formation could unlock new opportunities for efficient electrosynthesis of C–N products, and is a central theme of current research.

In this review, we survey recent progress in understanding and controlling the electrochemical microenvironment for C–N coupling reactions. We begin by outlining the fundamental aspects of electrochemical C–N coupling, including the key reactants, intermediate species, products, and reaction pathways involved. The influence of various microenvironmental factors at the electrode interface on the electrochemical processes at the interface is then summarized. We then highlight recent advances in actively modulating the microenvironment to improve C–N coupling performance, focusing on three primary approaches: 1) catalyst-centered design (which intrinsically shapes the electronic properties of active sites), 2) electrolyte/ionic modifications (which tailor the local electrolyte environment), and 3) pulsed electrolysis (PE) (which dynamically tunes local concentrations). For each strategy, we discuss representative examples of how microenvironment tuning can suppress competing reactions and steer the system toward the desired C–N products, drawing on lessons from CO_2RR and NO_3RR where applicable. Finally, we emphasize the pivotal role of microenvironment control in advancing electrochemical C–N coupling technology and propose future research directions to address remaining challenges.

2. Fundamental Aspects of Electrochemical C–N Coupling Reaction

The reaction pathways of electrochemical C–N coupling reactions involve several key steps. In a typical C–N coupling process, the choice of the nitrogen source is crucial, as it largely determines the reaction pathway and the final products.[23] Common inorganic nitrogen sources include N_2 and gaseous and aqueous NO_x. Given the complex reaction network and numerous possible

Jianping Bai is a master's candidate in the College of Chemical Engineering at Nanjing Tech University. In 2023, joined Prof. Libo Yao's research group to conduct systematic investigations into the electrocatalytic nitrate reduction and C–N coupling. Her research focuses on the electroreduction of CO_2 and nitrate to the synthesis of high-value C–N products, while leveraging pulsed electrolysis protocols to dynamically regulate reaction kinetics in nitrate reduction and C–N coupling steps.

Xinhai Cai is a master's student at the College of Chemical Engineering at Nanjing Tech University, class of 2023. His primary research interests lie in the design of electrocatalytic microenvironments, with a particular focus on achieving high selectivity in C—N bond formation through cross-coupling methods, as well as utilizing functional polymer materials to regulate reaction kinetics and interfacial processes in electrocatalytic CO_2RR.

Xin Liu has a interdisciplinary research background in organometallic chemistry, photocatalysis, and polymer synthesis. After earning his master's degree with distinction in 2017 in China, he joined the group of Prof. Thomas Werner and Johannes G. de Vries at the Leibniz Institute for Catalysis (LIKAT) in Germany, where he focused on 3*d* metal-catalyzed transformations. In January 2022, he joined Prof. Garret Miyake's research group at Colorado State University, where his research endeavors have expanded to the design of organic photoredox catalysts, the development of recyclable polymers, the upcycling of waste polymers into high-value materials.

Nirala Singh received his B.S. in chemical engineering from the University of Michigan and Ph.D. from the University of California at Santa Barbara in 2015. He was a Washington Research Foundation Innovation Fellow at the University of Washington and the Pacific Northwest National Laboratory before joining the faculty of the University of Michigan. He is currently an associate professor at the University of Michigan in chemical engineering. His research focuses on understanding electrochemical and electrocatalytic processes, including nitrate reduction, carbon dioxide reduction, biomass upgrading, water electrolysis, and research in energy storage using flow batteries.

Libo Yao received his bachelor's (2014) and master's (2017) degrees in chemical engineering from China University of Petroleum, and his Ph.D. from the University of Akron (2021). From 2021 to 2024, he was a postdoctoral fellow at the Department of Chemical Engineering and Department of Chemistry in University of Michigan. He is now a professor at the College of Chemical Engineering and State Key Laboratory of Materials-Oriented Chemical Engineering at Nanjing Tech University. His research focuses on electrocatalysis and electrosynthesis, energy conversion, and electrochemical engineering.

products, we categorize C–N products into either multinitrogen C–N products or single nitrogen atom C–N products.[24,25]

2.1. Multinitrogen C–N Products

Urea stands as the sole multinitrogen product produced solely via electrochemical catalysis to date, and its formation requires the creation of two C—N bonds. CO_2 must first be electrochemically activated to form a reduced carbon intermediate. The types of adsorbed nitrogen intermediates that couple with the carbon intermediate are dependent on the nitrogen source.[26] When N_2 serves as the nitrogen source, the N≡N bond predominantly undergoes direct C–N coupling without complete dissociation in a single step. In contrast, NO_x species typically participate in stepwise coupling mechanisms involving sequential bond formation steps (**Table 1**).[27]

2.1.1. N_2 as a Nitrogen Source (Nitrogen Reduction Reaction (NRR) Pathway)

When N_2 is used as the nitrogen source, the reaction mechanism inherits the challenges of the sluggish NRR: the N≡N triple bond is very inert and difficult to break. On typical catalysts, N_2 adsorption is weak, and electrochemical N_2 reduction tends to proceed via an associative mechanism, in which N_2 is incrementally hydrogenated without fully dissociating.[7] For C–N coupling to produce urea in this case, at least one of the N atoms from N_2 must couple with a carbon intermediate before being fully reduced to NH_3. Currently, four possible coupling paths are proposed (**Figure 1**).[28] It is worth noting that the N_2 route to urea is typically difficult: N_2 activation requires high overpotentials and competing formation of NH_3 often predominates, resulting in low selectivity and yield for urea in most reported attempts. These challenges motivate the exploration of alternative nitrogen sources for C–N coupling.

Table 1. Comparison of the mechanistic difference for urea production from N_2 and NO_x.

Nitrogen source	Distinction
N_2	N≡N undergoes direct C–N coupling without complete dissociation (predominantly)
NO_x	Stepwise coupling

2.1.2. NO_x as a Nitrogen Source

Using nitrogen oxide sources like nitrate (NO_3^-), nitrite (NO_2^-), or nitric oxide (NO) significantly alters the reaction pathways for C–N coupling. In the context of urea formation from CO_2 and NO (**Figure 2**a), one proposed mechanism involves a stepwise coupling of two nitrogen intermediates with one carbon intermediate.[29] The *CO can couple with an *NH_2 intermediate (derived from NO) to form an *NH_2CO. This species then incorporates a second *NH_2 (or related N-containing intermediate) to form a dinitrogen carbonaceous intermediate. In alternate pathways, an *NH_2–*NH_2 intermediate from NO could directly couple with *CO to form *NH_2CONH_2 and progresses to urea. In the process of CO_2 and NO_2^- or NO_3^- forming urea, the current mechanism involves the initial coupling of *CO or *COOH with *NO_2, *NO, *NH, or *NH_2 to form *OCNO, *HNCO, *NO_2CO, *NO_2CO_2, *NH_2CO, or *NH_2COOH coupling intermediates, which are then

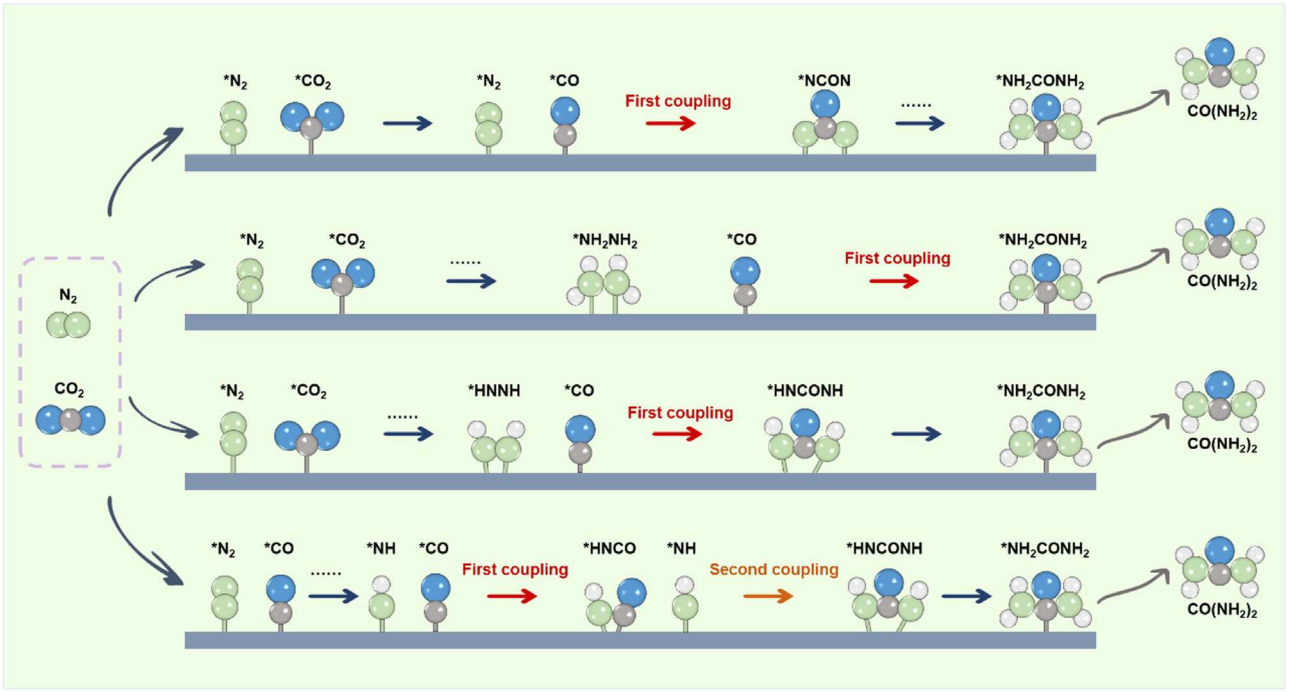

Figure 1. Schematic illustration of reaction pathways for urea production from CO_2 and N_2. C–N coupling steps are labeled.

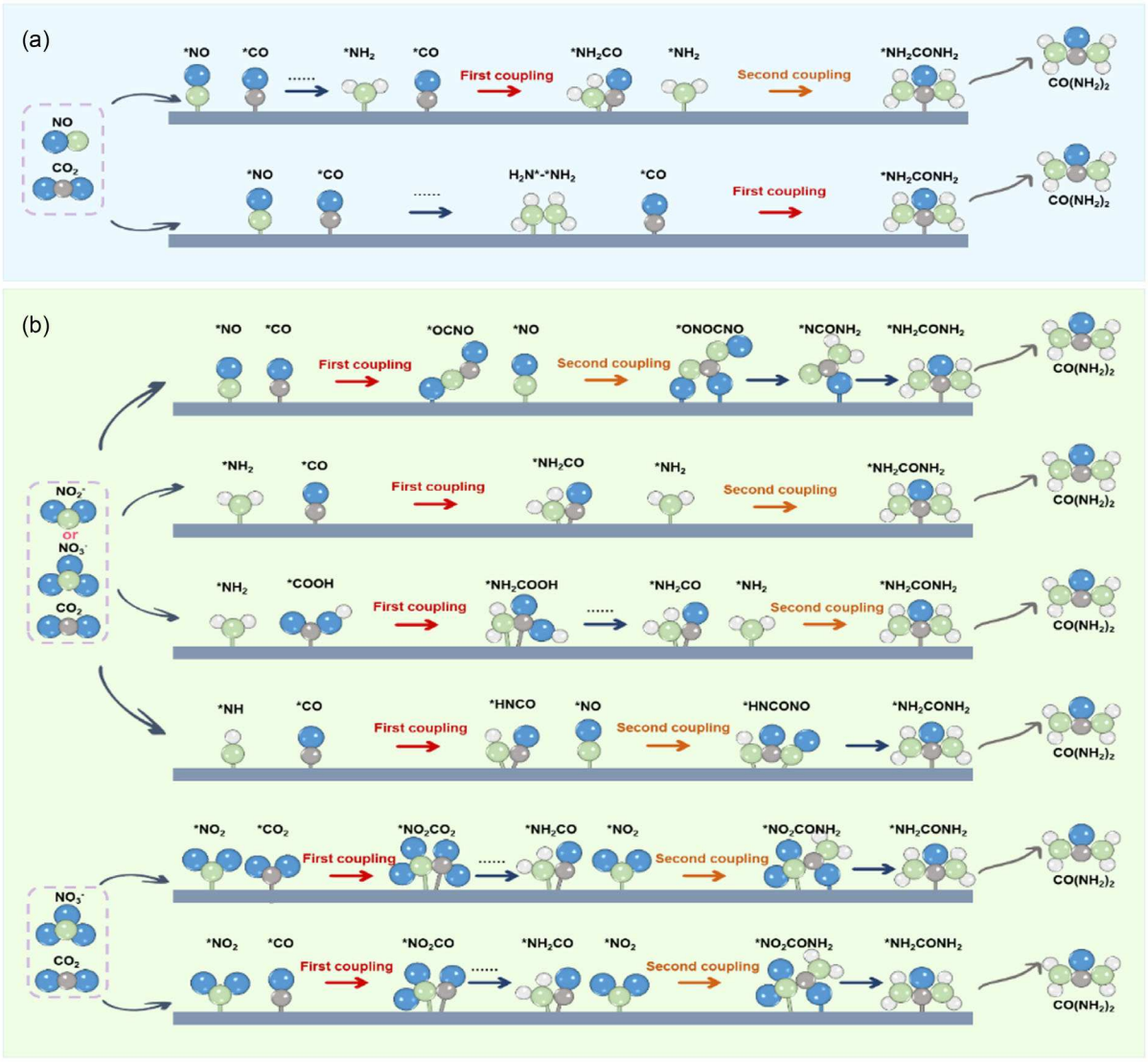

Figure 2. Schematic illustration of reaction pathways for urea production from NO_x species. a) NO; and b) NO_2^- and NO_3^-.

coupled to form $*NH_2CONH_2$ (Figure 2b).[18,30–32] The key distinction for NO_x-derived nitrogen is that the N—O bonds in NO_3^- are easier to break than the N≡N bond in N_2. As a result, experimentally, the coreduction of CO_2 with nitrates or nitrites tends to achieve higher C–N coupling efficiencies than the CO_2–N_2 system, but requires careful control to avoid over-reduction of nitrogen to ammonia or dinitrogen.

2.2. One-Nitrogen C–N Products (Amides and Amines)

Many valuable chemicals, such as amides or amines, contain a single C—N bond. The electrochemical formation of these products from CO_2 and a nitrogen source follows a similar principle of coupling surface intermediates as seen with urea, but only one-nitrogen-containing intermediate is needed per product molecule.[33] For example, formamide can be generated if an $*NH_2$ species couples with a carbon intermediate like *CO on the surface, forming an adsorbed $*CONH_2$ species that then desorbs as methylamine ($HCONH_2$) (**Figure 3**a). However, CO_2 and NO_3^- can also undergo independent electrochemical reduction, leading to the formation of NH_2OH and the carbonyl intermediate HCHO; these then couple to form formaldoxime ($*CH_2NOH$), which is subsequently reduced to *N*-methylhydroxylamine ($*CH_3NHOH$) and finally reduced to methylamine (Figure 3a).[34] A similar reaction pathway also leads to the production of ethylamine (Figure 3b). Formamide might form via the coupling of an $*NH_2$ with an *CHO or *CO intermediate (Figure 3c).[35,36] Acetamide could analogously originate from coupling an $*NH_2OH$ with a $*CH_3CHO$ intermediate (Figure 3d).[37] In practice, achieving high selectivity to a specific single-N product is challenging because it often requires balancing the degree of reduction of the carbon intermediate with that of the nitrogen intermediate. Thus, understanding and controlling the mechanistic details (which intermediate is present and when) is key to selectively synthesizing one-nitrogen C–N products.

In summary, the mechanism of electrochemical C–N coupling is a multifaceted interplay between CO_2 reduction and nitrogen-

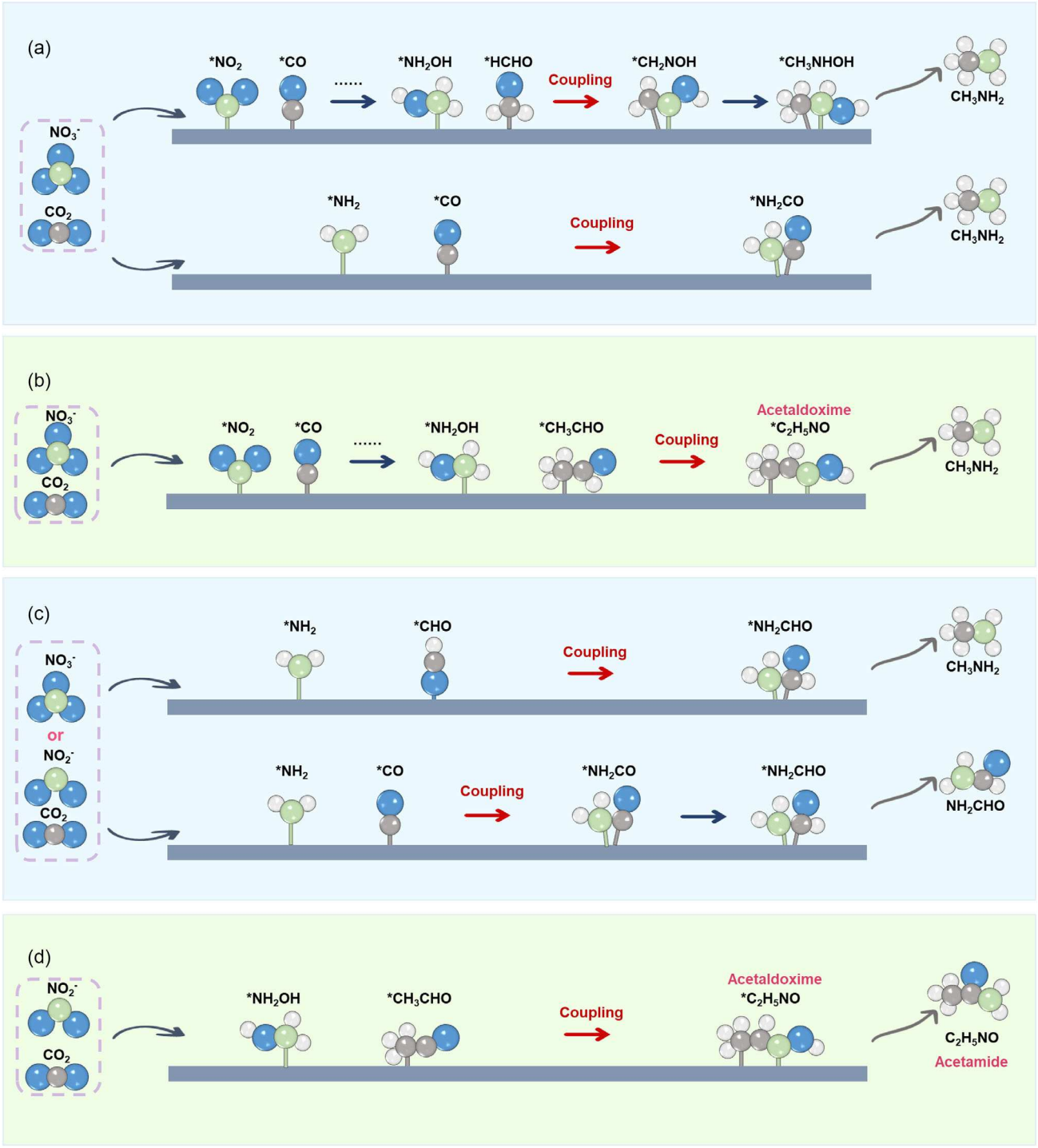

Figure 3. Schematic of mechanisms of CO_2 and NO_x reduction to form a) methylamine, b) ethylamine, c) formamide, and d) acetamide.

species reduction pathways. There are numerous possible routes for C—N bond formation, especially for complex products. This complexity contributes to the difficulty in attaining high yields and selectivities for C–N coupled products unless carefully directed. Subtle changes in local conditions can tip the balance toward the desired C–N coupling route or, conversely, toward competing reactions. In the next section, we discuss how the microenvironment plays a crucial role in steering these pathways.

3. Fundamentals of the Electrochemical Microenvironment and Its Influence on Interfacial Reactions

The electrochemical microenvironment refers to the local physical and chemical conditions at the electrode–electrolyte interface in the immediate vicinity of the catalyst's active sites.[38,39] This includes features of the catalyst as well as those in the local

electrolyte. The microenvironment can deviate significantly from bulk conditions; therefore, it imposes a significant influence on the reaction mechanism and catalytic performance.[40] Below, we illustrate how different features modulate the microenvironment and subsequently the electrochemical reactions.

3.1. Catalysts

From the perspective of the catalyst, the microenvironment consists of the composition and structure of the catalytic surface.[41] The specific defect sites and morphology will determine how reactant molecules adsorb and which intermediate species are stabilized.[42,43] The catalyst's intrinsic environment also includes any nearby ligands or functional groups, which tune the electronic property of active sites.[27] A catalyst support that is hydrophobic can raise the local pH at the interface and suppress the hydrogen evolution reaction (HER). Through these effects, the catalyst can modulate the microenvironment in a way that promotes certain reaction pathways that can be tuned to enhance C–N coupling selectivity and efficiency by stabilizing desired intermediates and deterring side reactions.[43,44]

3.2. Local Electrolyte

The electrolyte immediately adjacent to the catalyst is also part of the microenvironment.[45] This includes local pH, the distribution of ions, and the concentration gradients of reactants and products in the diffusion layer.[46] All of these can dramatically impact reaction kinetics and selectivity. Higher local pH values tend to promote the production of key intermediates.[47] Besides proton concentration, the types of cations in the electrolyte (e.g., Li^+, Na^+, K^+, Cs^+, or organic cations) influence the microenvironment via the electric double layer (EDL).[48,49] Cations in electrolyte enhance reaction kinetics and inhibit HER by adjusting the interface electric field and lowering the activation energy barrier. Such cation effects are well-documented in CO_2RR, and since the carbon sources are the same, the relevant conclusions can provide guidance for C–N coupling systems.[50] Thus, adjusting the electrolyte composition allows one to engineer the interfacial environment in favor of C—N bond formation.

3.3. PE

Besides directly controlling the catalyst and electrolyte, PE dynamically regulates both simultaneously. Through periodic potential switching, it induces reversible changes to catalyst surface properties while dynamically adjusting local pH, reactant, and intermediate concentrations in the microenvironment.

The interplay between features of the catalyst and local electrolyte microenvironment factors ultimately dictates the course of the electrochemical reaction at the interface.[51] Rationally modulating the microenvironment has therefore become an important approach to improve C–N coupling performance. In the following sections, we will discuss how catalyst design can create an inherently favorable environment for coupling, how ionic/electrolytic modifications can suppress side reactions like HER, and how PE can dynamically alter local conditions to enhance C–N bond formation.

4. Tailoring Microenvironment Through Catalyst Design

Catalysts create a local microenvironment that directly governs reaction activity and selectivity.[40,52,53] The catalytic phenomena within the microenvironment are jointly shaped by the interplay of electronic effects regulating reactant adsorption and activation, defect engineering influencing charge distribution, and morphological optimization enhancing mass transport and active site exposure.[54,55] These factors are intrinsically intertwined, collectively defining an efficient reaction microenvironment.[56] We first review applications for CO_2RR and NO_3RR separately, then C–N coupling.

4.1. Catalyst Design for CO_2RR or NO_xRR

The C–N coupling originates from CO_2RR and NO_3RR. As there exist significant parallels between C–N coupling, CO_2RR, and NO_3RR, insights gained from CO_2RR and NO_3RR demonstrate clear relevance for advancing C–N coupling processes.[57] Significant progress has been made in designing and optimizing catalyst microenvironments for CO_2RR and NO_3RR.[58] This section explores how tuning electronic properties, introducing defects, and controlling catalyst morphology and interfaces can address key challenges in CO_2RR and NO_3RR, ultimately improving activity and selectivity.

4.1.1. Ligand Engineering: Tuning Electronic Structures

Because the electronic properties of active sites dictate intermediate binding strengths and reaction pathway selectivity, tuning a catalyst's coordination environment or electronic state can steer reactions toward desired products. Adjusting the coordination structure of active metal centers optimizes their electronic configuration and can improve the catalyst's performance and atomic utilization efficiency.[59]

In CO_2RR, introducing coordination structures modulates the electronic structure, thereby tailoring the active centers and accelerating the formation of intermediates.[20,60] Pan et al. anchored Co single atoms on polymer-derived hollow N-doped porous carbon spheres (HNPCSs) rich in nitrogen coordination sites, creating a Co–N_5/HNPCSs catalyst (**Figure 4**a).[61] X-ray absorption near edge structure (XANES) and Extended x-ray absorption fine structure (EXAFS) analysis confirmed that the Co K-edge absorption of Co–N_5/HNPCSs lies between those of CoO and Co_3O_4, indicating an average Co oxidation state between $+2$ and $+3$ (Figure 4b), confirming the presence of Co–N coordination structures. As a result, Co–N_5/HNPCSs used for CO_2RR achieved a CO Faradaic efficiency (FE_{CO}) of 99.4% at -0.79 V, about 15.5 times higher than a CoPc molecular catalyst

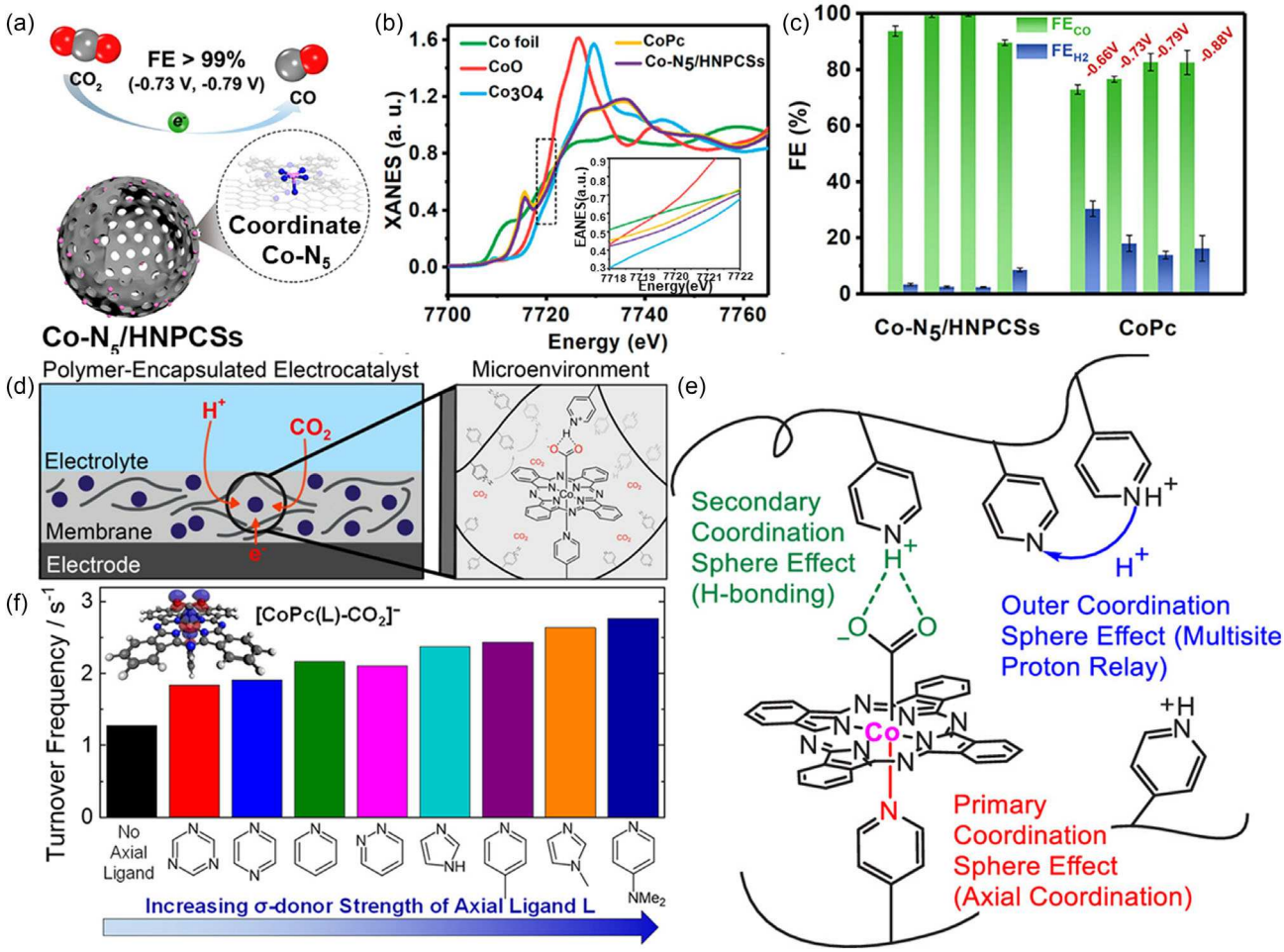

Figure 4. a) Simulated structure of Co–N_5/HNPCSs and its FE_{CO}. b) Co K-edge XANES spectra for Co–N_5/HNPCSs. c) FE_{CO} and FE_{H2} on Co–N_5/HNPCSs and CoPc. Reproduced with permission.[61] Copyright 2018, American Chemical Society. d) Schematic of a CoPc catalyst embedded in a P4VP polymer and the effect on microenvironment. Reproduced with permission.[66] Copyright 2022, American Chemical Society. e) Illustration of types of coordination effects on CoPc. f) Turnover frequencies of CoPc with axial ligands of different σ-donor strength. Reproduced with permission.[67] Copyright 2021, American Chemical Society.

under the same conditions (Figure 4c). To probe the role of coordination, the Co–N_5/HNPCSs catalyst was pyrolyzed at increasing temperatures, which progressively weakened the Co–N_5 coordination and led to a gradual decline in FE_{CO}. This confirms that the Co–N_5 coordination structure serves as the active center for CO_2 activation, promoting rapid formation of the *COOH intermediate and facilitating CO desorption.[62]

Rational modulation of a metal's coordination environment can thus alter its electronic structure and intermediate adsorption behavior.[63,64] For example, when CoPc is immobilized on an edge-plane graphite electrode, it shows limited CO_2 reduction activity and selectivity, with substantial hydrogen evolution. McCrory and coworkers dramatically improved the CO_2RR performance of CoPc by embedding it in a poly(4-vinylpyridine) (P4VP) film (Figure 4d).[65] The CoPc–P4VP electrode achieved ≈90% FE_{CO} and a turnover frequency of 4.8 s^{-1} at −0.75 V versus Reversible Hydrogen Electrode (RHE). This remarkable improvement is attributed to the dual role of the P4VP matrix, its pyridine units axially coordinate to the Co center, strengthening CO_2 binding, while uncoordinated pyridines create a secondary coordination sphere that facilitates proton transfer (Figure 4e).[66] Axial coordination strength is closely correlated with the CO conversion frequency; as the coordination strength increases, the CO conversion frequency rises accordingly (Figure 4f). Both experiments and Density Functional Theory (DFT) calculations confirmed that axial ligands lead to higher catalytic currents and improved CO selectivity, increasing the FE_{CO} from ≈60% to ≈70%.[67]

Introducing axial ligands can also break the symmetry of active sites and perturb the electron density distribution, thereby promoting intermediate adsorption and accelerating kinetics, an effect particularly notable in NO_3RR.[68,69] For example, Wan et al. incorporated an axial chlorine ligand into was added to the nitrogen-doped carbon an Fe single-atom catalyst (Cl–Fe–NC) to break the symmetry of the Fe–N_4 center (**Figure 5**a).[70] This modification boosted the FE of ammonia from below 80–99.4% and doubled the NH_3 yield to 9396.7 μg h^{-1} cm^{-2} (Figure 5b). Furthermore, this catalyst exhibits excellent stability, maintaining a consistent ammonia yield of 3657.3 μg NH_3 h^{-1} cm^{-2} even after

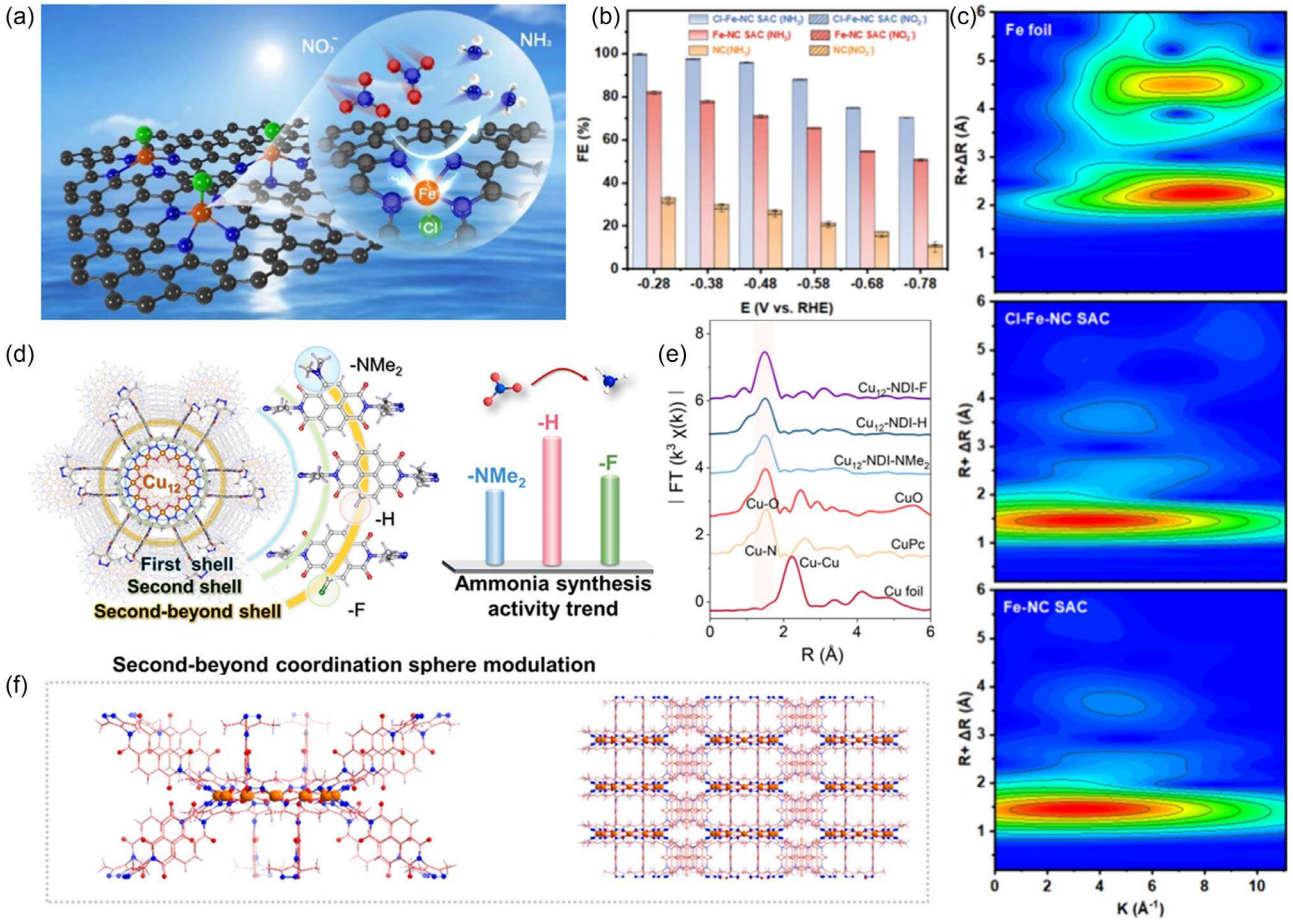

Figure 5. a) Schematic of axial Cl ligand coordination on an Fe single-atom catalyst for NO_3RR. b) FE_{NH3} and FE_{NO2^-} on Cl–Fe–NC and Fe–NC at different potentials. c) k^3-weighted EXAFS spectra at the Fe K-edge of Cl–Fe–NC and Fe–NC. Reproduced with permission.[70] Copyright 2025, American Chemical Society. d) Schematic of a Cu_{12}–NDI–X cluster with second-shell ligand coordination. e) EXAFS spectra at the Cu K-edge of Cu_{12}–NDI–X. f) Molecular structure of the Cu_{12}–NDI-H catalyst. Reproduced with permission.[73] Copyright 2025, American Chemical Society.

50 consecutive cycles at −0.28 V versus RHE. Fe K-edge EXAFS analysis showed the main peak shifting from 3.4 to 3.6 $Å^{-1}$ upon Cl coordination, confirming a change in the Fe electronic environment (Figure 5c).[68,71,72] DFT calculations further demonstrated that in the Cl–Fe–NC catalyst, the rate-determining step shifts from *NO → *NOH hydrogenation to $*NO_3 \rightarrow *NO_3H$, with the corresponding Gibbs free energy of reaction (ΔG) dropping from 0.68 to 0.15 eV. This highlights the significant enhancement of NO_3RR activity achieved by axial chlorine coordination.[68]

Li et al. took a second-sphere coordination approach, attaching organic naphthalene diimide ligands (NDI-H) to construct Cu_{12}–NDI–X clusters (X = NMe_2, H, F), thereby modulating the catalyst's secondary coordination shell (Figure 5d).[73] EXAFS shows the characteristic peaks of Cu–O and Cu–N at ≈1.51 Å in Cu_{12}–NDI–X, indicating the formation of a well-defined first coordination sphere (Figure 5e). In these catalysts, each Cu is coordinated by two oxygen and two nitrogen atoms (Figure 5f); the Cu coordination structure tunes the *d*-band center of the Cu active site and enhances NO_3^- adsorption and protonation of key intermediates.[74] Among the series, Cu_{12}–NDI-H (with hydrogen-functionalized ligands) showed the best performance, achieving a maximum NH_3 production rate of 35.1 mg h^{-1} mg_{cat}^{-1} and a FE of 98.7%. Additionally, the catalyst operates stably for 100 h at a current density of 100 mA cm^{-2}, showing only minimal declines in ammonia yield and conversion rate.

4.1.2. Defect Engineering: Modulating Electronic Structure and Intermediate Adsorption

Introducing defects such as atomic vacancies, step edges, or grain boundaries can profoundly alter a catalyst's reactivity. By creating coordinatively unsaturated sites, defect engineering modifies local electronic states and changes the adsorption strength and mode of key intermediates.[21,75]

One approach is to deliberately generate surface defects to enhance CO_2RR.[20] For instance, Wu et al. synthesized Cu catalysts with a high density of stacking faults (SFs) via laser irradiation.[76] Compared to an intact crystal lattice, these SF defects perturb the Cu electronic structure, leading to increased *CO coverage on the surface (**Figure 6**a). Ab initio molecular dynamics simulations and experiments confirmed the introduction of these structural defects. Using surface-sensitive electrochemical methods,

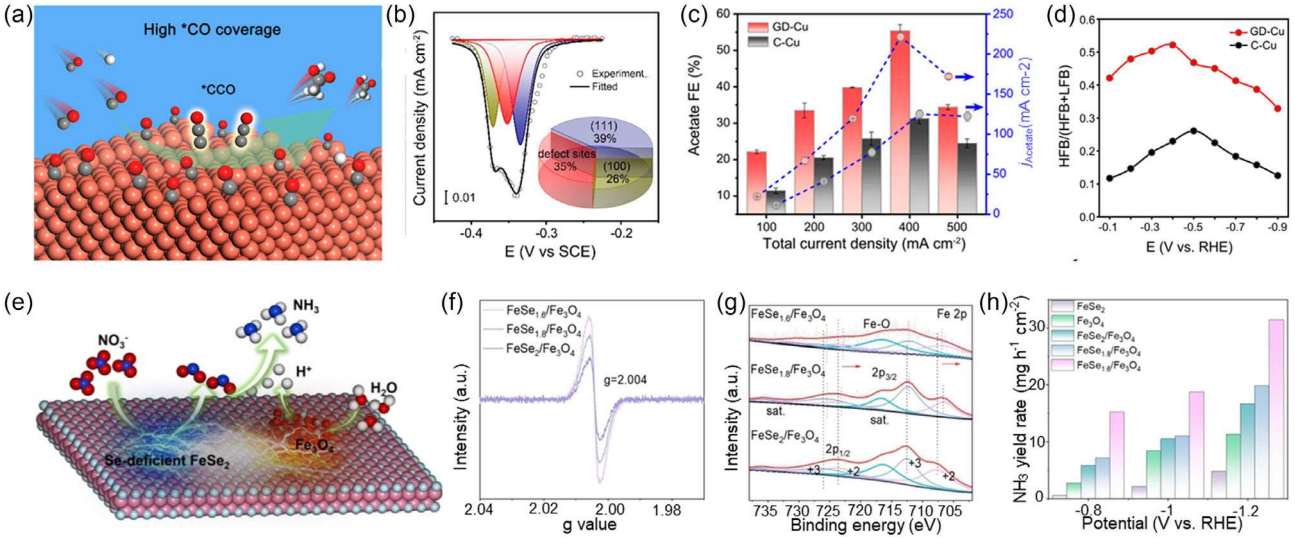

Figure 6. a) Schematic illustration of enhanced *CO adsorption on a defect-rich Cu surface. b) Lead underpotential deposition (UPD) curves indicating surface defect density on GD-Cu compared to commercial Cu. c) FE for acetate production and partial current densities for GD-Cu versus Cu-C at 400 mA cm^{-2}. d) Ratio of HFB to total (HFB + LFB) in situ spectroscopic signals for GD-Cu versus Cu-C. Reproduced with permission.[76] Copyright 2023, American Chemical Society. e) Schematic of the NO_3RR pathway on Se-vacancy-rich $FeSe_2/Fe_3O_4$. f) EPR spectrum of $FeSe_{1.6}/Fe_3O_4$ confirming Se vacancies. g) Fe 2*p* XPS spectra for $FeSe_{1.6}/Fe_3O_4$ versus $FeSe_2$. h) NH_3 yield rates of $FeSe_{1.6}/Fe_3O_4$ compared to $FeSe_2$ and Fe_3O_4. Reproduced with permission.[79] Copyright 2024, Wiley-VCH.

Wu et al. quantified the defect density, finding that gerhardtite-derived Cu (GD-Cu) nanoparticles have defect sites on ≈35% of their surface atoms, significantly higher than the ≈14% in commercial Cu (Figure 6b).[77] As a result, the FE for acetate on the SF-rich GD-Cu increased from 31% to 56% at a current density of 400 mA cm^{-2} (Figure 6c). This improvement indicates that SF defects create more active sites and enhance *CO coverage. In situ infrared and Raman spectroscopy further showed that the ratio of the high-frequency band (HFB) to the total (HFB + low-frequency band, LFB) is much higher for GD-Cu than for a defect-poor Cu (Cu-C), confirming that SF-rich GD-Cu provides more favorable *CO adsorption sites (Figure 6d). These results demonstrate that SF defects modulate the local electronic microenvironment of Cu, increasing back-donation of *d*-electrons into *CO antibonding orbitals and thereby strengthening *CO adsorption.

In NO_3RR, where sluggish proton transfer often limits the reaction rate, defect engineering can significantly accelerate the process.[40,78] Du et al. introduced selenium vacancies into $FeSe_2$ supported on Fe_3O_4, creating a catalyst with abundant defect sites (Figure 6e).[79] Electron Paramagnetic Resonance (EPR) spectroscopy detected a strong signal at $g = 2.004$ in the Se-vacancy-rich $FeSe_2$, confirming the generation of Se vacancies (Figure 6f). X-ray photoelectron spectroscopy (XPS) analysis of $FeSe_{1.6}/Fe_3O_4$ showed that the main Fe 2*p* peaks shifted to lower binding energies as the vacancy concentration increased (Figure 6g). The decreased peak width at higher defect levels indicates accelerated electron transfer on the catalyst surface due to Se vacancies, which modulate the electronic structure and favor NO_3^- adsorption. Consequently, $FeSe_{1.6}/Fe_3O_4$ achieved an NH_3 production rate of 31.46 mg h^{-1} cm^{-2} at 1.2 V versus RHE, which is 6.5 times and 2.8 times higher than those of $FeSe_2$ and Fe_3O_4 alone, respectively (Figure 6h). This enhancement is attributed to Se vacancies accelerating electron transfer and promoting H_2O activation, thereby facilitating NO_3^- deoxygenation and subsequent hydrogenation. Similarly, Singh and coworkers reported that the catalytic activity of rhodium sulfide is strongly dependent on sulfur vacancy defects. The presence of these vacancies enhances nitrate adsorption, reduces the dissociation energy barrier, and thereby improves activity by a factor of 1.6–5.6 compared to Rh/C.[80]

4.1.3. Catalyst Morphology and Overlayer Construction: Controlling Mass Transport

Electrocatalyst microenvironments not only involve active sites but also mass transport of reactants and products. Beyond tuning active sites, controlling mass transport is critical because it influences reaction rates, selectivity, and catalyst stability.[81] Two key strategies to improve mass transport in CO_2RR are morphological design of catalysts to create efficient transport channels and modifying electrode surfaces with polymers to regulate local reactant availability.

Highly ordered catalyst structures with hierarchical porosity can expose more active sites while also influencing local structure (oxidation state, electron density), thereby facilitating efficient reactant transport.[82] Tuning pore structure is thus a powerful strategy to optimize mass transport. Jia et al. synthesized a hierarchical porous single-atom Fe/N–C catalyst (HP-FeNC) by embedding isolated Fe atoms into a ZIF-8-derived carbon with a dodecahedral shape and ordered micro/mesoporosity (**Figure 7**a).[83] This architecture provides numerous accessible $Fe–N_4$ sites and improves CO_2 diffusion. Linear sweep voltammetry comparing HP-FeNC to a nonporous FeNC showed that

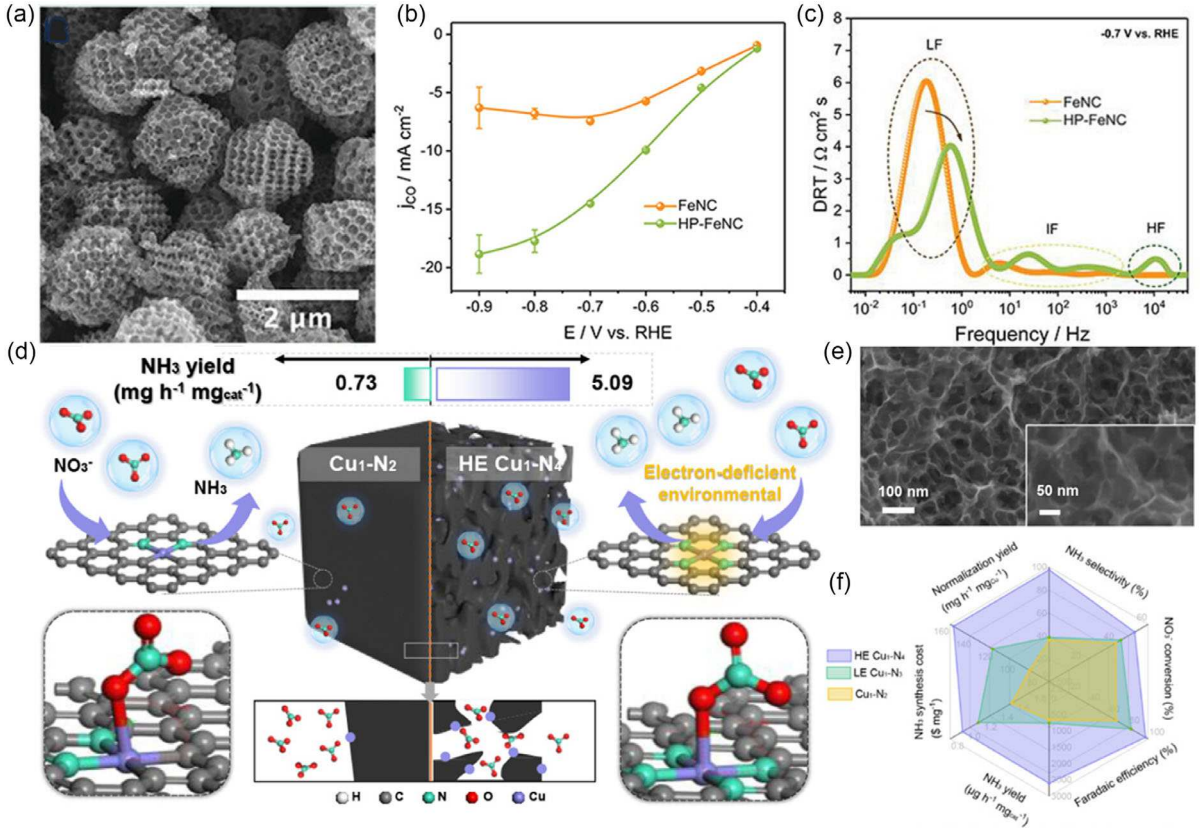

Figure 7. a) SEM image of HP-FeNC. b) j_{CO} for HP-FeNC and FeNC as a function of voltage. c) DRT spectra at −0.7 V versus RHE for HP-FeNC and FeNC. Reproduced with permission.[83] Copyright 2023, Wiley-VCH. d) Schematic comparison of a conventional Cu_1–N_2 and HE–Cu_1–N_4 with a porous dodecahedral framework. e) SEM image of the HE–Cu_1–N_4. f) Radar chart of NO_3RR performance metrics for HE–Cu_1–N_4. Reproduced with permission.[88] Copyright 2025, American Chemical Society.

HP-FeNC delivers higher current densities, indicating enhanced mass transport. Moreover, at −0.9 V, the CO partial current density (j_{CO}) increased from −6 to −19 mA cm^{-2} (Figure 7b). At the same potential, it also maintains a carbon monoxide FE above 90% over a 24-h period. At −0.7 V, the low-frequency distribution of relaxation times (DRT) peak for HP-FeNC was significantly lower and shifted to a higher frequency relative to FeNC (Figure 7c). This indicates that the presence of mesopores and macropores in HP-FeNC greatly accelerates CO_2 transport to isolated Fe sites, thereby improving the reaction kinetics.

Morphology control is also vital in NO_3RR. Importantly, the catalyst's support or substrate architecture can be engineered to reduce transport resistance.[84,85] Long et al. designed a Cu single-atom catalyst with high active site exposure and a locally electron-deficient environment (HE–Cu_1–N_4) on a highly porous carbon framework to maximize site exposure and minimize NO_3^- diffusion limitations.[86,87] Copyrolysis of ZIF-8 with melamine produced a unique 3D dodecahedral carbon framework with thin walls, termed HE–Cu_1–N_4 (Figure 7d).[88] During synthesis, melamine decomposition released HCN, which helped restructure the carbon framework and create larger pores (Figure 7e). This enlarged porosity facilitates reactant diffusion to active sites and thus boosts catalytic activity. Performance tests at −0.7 V versus RHE demonstrated that HE–Cu_1–N_4 achieved an NH_3 selectivity of 97.5%, an NH_3 production rate of 2609.2 μg h^{-1} mg_{cat}^{-1}, and FE_{NH3} of 97% (Figure 7f). These metrics were significantly better than those of other catalysts, owing to HE–Cu_1–N_4's reduced mass transport resistance and high density of exposed active sites that efficiently capture and activate NO_3^-. In 20 consecutive runs, the HE–Cu_1–N_4 catalyst maintained ≈95% selectivity for NH_3 in a continuous flow system, producing a total of 7.3 mmol of NH_3 and demonstrating strong potential for long-term operation. Furthermore, under real-world conditions using actual river water, the HE–Cu_1–N_4 catalyst still achieved 81.7% NH_3 selectivity, indicating robust performance in practical environments.

Another emerging approach is to modify electrode surfaces with functional polymers to tailor the microenvironment around active sites and control local reactant concentrations.[89] Polymer coatings can influence reactant/product transport and even local electronic properties, thereby affecting catalysis.

Li et al. coated Ag nanoparticles with a nitrogen-rich polypyrrole (PPy) film to create an Ag@PPy composite CO_2RR catalyst (**Figure 8**a).[90] The PPy coating increases the electrode's hydrophobic character and local CO_2 affinity, thereby suppressing the HER and boosting CO_2RR kinetics. In a flow cell at −300 mA cm^{-2}, Ag@PPy achieved a FE_{CO} of 91.7%, up from 43.8% for the uncoated Ag (Figure 8b). The PPy-coated Ag also exhibited a lower Tafel slope and reduced interfacial resistance

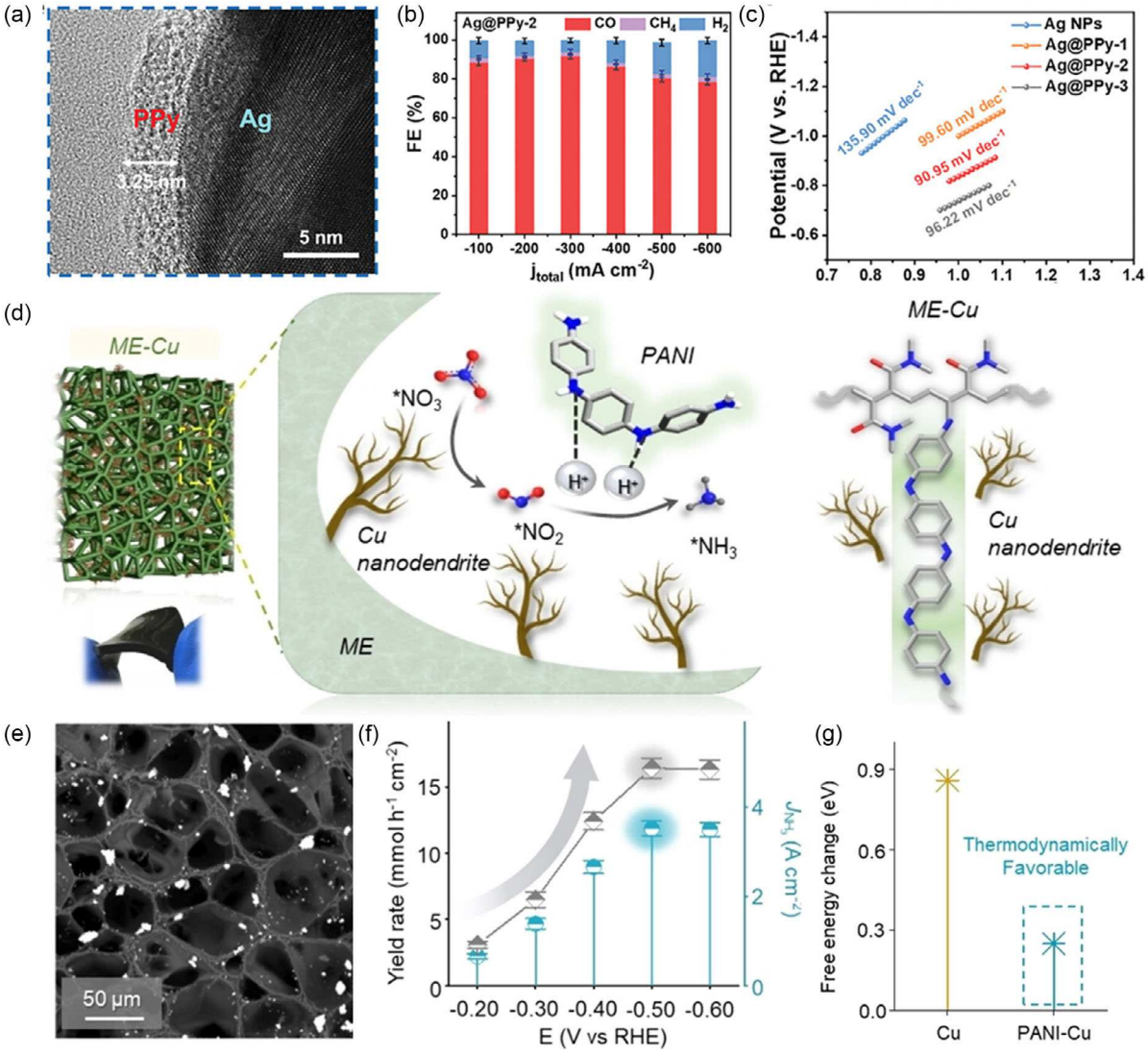

Figure 8. a) High Resolution Transmission Electron Microscope (HR-TEM) image of the Ag@PPy. b) FE_{CO} for Ag and Ag@PPy at $-300\ mA\ cm^{-2}$. c) Tafel plots comparing Ag@PPy and bare Ag. Reproduced with permission.[90] Copyright 2025, Wiley-VCH. d) Schematic of a PANI–Cu molecular electrode film with Cu nanodendrites for NO_3RR. e) SEM image of the PANI–Cu catalyst film. f) NH_3 yield rates and partial current densities for PANI–Cu and bare Cu (at -0.4 V). g) DFT-calculated energy barriers for *NO → *NOH on Cu and PANI–Cu. Reproduced with permission.[91] Copyright 2024, Wiley-VCH.

compared to bare Ag (Figure 8c). Temperature-programmed desorption showed that CO_2 binds more strongly on Ag@PPy (desorption at 247 °C vs. 209 °C for bare Ag), indicating that PPy increases the local CO_2 concentration at the surface. DFT calculations confirmed that the PPy layer lowers the activation energy for CO_2RR, suppresses competitive HER, and enhances CO selectivity.

Polymer modification has also been applied to improve NO_3RR. NO_3RR involves complex multistep protonation and often suffers from slow kinetics and poor NH_3 selectivity. To address these challenges, Su et al. designed a so-called "molecular electrode" by integrating a Cu catalyst with a polyaniline (PANI) polymer film for selective NO_3^- reduction to NH_3.[91] The PANI coating facilitates proton transfer to crucial $*NO_x$ intermediates on Cu, overcoming the proton transfer limitations of bare Cu in NO_3RR. Incorporating PANI also improves the composite's electrical conductivity and creates a highly porous film morphology, which enhances NO_3^- mass transport. Furthermore, the intimate contact between Cu nanostructures and the conductive PANI matrix promotes efficient electron delivery to the active sites (Figure 8d,e).[88] At -0.4 V versus RHE, the PANI–Cu molecular electrode achieved an NH_3 production rate of 12 mmol h^{-1} cm^{-2} at a current density of 2.7 A cm^{-2} (Figure 8f). DFT calculations showed that on the PANI–Cu system, the energy barrier for *NO → *NOH protonation is dramatically lowered (from 0.86 to 0.25 eV, Figure 8g), indicating that PANI actively promotes *NO protonation on Cu and accelerates the overall NO_3RR to NH_3 conversion.

4.2. Catalyst Design for C–N Coupling

Electrochemical C–N coupling reactions present far more complex challenges than single-reactant processes. By integrating

electronic/ligand modulation, defect engineering, morphology control, and interface design, strategies proven successful in CO_2RR or NO_xRR, researchers aim to promote the desired C—N bond-forming reactions while suppressing side reactions.[92] Below, we highlight how the strategies commonly employed in CO_2RR and NO_3RR can be adapted to advance C–N coupling reactions.

4.2.1. Modulating Axial Coordination to Optimize Electronic Structures of Active Sites for Electrocatalytic C–N Coupling

Tuning the electronic structure of catalytic active sites via tailored coordination environments is an effective approach to promote C—N bond formation.[26,93] A representative example is the electrochemical synthesis of urea from N_2 and CO_2, which is notoriously difficult due to the inertness of the N≡N triple bond.[7,68,94] To activate N_2, Zhang et al. developed a catalyst with axial chlorine ligands coordinated to a Zn–Mn–N framework (ZnMn–N,Cl), which helps to elongate the N≡N bond and facilitate its cleavage (**Figure 9**a).[95] EXAFS revealed that after Cl coordination, the main Fourier transform peak shifted from 1.56 to 1.64 Å (Figure 9b), consistent with Mn–Cl coordination that slightly displaces Mn out of the planar N_4 coordination environment. This electronic perturbation facilitates the coadsorption of N_2 and CO_2, promoting the formation of a *NCON intermediate and improving the tolerance to CO poisoning on the catalyst surface. Consequently, the ZnMn–N,Cl catalyst achieved a urea production rate of 4.0 mmol g^{-1} h^{-1} with a FE of 63.5%, significantly outperforming similar catalysts without Cl coordination (Figure 9c).

Coordination engineering is also effective for molecular catalysts in C–N coupling. Li et al. investigated a molecular copper phthalocyanine catalyst (CuPc) with tunable active site configurations (Figure 9d). By introducing electron-donating amino substituents on CuPc (to form CuPc-Amino), they strengthened the intramolecular Cu–N coordination, increasing the coordination number and optimizing the Cu electronic structure.[96] CuPc-Amino induces a blueshift of its Q-band, resulting in an altered electronic environment.[97] Fourier-transform extended X-ray absorption fine structure (FT-EXAFS) analysis further revealed that CuPc-amino has no Cu–Cu scattering and the average Cu–N coordination number rising from 3.9 to 4.2, which promotes structural stability. Electrostatic potential mapping indicated that the amino-modified CuPc has a more negative potential around the Cu–N_4 center, suggesting an enhanced ability to bind electrophilic intermediates and promote C–N coupling (Figure 9e). In an H-cell test, the CuPc-amino catalyst exhibited a volcano-shaped dependence of urea production rate on applied potential, reaching 103.1 ± 5.3 mmol h^{-1} g^{-1} at −1.6 V (Figure 9f), which is ≈2.6 times higher than that of pristine CuPc. The corresponding FE for urea was 11.9%, with a urea partial current density of 8.2 ± 0.5 mA cm^{-2}. Compared to CuPc, CuPc-amino exhibits significantly improved stability. Under an applied potential of −1.6 V versus RHE, CuPc-amino maintained a stable urea yield over 10

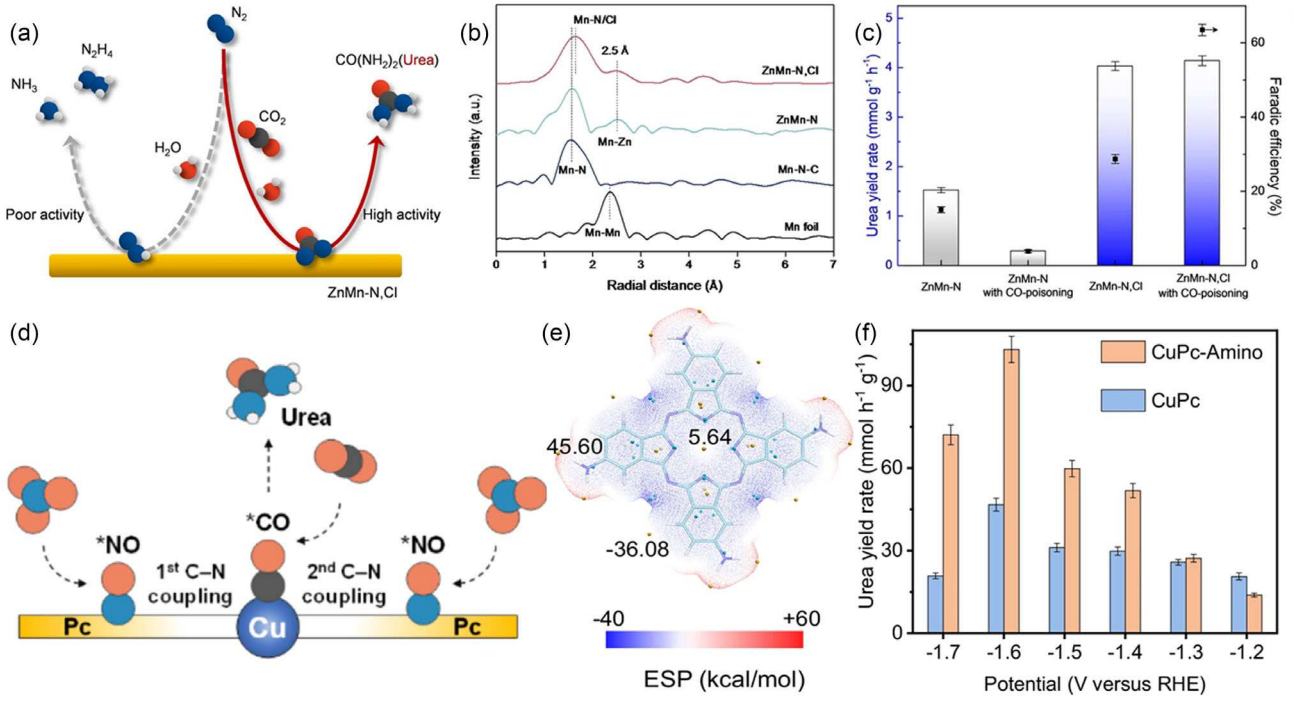

Figure 9. a) Schematic of N_2 activation and co-electroreduction of $N_2 + CO_2$ to urea on the ZnMn–N,Cl catalyst. b) Fourier transformed EXAFS spectra at the Mn K-edge for ZnMn–N,Cl versus a Cl-free reference. c) Urea yield rates and FEs for ZnMn–N,Cl versus control catalysts. Reproduced with permission.[95] Copyright 2023, Wiley-VCH. d) Proposed reaction mechanism for urea synthesis on CuPc versus CuPc-amino. e) Electrostatic potential maps of CuPc versus CuPc-amino, showing a more negative potential around the Cu–N_4 center in the amino-substituted catalyst. f) Urea yield rates as a function of potential on CuPc and CuPc-amino. Reproduced with permission.[96] Copyright 2024, Springer Nature.

cycles, whereas the unmodified CuPc catalyst showed a 67.4% drop in urea selectivity after the same number of cycles. These findings underscore that tailoring the coordination environment is a powerful way to modulate the electronic structure of active sites and boost C–N coupling activity.

4.2.2. Defect Engineering for C–N Coupling

Similar to the single-reactant reactions, introducing defects in catalysts can create unique active sites for C–N coupling reactions.[98] Vacancies and other defects can stabilize multiatom intermediates containing both carbon and nitrogen, facilitating their coupling or further transformation. By modifying surface electronic structure and providing coordinatively unsaturated sites, defect engineering can lower reaction energy barriers and enhance C–N coupling kinetics.[99]

For example, in many CO_2 and nitrate coupling systems, the formation of a $*CO_2NH_2$ intermediate is a high-energy, rate-determining step that limits the reaction rate. Lv et al. tackled this by introducing oxygen vacancies (V_O) into InOOH, creating an oxygen-vacancy-rich indium oxyhydroxide (V_O–InOOH) catalyst (**Figure 10**a).[100] The presence of V_O defects preferentially lowers the energy of the potential-determining step by weakening In—O bonds at unsaturated In sites, thus improving the catalytic performance (Figure 10b). EPR measurements detected a strong signal at $g = 2.001$ in V_O–InOOH, confirming abundant unpaired electrons associated with oxygen vacancies (Figure 10c). V_O–InOOH achieved a urea production rate of 592.5 $\mu g\ h^{-1}\ mg_{cat}^{-1}$ with a FE of 51%, significantly higher than the 378.4 $\mu g\ h^{-1}\ mg_{cat}^{-1}$ and 26.3% FE of pristine InOOH (Figure 10d). The oxygen vacancies render the catalyst surface electron-rich and locally *p*-type (electron-deficient) in character (Figure 10e). This property allows CO_2 molecules to accumulate at vacancy sites without being immediately reduced to CO or formate; instead, CO_2 at a vacancy preferentially reacts with *NO intermediates to form a *OCNO intermediate, thereby lowering the energy barrier for C—N bond formation. DFT calculations have demonstrated that the In surface sites become fully covered by $*NO_2$, which then combines with CO_2 to form a $*CO_2NO_2$ intermediate with a low energy barrier of 0.2 eV. Introducing a V_O at the In site rearranges the local electron distribution, promoting the protonation of $*CO_2NH_2$ and weakening its interaction with the In center in V_O–InOOH.[101]

Introducing oxygen vacancies in CeO_2 has a similar beneficial effect. Wei et al. synthesized a CeO_2 catalyst with a high density of oxygen vacancies (V_O–CeO_2), which exhibited a more mesoporous structure than stoichiometric CeO_2 (Figure 10f).[102] At −1.6 V, V_O–CeO_2 produced urea at 943.6 $mg\ h^{-1}\ g^{-1}$, three times the yield of defect-free CeO_2 (Figure 10g). Even after 10 cycles, the urea production current density and yield remained essentially unchanged. The enhanced performance is attributed to the creation of coordinatively unsaturated sites that strengthen

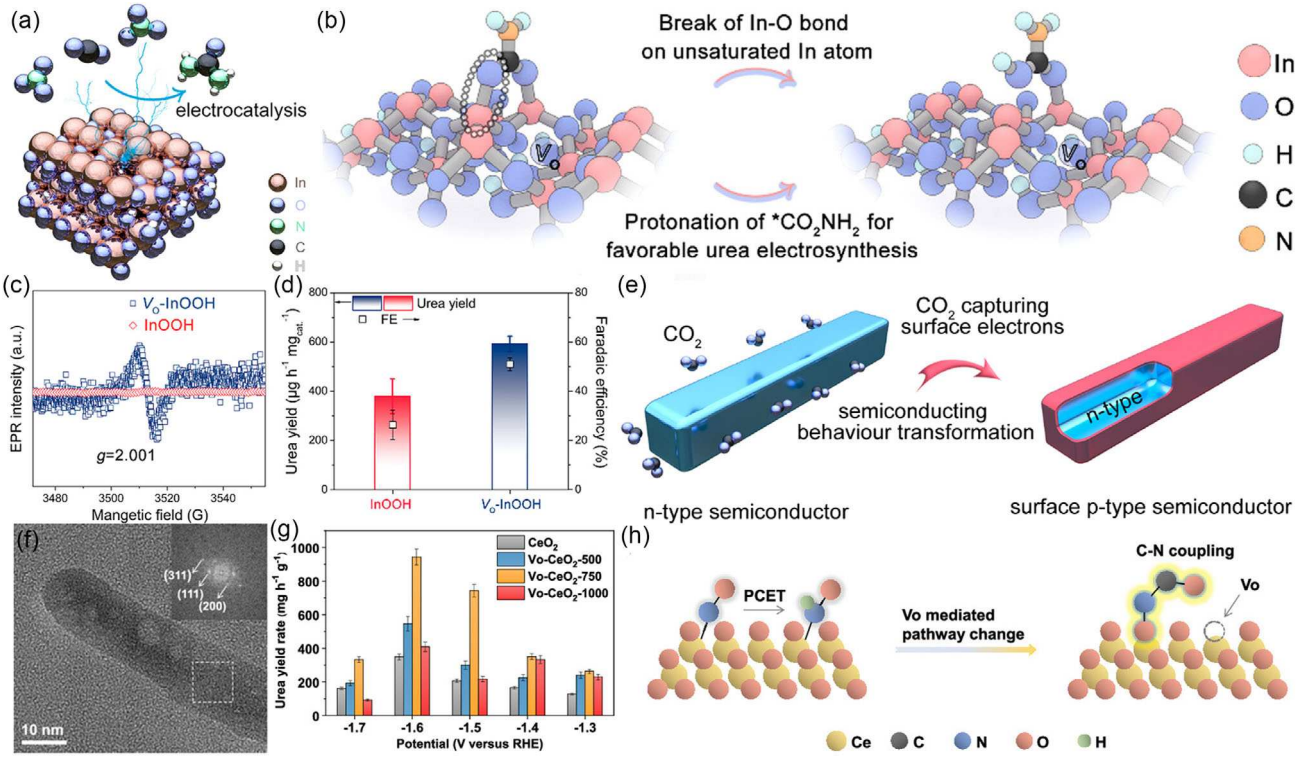

Figure 10. a) Schematic of the electrocatalytic $CO_2 + NO_3^-$ conversion to urea on V_O–InOOH. b) Structural models of pristine InOOH and V_O–InOOH and the associated energy change in the potential-determining step. c) EPR spectra of InOOH and V_O-InOOH. d) Urea yield rates on InOOH and V_O–InOOH. e) Schematic illustration of the local semiconductor type conversion induced by oxygen vacancies. Reproduced with permission.[100] Copyright 2022, American Chemical Society. f) Transmission Electron Microscope (TEM) image of V_O–CeO_2 showing its mesoporous structure. g) Urea yield rates for V_O–CeO_2 and CeO_2 at −1.6 V. h) Proposed reaction pathway on V_O–CeO_2. Reproduced with permission.[102] Copyright 2022, American Chemical Society.

the adsorption of reactants. V_O–CeO_2 not only improves the CO_2-to-CO conversion but also offers additional adsorption sites for nitrate. The vacancies stabilize the *NO intermediate, steering it toward coupling with *CO rather than complete hydrogenation to NH_3, thereby selectively boosting urea synthesis (Figure 10h). In situ sum-frequency generation (SFG) spectroscopy revealed distinct *NO and *OCNO peaks on V_O–CeO_2, with the *NO peak intensity gradually decreasing as the *OCNO peak intensified.[103] DFT calculations indicate that on V_O-rich CeO_2, the coupling of *NO with *CO faces an energy barrier of only ≈0.27 eV, favoring the formation of a *OCNO intermediate. Furthermore, these oxygen vacancies allow lattice O atoms to bond with adsorbed *NO, increasing the exposure of its N atom and reducing steric hindrance during the C–N coupling step.

Similarly, Song et al. introduced Zn into Fe_2O_3 to generate asymmetric oxygen vacancies, achieving a urea production rate of 7.48 mg h^{-1} mg_{cat}^{-1} and a stable urea FE over 50 h.[104,105] These results indicate that asymmetric oxygen vacancies enhance the reaction's activity and selectivity. In situ Raman and SFG measurements further showed that oxygen vacancies increase the surface *CO coverage, stabilize *NO and *CO intermediates, and promote the nucleophilic coupling of *CO with *NO to form *OCNO.[102] Consistent with these observations, DFT calculations confirm that asymmetric oxygen vacancies lower the Gibbs free energy barrier for the C–N coupling reaction.

Defect-engineered catalysts have expanded C–N coupling beyond urea.[31] For instance, Zhang et al. employed atomically dispersed Fe on oxygen-deficient TiO_2 to catalyze the coupling of glyceraldehyde with NO_3^- to produce glycine.[95] Nearly 100% of the glyceraldehyde was converted, with glycine as the main product (80.2% selectivity). In this system, oxygen vacancies on the TiO_2 support adsorb and activate NO_3^-, lowering the formation energy of the *NO intermediate. These vacancies may also bind glyceraldehyde through bidentate coordination. By bringing activated *NO and *CHO in close proximity to the defective surface, the system enables the $-NH_2$ group to attack the Fe-bound *CHO or promotes coupling of *NO and $*CH_2O$ fragments, ultimately forming the C—N bond in glycine.

4.2.3. Mass Transport Microenvironment Engineering in C–N Coupling

In electrocatalytic C–N coupling reactions, efficient mass transport of multiple reactants to active sites, as well as timely removal of products/byproducts, is crucial. Slow mass transport can lead to concentration gradients and limit the reaction rate, selectivity, or even catalyst stability. Two fundamental approaches to engineer the microenvironment for controlling mass transport are designing catalyst structures with enhanced porosity or tailored morphology, and incorporating functional polymer coatings at the interface to regulate reactant fluxes and intermediate retention.

Liu et al. demonstrated a structural strategy by developing a *p*-type semiconductor nanosphere catalyst (Ti-DHTP) for the coreduction of CO_2 and NO_3^- to urea.[106] This catalyst consists of microspheres (5–7 μm in diameter) assembled from 2D nanosheets of a titanium-based metal–organic framework, forming a porous semiconductor sphere termed Ti-DHTP (**Figure 11**a). The plentiful meso- and macroporosity between nanosheets exposes many active sites and shortens ion diffusion paths, thereby enhancing the reaction rate. Moreover, Ti-DHTP's *p*-type semiconducting nature (Figure 11b) means it has mobile hole carriers and a positively charged surface disposition, which repels protons and thus suppresses the competing HER. At −0.6 V versus RHE, it achieved a urea production rate of 348 μg h^{-1} cm^{-2} with a 21.75% FE, and a multicarbon (C_{2+}) selectivity of ≈96% (Figure 11c). Additionally, Ti-DHTP exhibited excellent stability in both cyclic and long-term tests at −0.6 V versus RHE. Its electrocatalytic activity remained steady over 30 successive cycles, and under prolonged electrolysis, urea synthesis continued for two days without any significant decline. Postreaction XPS and Scanning Electron Microscope (SEM) analyses confirmed that Ti-DHTP's structure and morphology were preserved, indicating no detectable degradation.

Similarly, Gerke et al. combined a pyrazole–borate imidazolate framework (BIF) with copper-based molecular cages to create a composite catalyst, BIF-(29)Cu, providing another example of morphology and interface control.[107] In BIF-(29)Cu, each Cu^{2+} is coordinated in a tetrahedral N_4 ligand environment within a cage (Figure 11d,e).[108] By disrupting the van der Waals interactions between these cages, the bulk material was broken down into a colloidally stable suspension of ≈300 nm particles. This downsizing greatly increased the exposed active surface area and facilitated diffusion of CO_2 and NO_3^- to the isolated Cu active sites. Multiwalled carbon nanotubes were used as a conductive support, further improving electron transport. Meanwhile, the BIF cages partially recrystallized into an ordered octahedral framework (Figure 11f), constructing well-defined pore channels that shorten mass transport distances for reactants and electrons. In situ X-ray absorption spectroscopy (XAS) confirmed that under CO_2/NO_3^- coreaction conditions, the CuN_4 coordination environment in the cages remained intact, indicating that the isolated Cu centers resisted aggregation and deactivation (Figure 11g). Thanks to these structural features, at −0.3 V versus RHE the composite achieved an optimal urea FE of 68.5% with a current density of 407 μA cm^{-2} (Figure 11h).

Functional polymer coatings can further act as interfacial architects in C–N coupling systems. By tuning their chemical composition, charge, hydrophilicity/hydrophobicity, and porosity, polymer films can selectively regulate the transport of key species at the electrode–electrolyte interface. Rather than being passive barriers, these coatings actively modulate local concentrations and fluxes through mechanisms like electrostatic attraction/repulsion or selective permeability.

Wang et al. demonstrated a case by applying an ordered bilayer polymer coating on a bimetallic Fe–Ni dual-atom catalyst (FeNi DAC) for urea synthesis (**Figure 12**a).[109] The inner layer is PANI, which contains protonatable amine groups, and the outer layer is a hydrophobic, nanoporous polymer of intrinsic microporosity (PIM) (Figure 12b). This bilayer design creates a hierarchical microenvironment in which the porous, hydrophobic PIM outer layer acts as a sieve that preferentially allows CO_2 to diffuse in while impeding water (Figure 12c).[110] This increases the local CO_2

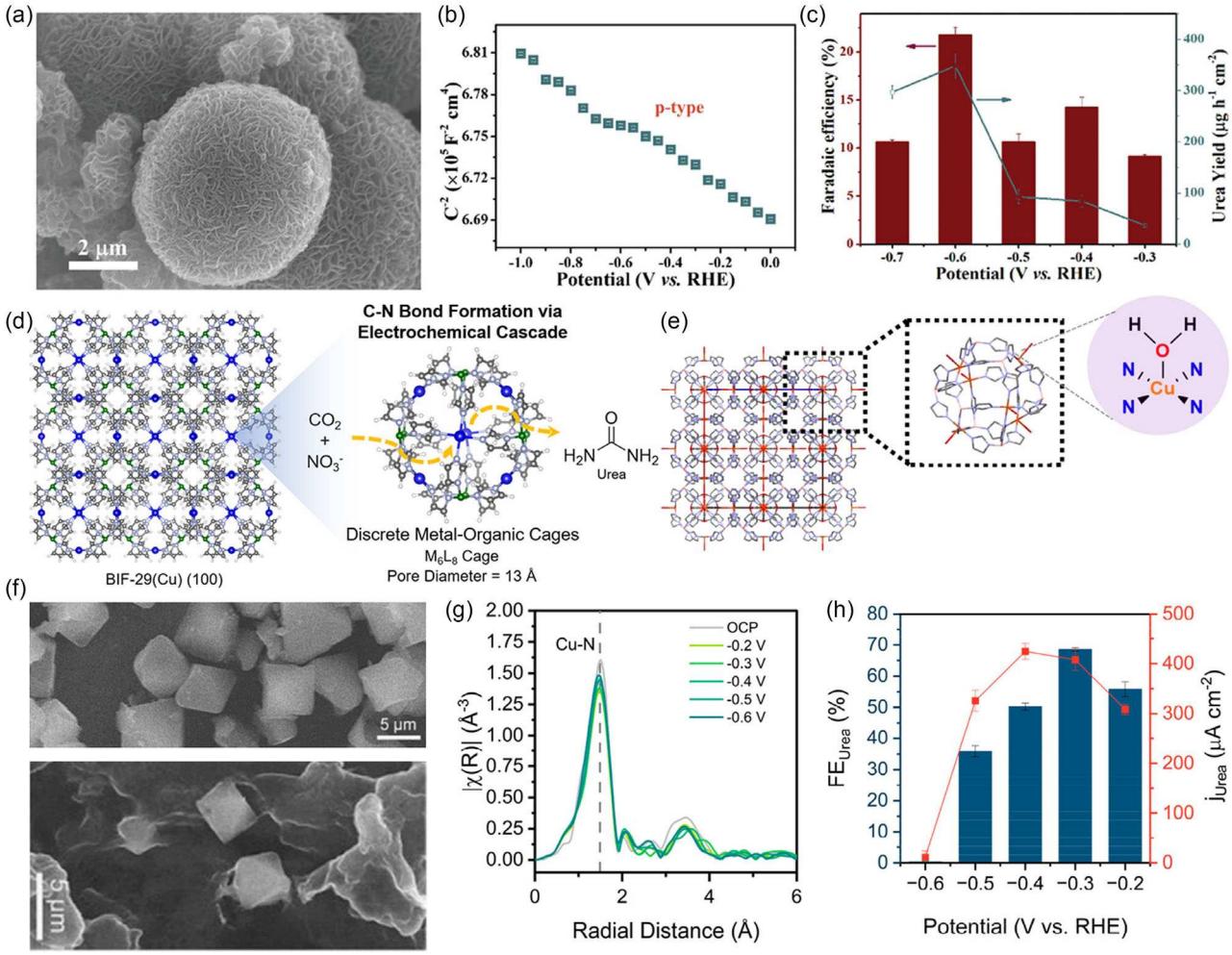

Figure 11. a) SEM image of Ti-DHTP microspheres. b) Mott–Schottky plot confirming *p*-type conductivity of Ti-DHTP. c) Urea FE and production rate on Ti-DHTP and potential. Reproduced with permission.[106] Copyright 2024, Wiley-VCH. d) Schematic of the BIF-(29)Cu. e) Tetrahedral CuN_4 coordination environment within a BIF cage. f) SEM images of bulk BIF-29(Cu) (top) and after recrystallization into ≈300 nm octahedral particles (bottom). g) EXAFS of BIF-29(Cu). h) Urea selectivity and current density in 0.1 M $KHCO_3$ + 0.1 M KNO_3. Reproduced with permission.[107,108] Copyright 2023, American Chemical Society.

concentration at the catalyst interface and helps suppress excessive H_2O/proton access, thereby mitigating HER. Meanwhile, the PANI inner layer, being rich in amine functionality, can capture and concentrate CO_2 near the active sites, effectively forming a CO_2 reservoir. The PANI also facilitates proton transfer in a controlled manner to the FeNi dual-atom sites, ensuring that protonation steps (necessary for both CO_2 and NO_3^- reduction) proceed efficiently. With this finely tuned microenvironment, the polymer-coated FeNi DAC achieved a urea production rate of 1671.6 μg h^{-1} mg_{cat}^{-1} with a FE of 75.3%. Finite element simulations confirmed that the bilayer polymer coating led to a higher CO_2 concentration near the catalyst surface and shortened diffusion distances for CO_2 relative to an uncoated catalyst (Figure 12d).

5. Tuning Microenvironment through Electrolytes and Ions

Electrolyte composition is a critical determinant of the electrochemical reaction microenvironment.[111,112] By influencing local pH, ionic strength, mass transport of reactants, and the EDL structure, the electrolyte can dramatically alter reaction pathways and efficiencies.[113,114] Tuning electrolyte properties has emerged as an effective strategy to modulate the interfacial environment and boost electrochemical performance.[53,115] Numerous studies in CO_2RR and NO_xRR have demonstrated that manipulating cation identity, concentration, and pH of the bulk electrolyte can enhance current densities and product selectivities.[116,117] Inspired by these successes, analogous electrolyte engineering has been extended to electrochemical C–N coupling, yielding promising results.[118]

5.1. The Roles of Ions and Electrolytes in CO_2RR and NO_xRR

5.1.1. Effects of Cation Identity

In CO_2RR and related reduction processes, alkali metal cations in the electrolyte are drawn to the negatively polarized cathode and accumulate in the EDL.[20,119] These cations have an outsized

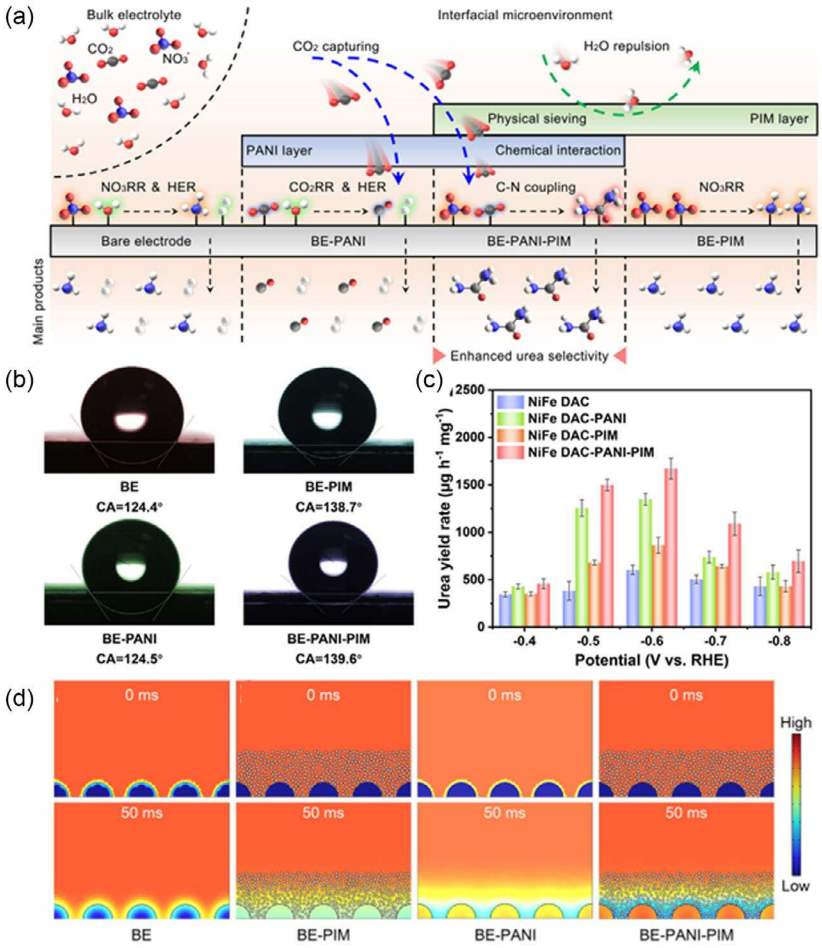

Figure 12. a) Schematic illustration of an orderly bilayer polymer coating on a FeNi DAC for urea synthesis. b) Contact angle measurements, demonstrating increased hydrophobicity with the PIM outer layer. c) Current–potential curves for catalysts with and without polymer coatings, showing enhanced current for the bilayer-coated electrode. d) Finite element simulation of CO_2 concentration profiles near the catalyst surface, showing higher CO_2 local concentration for the polymer-coated catalyst. Reproduced with permission.[109] Copyright 2024, Wiley-VCH.

influence on the interfacial environment by modulating local electric fields and buffering interfacial pH, thereby affecting reaction pathways. Currently, anions are also becoming increasingly popular and are achieving similar effects.[120] It is well-established that CO_2RR activity increases with larger cation size, generally following the order $Li^+ < Na^+ < K^+ < Cs^+$.[121,122] This trend has been observed across numerous catalysts (e.g., Ag, Au, Cu), especially under neutral or alkaline conditions, and is often attributed to the ability of larger, less strongly hydrated cations to more effectively alter the interfacial field and stabilize key CO_2RR intermediates. For example, in situ spectroscopy and simulation studies show that as the cation is switched from Li^+ to Cs^+, the hydration shell radius shrinks, allowing the cation to approach closer to the electrode surface and create a stronger local electric field (**Figure 13**a, b).[49,123] Cs^+ was found to cluster densely near a negatively charged Ag surface, increasing charge density in the EDL and enhancing CO_2 activation.[124]

Consistent with this, modulating the cation identity can significantly boost CO_2-to-CO conversion rates.[125] Gu et al. demonstrated that adding K^+ to an acidic CO_2 electrolyte (0.1 M H_2SO_4 + 0.4 M K_2SO_4) dramatically increased CO production on Au/C, achieving a ≈91% FE_{CO} at a partial current density of 227 mA cm^{-2}.[49] They attributed this improvement to K^+-induced modulation of the EDL; the cations altered the local field and inhibited proton migration toward the cathode, thereby suppressing HER and favoring CO_2RR to CO (Figure 13c). Subsequently, Pan et al. systematically investigated alkali cations under acidic CO_2RR conditions and observed that at fixed current density, the FE_{CO} increased monotonically with the cation's atomic number ($Li^+ < Na^+ < K^+ < Cs^+$) (Figure 13d).[126] Using Cs^+ electrolytes, they attained a CO partial current of ≈105 mA cm^{-2} with ≈60% FE_{CO} at −4.0 V, along with a single-pass CO_2 conversion of ≈90% in a flow cell (Figure 13e,f). These studies illustrate that larger cations strengthen the interfacial field and can dramatically boost CO_2RR kinetics toward carbon products.[127,128]

Beyond promoting C_1 products, alkali cations also influence pathways to C_{2+} products.[16,129] Larger cations in the EDL can stabilize C–C coupling intermediates by creating a more localized field within the Stern layer, thereby boosting C_{2+} product formation.[124] Monteiro et al. used ab initio molecular dynamics to show that larger hydrated cations (Na^+, K^+, and Cs^+)

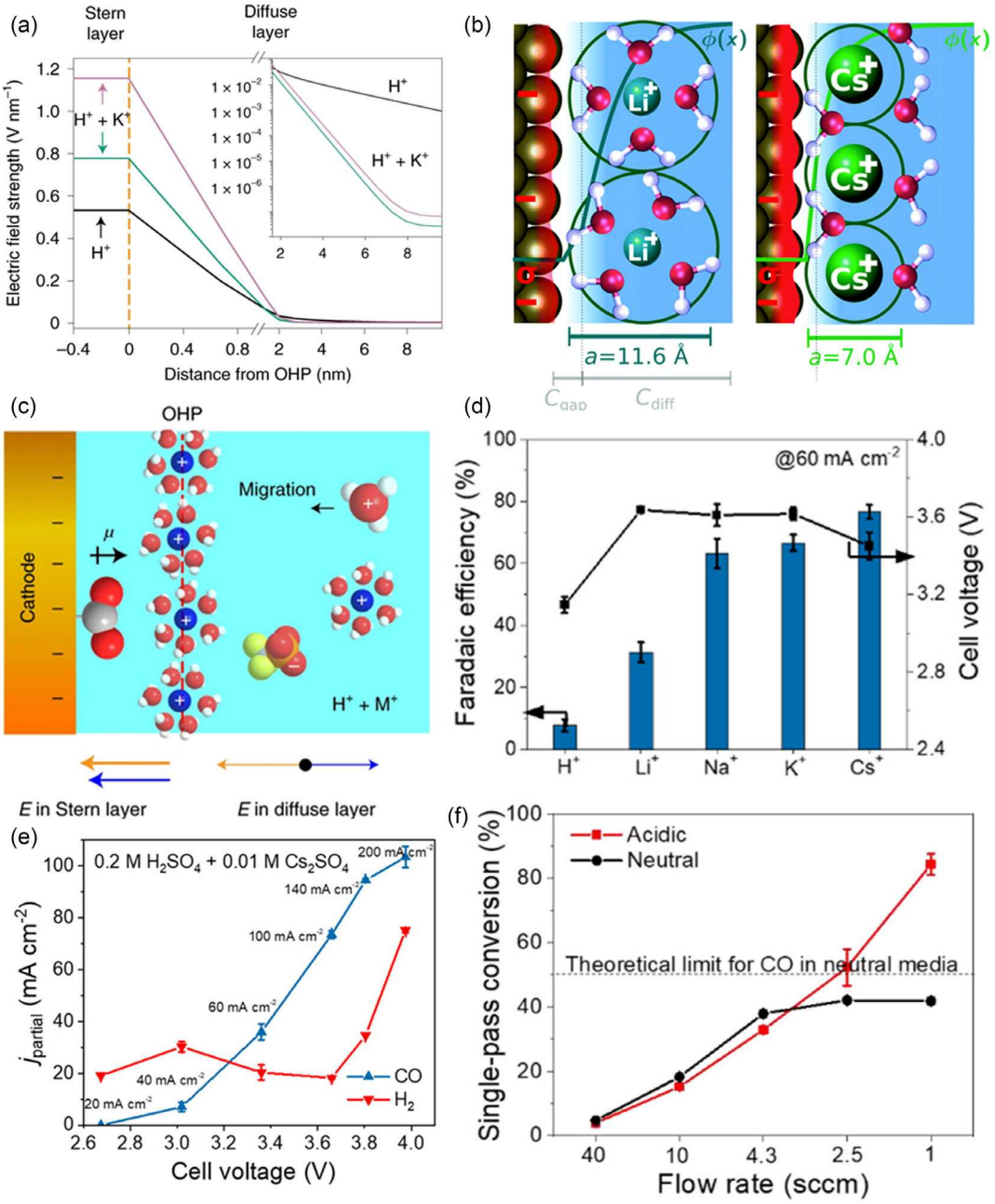

Figure 13. a) Simulation of the electric field as a function of Outer Helmholtz Plane (OHP) distance with and without K^+. Reproduced with permission.[49] Copyright 2022, Springer Nature. b) Schematic diagram showing the influence of the cationic hydration layer, *a*. Reproduced with permission.[197] Copyright, Royal Society of Chemistry. c) HOTf + MOTf cathode double-layer structure. d) The effect of alkali metal cations on the FE of CO. e) Effect of different voltages on the partial current density of H_2 and CO. f) The effect of flow rate on one-way conversion efficiency. Reproduced with permission.[126] Copyright 2022, American Chemical Society.

maintain higher interfacial concentrations and coordinate favorably with CO_2, stabilizing the CO_2^- intermediate and thus facilitating downstream C–C coupling (**Figure 14**a).[122] Experimentally, in a strongly acidic flow system, increasing K^+ concentration was found to improve C_{2+} product selectivity markedly. Feng et al. showed that in 0.05 M H_2SO_4 with added KCl, the FE toward C_{2+} products rose to ≈86% at −900 mA cm^{-2} total current density (Figure 14b,c).[130] Finite element simulations confirmed that K^+ enrichment in the catalyst's porous network raised local pH and suppressed HER (Figure 14d). Consistently, other studies show that moving from Li^+ to Cs^+ lowers the C_1/C_2 product ratio (e.g., from ≈6.2 with Li to ≈0.5 with Cs), indicating a shift toward multicarbon products with larger cations.[131]

A similar "cation effect" is observed in NO_3RR, though the optimal cation ordering can differ depending on the catalyst and reaction conditions.[132,133] Fajardo et al. reported that for NO_3RR to ammonia on Sn, the enhancement followed

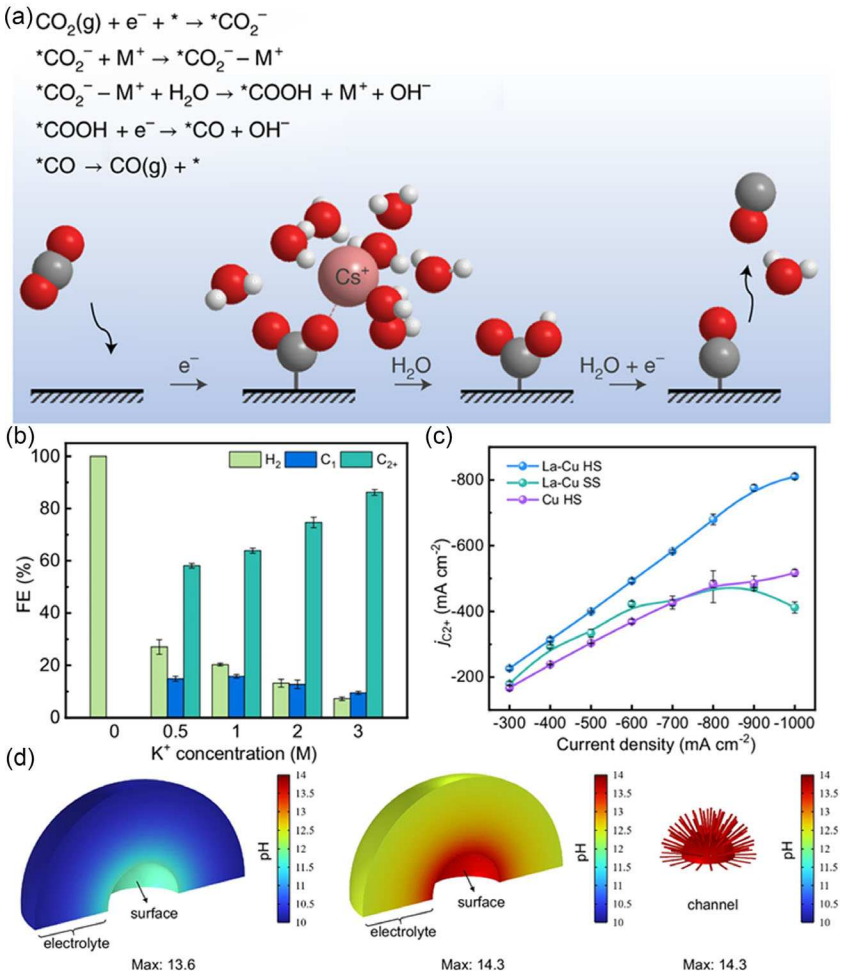

Figure 14. a) Schematic diagram of the mechanism of cations and $*CO_2^-$ intermediates. Reproduced with permission.[122] Copyright 2021, Springer Nature. b) The effect of K^+ concentration on the total FE of La–Cu H. c) C_{2+} products partial current density over La–Cu HS, La–Cu SS, and Cu HS under different current densities. d) The pH distribution in electrolyte near surface of solid sphere, hollow sphere, and within channels of hollow sphere. Reproduced with permission.[130] Copyright 2024, Springer Nature.

$Li^+ < Na^+ \approx K^+ < Cs^+$, paralleling the CO_2RR trend (**Figure 15**a).[134] In their system, the stronger interfacial field with larger cations stabilized an $*NO_2^-$ intermediate, suppressing its accumulation. Switching from LiOH to CsOH electrolyte decreased the undesired nitrite selectivity from 65% to 5.9%, while FE_{NH3} rose from 15% to 39%.

However, Yu et al. found a slightly different sequence for ammonia production on a Cu cathode ($Li^+ < Cs^+ < Na^+ < K^+$), with K^+ yielding the highest NH_3 rates (Figure 15b).[22,135] They attributed lower Cs^+ performance to an unusually low double-layer capacitance (C_{dl}) in CsOH on Cu, indicating fewer oriented water dipoles and thus less effective proton availability. Indeed, the measured C_{dl} followed $Li^+ < Cs^+ < Na^+ < K^+$, correlating with the NH_3 formation rates (Figure 15c). Fewer polarizable water molecules in the Cs^+ double layer meant slower protonation of intermediates, thus limiting ammonia yield despite Cs's strong field effect (Figure 15d). This is not exceptional, the same C_{dl} order on a Cu/Cu_2O catalyst and concomitant trends in NO_3^- conversion and NH_3 selectivity.

5.1.2. Effect of pH on CO_2RR and NO_xRR Activity

Electrolyte pH exerts a complex influence on CO_2RR, affecting both reaction kinetics and carbon utilization.[136,137] A well-known paradox is that while an alkaline environment at the cathode generally suppresses the competing HER and favors C–C coupling,[138] it causes significant CO_2 loss to carbonate formation.[139] Strongly basic media prevent carbonate formation, but then the local proton-rich environment strongly favors HER, severely curbing CO_2RR activity. To resolve this, the ideal scenario is to create an acidic bulk while maintaining an alkaline local pH near the cathode. Sargent and coworkers achieved this by introducing a cation amplification layer (CAL), a perfluorosulfonic acid ionomer film coated on the catalyst, to regulate ion transport at the interface.[140] The CAL is designed to enrich K^+ near the Cu catalyst surface while impeding OH^- diffusion away. This creates a KOH-rich microenvironment at the catalyst even when the bulk electrolyte is acidic (**Figure 16**a). In a flow electrolyzer with a 1 M H_3PO_4($pH < 1$) + 3 M KCl bulk electrolyte, the CAL-modified

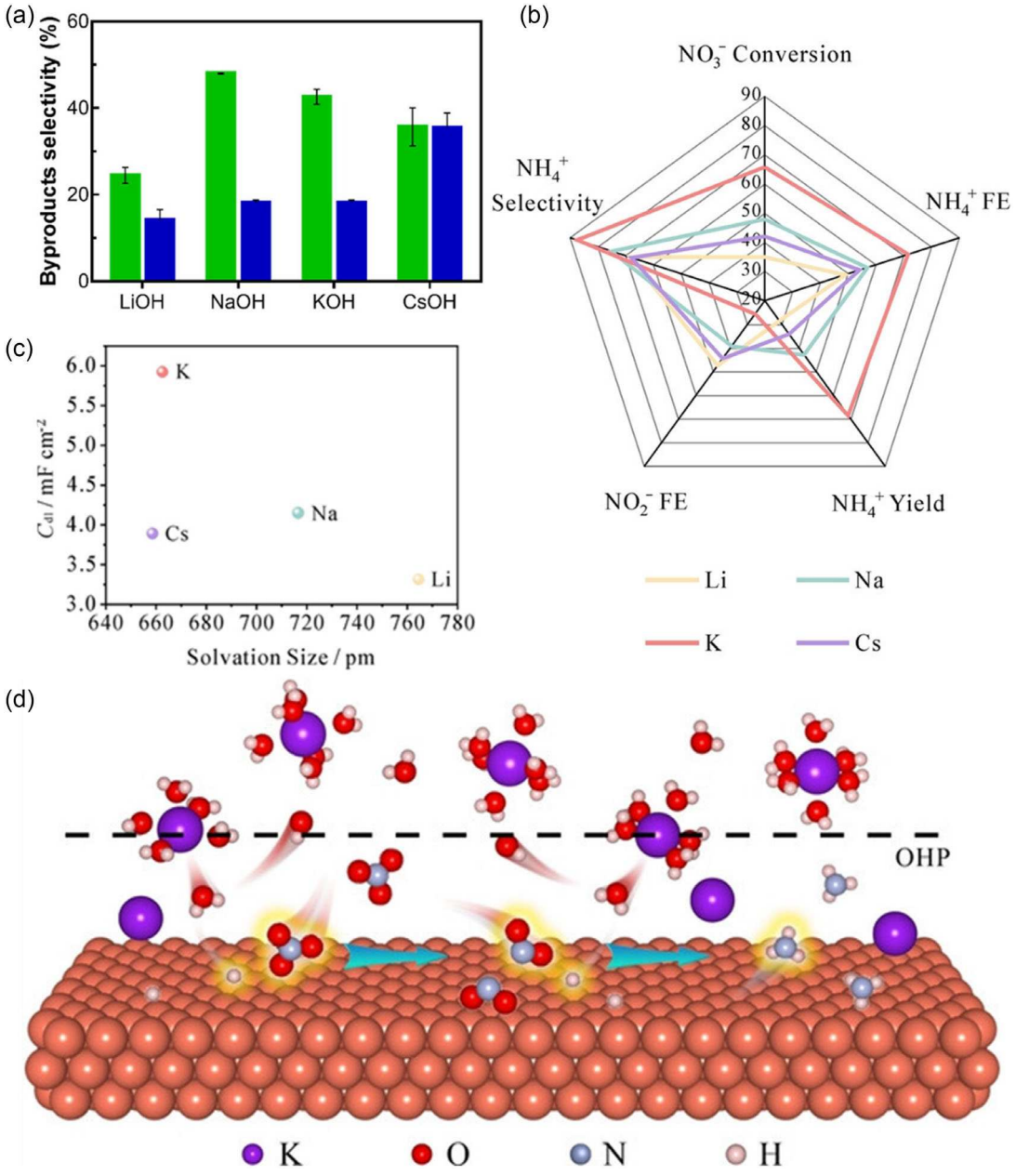

Figure 15. a) Selectivity of different alkali metal cation electrolytes toward N_2 (green) and NH_3 (blue) at 20 mg NO_3^-N L^{-1}. Reproduced with permission.[134] Copyright 2023, Elsevier. b) At the same potential, the effects of different alkali metal cations on NO_3^- conversion rate, NH_3 selectivity, NH_3 concentration, NO_2^- concentration, and NH_3 yield. c) Relationship between alkali metal cation size and C_{dl}. d) Schematic diagram of the promoting effect of K^+. Reproduced with permission.[135] Copyright 2024, Wiley-VCH.

Cu achieved a local pH ≈9 at the cathode interface when running at 400 mA cm^{-2}, versus only ≈7.2 local pH without the CAL under the same conditions. This local alkalinity directly translated to improved C–C coupling; the FE_{C2H4} reached 13% with the CAL, compared to 9.3% without (Figure 16b–d).

Beyond ionomer layers, increasing the bulk concentration of supporting cations can also elevate local pH under reaction conditions.[141,142] In the same study, increasing K^+ from 1 to 3 M in the acidic electrolyte enhanced C_2H_4 formation (FE_{C2H4} from ≈10% to 26% at 1.2 A cm^{-2}, Figure 16e). Furthermore, lowering the CO_2 flow rate gave CO_2 more residence time to interact with the enriched K^+, thereby increasing single-pass carbon efficiency to 77% with C_{2+} products contributing ≈50% of the converted carbon (Figure 16f). Under these optimized conditions, the total C_{2+} partial current reached ≈600 mA cm^{-2}. In summary, local pH control is key to reconciling the activity-utilization trade-off in CO_2 electrolysis.

For nitrate reduction, pH control is likewise crucial. $NO_3^-$to NH_3 conversion requires a supply of reactive hydrogen to hydrogenate N-containing intermediates.[143] In strongly alkaline media, proton availability is limited, which can slow nitrate reduction despite favorable HER suppression. Indeed, most NO_3RR systems

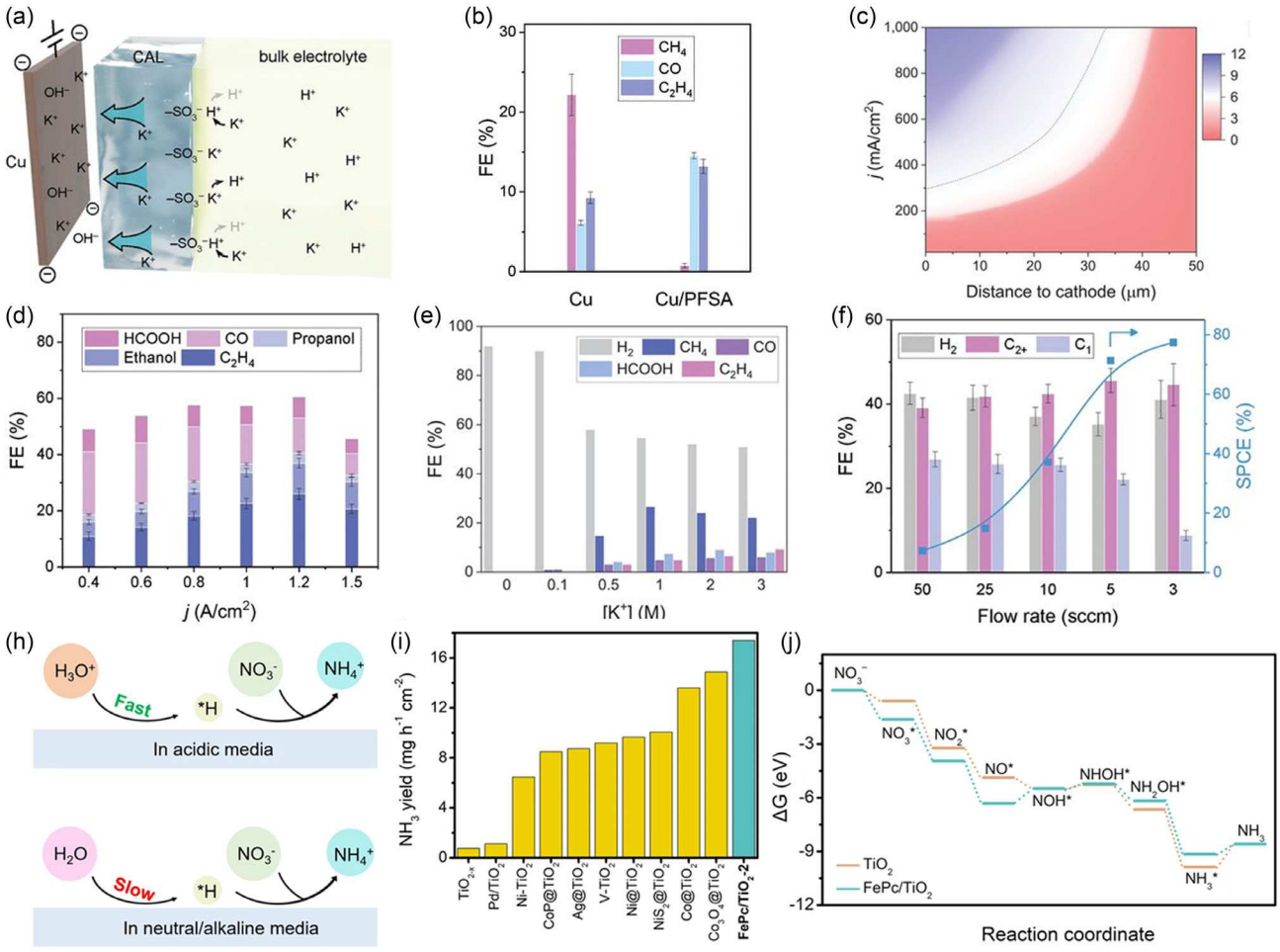

Figure 16. a) Schematic diagram of ionic transport near the catalyst surface functionalized by the Perfluorosulfonic Acid (PFSA) ionomer. b) FEs toward gaseous CO_2RR products on bare Cu and PFSA-modified Cu (Cu/PFSA). c) Schematic diagram showing the effects of pH and current density at different distances. d) The FE of the products generated varies with changes in current on the CAL-modified Cu electrode. e) The effect of different K^+ concentrations on FE. f) Distribution relationship between product and flow rate on CAL-modified Cu electrodes. Reproduced with permission.[140] Copyright 2023, The American Association for the Advancement of Science. h) Pathway for *H production in NO_3RR. i) NH_3 yield performance in acidic media. j) Free energy diagram for NO_3^- reduction on FePc/TiO_2. Reproduced with permission.[146] Copyright 2023, Springer Nature.

operate better in basic electrolytes, and discussions often focus on alkaline conditions.[144] However, overly alkaline conditions can suffer from proton starvation. On the other hand, in strongly acidic media, nitrate reduction is usually plagued by side reactions, yet the abundant protons can accelerate certain steps and potentially increase overall nitrate conversion. This has spurred interest in nitrate reduction under acidic conditions.[145]

Strongly acidic electrolyte conditions can overcome the proton limitation in alkaline and neutral NO_3RR (Figure 16h).[146] Zhang et al. designed a FePc/TiO_2 composite catalyst based on the inspiration of the iron active center in biological nitrite reductase.[147,148] The catalyst exhibited excellent stability in acidic medium at pH = 1, and its poor HER activity effectively suppressed the side reaction while achieving 17.4 mg h^{-1} cm^{-2} NH_3 yield and 90.6% FE (Figure 16i). Theoretical calculations further revealed that the acidic environment significantly enhanced the overall reaction kinetics by optimizing the energy barrier of the rate-controlling step of *NO → *NOH. (Figure 16j) This finding suggests that rational regulation of electrolyte acidity can synergistically address the balance between proton supply and side-reaction inhibition, providing an important direction for the design of efficient NO_3RR catalytic systems.

5.2. Role of Ions and Electrolytes in Electrochemical C–N Coupling

The above findings for single-feed CO_2RR and NO_3RR suggest that carefully regulating cation identity, cation concentration, and pH in the reaction environment can tune interfacial electric fields, stabilize specific intermediates, and control competitive reactions.[149,150] It follows that these strategies should similarly benefit coelectrolysis of CO_2 with nitrogen species to form C–N coupled products.[151] In the following, we discuss how cation effects and pH modulation specifically impact the formation of C—N bonds via $CO_2 + NO_x$ coreduction, highlighting mechanistic insights and experimental advances.

5.2.1. Effects of Cation Identity on C–N Coupling

Analogous to the trends in CO_2RR and NO_3RR, the identity of alkali cations in the electrolyte strongly affects urea synthesis from CO_2 and nitrate.[98,152] Wang and coworkers demonstrated this clearly on a TiO_2 catalyst, where both the cation identity and its concentration influenced the assembly of C–N intermediates and the selective formation of urea.[35,153] At an applied potential of −1.50 V versus RHE, their TiO_2 electrode achieved an exceptionally high urea yield of 265.6 ± 13.3 mmol h^{-1} g_{cat}^{-1}. This performance was attributed primarily to the electrolyte cation effect, the urea formation rate followed the trend $Li^+ < Na^+ < Cs^+ < K^+$, with K^+ giving the best results (**Figure 17**a). In 1 M $KHCO_3$ electrolyte, the TiO_2 delivered a

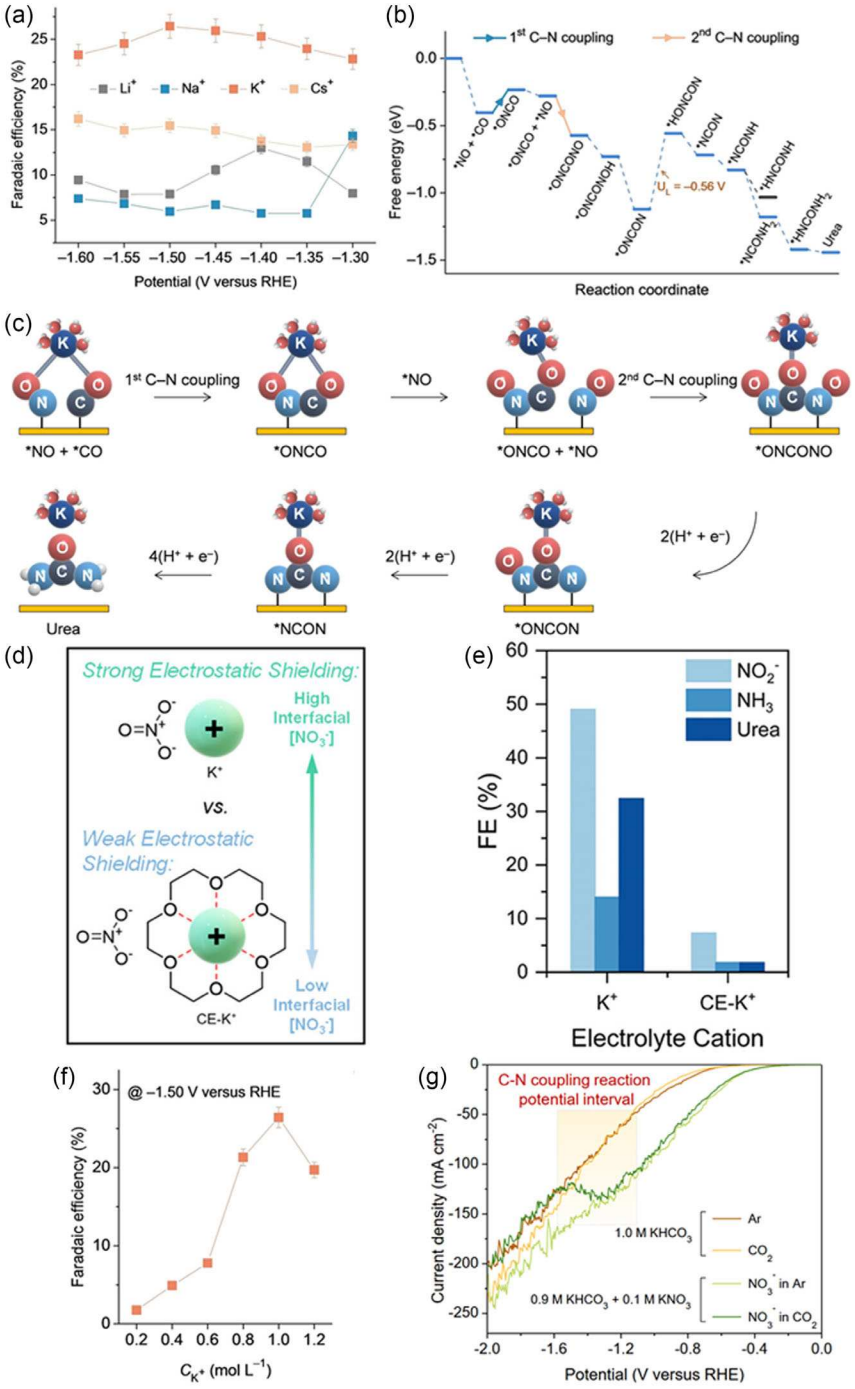

Figure 17. a) The effect of different alkali metal electrolytes on FE. b) Free energy diagram on TiO_2 (101) with the cation effect considered. c) Under the influence of K^+, the urea synthesis pathway. d) Schematic diagram showing the effect of 18-crown-6 (CE-K^+) on the reaction. e) The effect of cations acting as free or chelated ions on NO_3RR. Reproduced with permission.[155] Copyright 2023, American Chemical Society. f) Urea yield rates with various concentrations of K^+. g) Linear sweep voltammetry curves of TiO_2. Reproduced with permission.[153] Copyright 2023 Wiley-VCH GmbH.

26.4% FE_{urea} and a $jure_a$ of 22.9 mA cm^{-2}, whereas in 1 M $LiHCO_3$, these metrics dropped to 7.8% and 2.3 mA cm^{-2}, respectively. Computations on the TiO_2(101) surface showed that alkali cations stabilize the direct coupling of *CO and *NO to form a CO–NO adduct (Figure 17b). Crucially, the estimated energy barrier for the C–N coupling step decreased in the order $Li^+ > Na^+ > Cs^+ > K^+$, inversely correlating with the observed urea activity.[154] This trend mirrors the earlier single-reaction behaviors and underscores that K^+ provides the optimal balance of effects.

Mechanistically, larger cations (Na^+, K^+, Cs^+) tend to accumulate at the outer Helmholtz plane and can create a strong local electrostatic field that overcoming electrostatic barriers to reactant adsorption and stabilizes negatively charged intermediates.[127] Changing the type of cation can significantly lower kinetic barrier for the $*CO + *NO \rightarrow *ONCO$ step (From 0.73 for Li^+ to 0.22 for K^+). In the C–N coupling context, this means more *CO and *NO can adsorb and coalesce at the surface. For example, K^+ was proposed to promote formation of the key *ONCO intermediate through a "push–pull" electrostatic effect (Figure 17c). K^+ is large enough to effectively screen the repulsion between *CO and *NO and bring them into proximity, yet not so large as to sterically hinder their interaction. By contrast, Li^+ with its tight hydration shell cannot accumulate sufficiently at the interface to aid coupling. Although Cs^+ is the largest, which can reduce the availability of catalytic sites or alter hydration structure. Thus, K^+ emerged as the "just right" cation for urea, facilitating C—N bond formation more effectively than either smaller or larger alkali ions.

A clever experiment to verify the role of cation-induced fields was conducted by introducing a crown ether to bind K^+ in situ. 18-Crown-6 selectively complexes K^+, effectively reducing the "free" K^+ available in the double layer (Figure 17d).[155] With crown ether added to a K^+ electrolyte, the urea yield dropped significantly (Figure 17e). This is strong evidence that K^+ is presence in the EDL was crucial for driving the C–N coupling once SEQUESTered, the beneficial effect diminished. It thus confirms that cation-induced electric field modulation is a key driver for the enhanced C–N coupling observed.

In addition to cation identity, the concentration of cations in the electrolyte can modulate C–N coupling performance. Increasing K^+ was found to improve urea production on the TiO_2 catalyst, but with an optimal window before performance declined (Figure 17f). For instance, raising the $KHCO_3$ concentration from 0.2 to 1.0 M, the urea yield increased from 13.6 to 265.6 mmol h^{-1} $g_{cat}{}^{-1}$. The 1 M K^+ electrolyte also showed the appearance of a distinct cathodic peak in Linear Sweep Voltammetry (LSV) scans around −1.5 V versus RHE, indicating that a higher K^+ concentration thermodynamically favors the C–N coupling reaction (Figure 17g).

However, beyond an optimal concentration, further increasing K^+ can diminish performance. In the TiO_2 study, when K^+ was increased beyond ≈1 M, the urea partial current and FE began to drop. It may be that with very high cation concentration, the system may favor the "self-hydrogenation" of N intermediates over the cross-coupling with CO_2. Simultaneously, overly high local KOH concentrations can begin to inhibit CO_2 activation and can enhance HER due to the high ionic strength promoting water dissociation. Thus, beyond a certain K^+ concentration, the synergy between CO_2 and NO_3^- reduction breaks down.

5.2.2. Correlation between Surface Coverage and pH

Achieving efficient C–N coupling requires balancing the reaction kinetics of both carbon and nitrogen sources, which often have different optimal pH requirements.[6,156] CO_2RR benefits from a locally high pH, whereas NO_3^-/NO_2^- reduction steps require protons for hydrogenation. The surface coverage of key intermediates is therefore sensitive to the proton availability at the interface. Careful pH adjustment can tilt the coverage in favor of intermediate coadsorption and subsequent coupling.[157] If the environment is too alkaline, there may be plenty of *CO but a dearth of *H or *NOH, stalling the reduction of nitrogen intermediates. Conversely, if too acidic, $*NO_x$ intermediates hydrogenate fully to NH_3 and *CO coverage drops due to competition from HER. Thus, an intermediate, mildly acidic condition can be advantageous to provide some protons without overwhelming the CO_2RR.

Experimentally, Chen et al. illustrated this balance by varying the initial pH in a $CO_2 + NO_3^-$ electrolysis system.[158] Using a $CuInS_2$ catalyst with a mixed electrolyte (0.05 M KNO_3 + 0.05 M $KHCO_3$), they found that adjusting the bulk pH from ≈8 to 5 significantly boosted the reaction rate and urea yield. At pH 5, the current density increased and the urea yield reached 3017 μg h^{-1} $mg_{cat}{}^{-1}$ with a 19.6% FE_{urea} at −1.3 V (**Figure 18**a). In contrast, at the unadjusted pH ≈8, the urea concentration was only 5.3 mg L^{-1}. This dramatic improvement with slight acidity indicates that proton availability was a limiting factor at neutral pH. By providing more protons (pH 5), the formation of $*NH_x$ species from nitrate was facilitated, which could then couple with *CO to form urea more readily. Importantly, the pH was not so low as to trigger dominant HER or completely convert all $*NO_2$ to NH_3; it struck a balance that favored the coupling pathway.

The mechanistic impact of pH on C–N coupling has been probed by theory as well.[159,160] Wu et al. performed a detailed analysis of the pH-dependent mechanism for urea synthesis from CO_2 and nitrite (NO_2^-) on Cu.[161] They considered proton-coupled electron transfer steps proceeding via either an Eley–Rideal (E–R) mechanism or a Langmuir–Hinshelwood (L–H) mechanism (Figure 18b). Their calculations on Cu(100) revealed that the rate-determining step in nitrite reduction is the hydrogenation of $*NH_2$ with an activation barrier of 0.754 eV (Figure 18c). This step critically requires protons, meaning its rate will depend on proton concentration. Using degree of rate control and coverage analyses, they found that at neutral pH, the Cu surface is predominantly covered by $*NO_2$, indicating that the subsequent hydrogenation is sluggish due to limited protons. In fact, the $*NO_2$ coverage was so high that the system likely follows an E–R pathway for hydrogenation. However, if the local H^+ is increased, this protonation step can accelerate. Lowering the pH would increase the availability of H_2 to convert $*NO_2$ to *HNO, thereby speeding

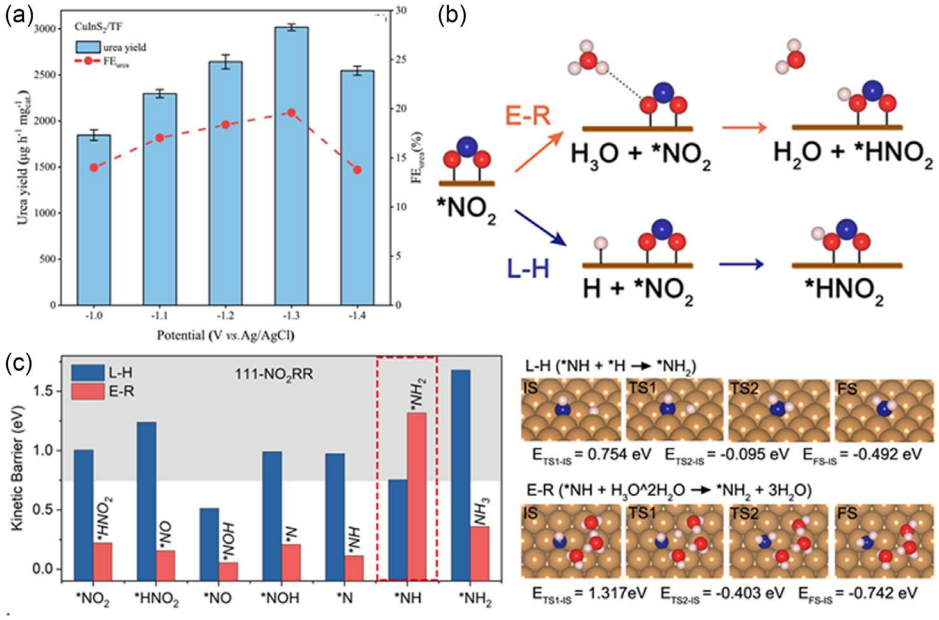

Figure 18. a) $CuInS_2$/Titanium foam ($CuInS_2$/TF) electrode for urea yield and FE diagram. Reproduced with permission.[158] Copyright 2024, Elsevier B.V. All rights reserved. b) Schematic diagram of E–R and L–H mechanisms. c) The kinetic process for the *NH hydrogenation step. Reproduced with permission.[161] Copyright 2024, Springer Nature.

up the rate-determining step and freeing up the surface for C–N coupling. In essence, a modestly acidic environment shifts the coverage by relieving the bottleneck in NO_2-to-*HNO conversion, promoting the overall urea formation kinetics. Notably, the calculations indicate that while some proton input is necessary, an excess could instead lead to $*NO_2$ being fully hydrogenated to $*NH_3$. Thus, the optimal pH is one that just sufficiently protonates the N intermediates to enable C–N coupling, but not so strongly as to favor ammonia over urea.

6. Tuning Microenvironment through PE

6.1. Mechanisms of PE in Modulating Reaction Microenvironments

PE is an advanced electrochemical strategy that employs oscillating potentials–alternating between a more positive (E_a) and more negative (E_c) voltage.[162] In contrast to conventional constant potential electrolysis (CPE), these potential pulses actively retune the catalyst/electrolyte interface in real time.[163] And PE can selectively enhance or suppress specific interfacial processes, offering dynamic control over reaction pathways. This dynamic modulation directly addresses several key limitations of CPE that hinder efficiency and selectivity in electrochemical conversions.[164]

First, under constant applied bias, catalysts often undergo gradual and irreversible changes in morphology, phase, or oxidation state at the surface. This leads to the loss of active sites, performance decay, and ultimately catalyst deactivation.[165] Second, a static cathodic potential continuously depletes reactants and accumulates products at the interface, resulting in concentration polarization. Furthermore, many electrochemical reactions involve multistep or multispecies mechanisms. A single fixed potential is often insufficient to simultaneously optimize all steps, entailing a trade-off between selectivity and yield due to kinetic mismatches.[166]

However, in each PE cycle, a high potential pulse can reoxidize or reconfigure the catalyst surface, removing poisons or reactivating sites, while a low potential pulse drives the desired reduction chemistry under refreshed conditions. This on/off alternation allows the system to avoid the continuous depletion or buildup of species that occurs under static polarization, instead periodically "resetting" the boundary layer composition. As a result, the catalyst surface and local electrolyte environment are constantly readjusted, active sites are regenerated, and reactants are replenished at the interface.[167,168] **Figure 19** schematically illustrates how these potential pulses mitigate catalyst deactivation and concentration gradients, creating a more favorable microenvironment for sustained reactions.[169]

Importantly, the benefits of PE have been clearly demonstrated in CO_2RR and NO_3RR, which serve as instructive case studies due to their relevance for electrochemical C–N coupling.[170–172] In the following sections, we outline the fundamental mechanisms by which PE controls the catalyst–electrolyte interface and enhances reaction performance, then review recent applications of PE in CO_2RR and NO_3RR. We highlight how pulsing improves catalyst stability and phase maintenance, boosts reactant delivery and local concentration control, and modulates reaction kinetics.[173,174] These insights will set the stage for discussing emerging uses of PE to optimize microenvironments in more complex electrochemical C–N coupling reactions.

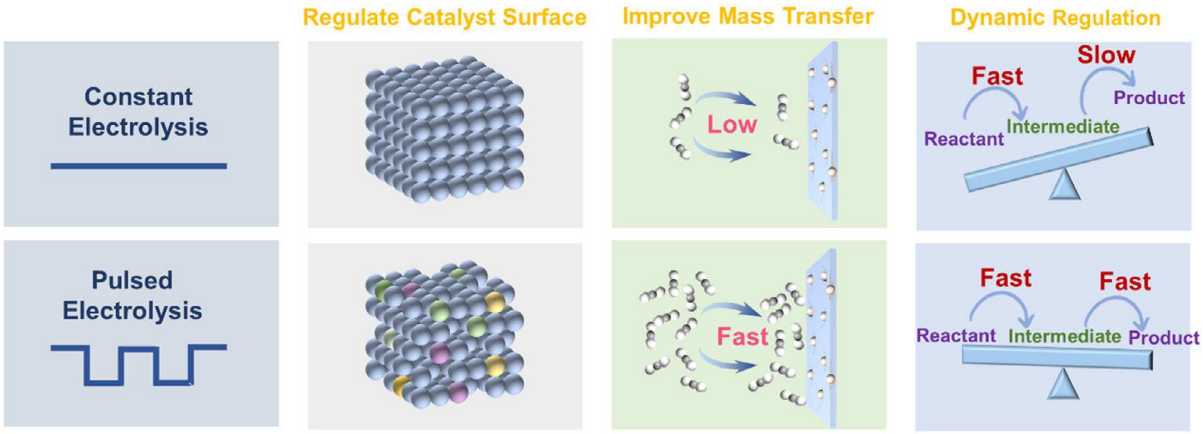

Figure 19. Demonstration of PE in modulating microenvironment-related motifs.

6.2. Leveraging PE for Microenvironmental Modulation in CO_2RR and NO_xRR

6.2.1. PE for Catalyst Preservation and Enhanced Performance in CO_2RR and NO_3RR

One of the advantages of PE is its ability to preserve active catalyst phases and maintain performance during reactions that would gradually deactivate under constant operation. This has been well exemplified in CO_2RR and NO_3RR on copper (Cu) catalysts, where pulsing helps retain crucial oxidation states and orchestrate multistep reaction pathways for improved outcomes.[166,175]

In CO_2 reduction, Metallic Cu is unique in its ability to produce C_{2+} products from CO_2.[14,176] However, under CPE, Cu surface structure undergoes unfavorable restructuring, leading to the loss of catalytic sites.[177,178] However, carefully designed pulse programs can restructure the catalyst in beneficial ways. Timoshenko et al. showed that alternating potentials can create a mixed-valence Cu surface while tuning the surface structure and composition of the copper catalyst, thereby improving the selectivity of the different products in the CO_2RR (**Figure 20**a).[179,180] Using Cu_2O nanocubes, they found that CPE yielded only ≈10% ethanol FE, whereas the PE (with E_c and E_a applied for 4 and 0.5 s, respectively) increased the ethanol FE by 1.7 times. Under pulsing, X-ray spectroscopy revealed that the catalyst surface maintained a coexistence of Cu^+ and Cu^0 species rather than fully reducing to Cu^0 as in the static case (Figure 20b).[181] This coexistence provides complementary CO adsorption sites, which promote an "asymmetric" CO dimerization, facilitating C–C coupling to C_2 products. Additionally, the repetitive oxidation/reduction caused the originally well-defined Cu_2O cubes to fragment into defect-rich agglomerates, while constant bias led to sintering and smooth facets. The pulse-induced defects and grain boundaries further helped to stabilize Cu^+ species and offered additional active sites for CO_2 conversion. The Cu catalyst in pulsed mode produced substantially more ethylene/ethanol and less hydrogen side-product, underscoring how pulse-driven surface dynamics can be harnessed to steer reaction selectivity. In contrast, excessively $E_a \approx +1.2$ V overoxidizes the interface (removing OH^- and Cu(I) species), which favors methane formation (≈48% FE_{CH4}) at the expense of C_2 products (Figure 20c). Operando XAS confirmed that pulsing at 0.9 V creates a rough (Figure 20d), Cu^+-rich surface conducive to C–C coupling, whereas 1.2 V pulses strip the catalyst and locally deplete hydroxide, tipping the mechanism toward CH_4. These findings highlight the importance of pulse amplitude in tuning catalyst phases and reaction pathways.

Cu-based materials are promising NO_3RR catalysts with a *d*-band center favorable for NO_3^- adsorption, but like CO_2RR, they suffer structural changes under constant operation.[7,182] Cu/Cu_2O heterojunction initially provides an active Cu^+–Cu^0 interface for nitrate reduction, but under the CPE, this interface degrades.[183] PE can prevent this deactivation by reoxidizing the catalyst transiently.[129] Bu et al. showed that during pulsed NO_3RR, each anodic interval momentarily oxidized Cu^0 back to CuO, and the subsequent cathodic pulse reduced CuO to Cu/Cu_2O again (**Figure 21**a).[184] This cyclic regeneration sustains highly active Cu^+/Cu^0 interfaces throughout the reaction. Under an optimized square-wave program ($E_c = -0.1$ V, $E_a = +1.0$ V, $t_a = t_c = 20$ s), the rate of the nitrate-to-nitrite step reached 315.3 μmol cm^{-2} h^{-1}, which is roughly 13 times higher than that under CPE (Figure 21b). PE achieved a nitrite FE of ≈63% with 91.6% selectivity, far outperforming the CPE (Figure 21c). These gains directly stem from the pulse-driven maintenance of the bifunctional Cu/Cu_2O surface, which continually provides the optimal adsorption sites for NO_3^- reduction to NO_2^-. In contrast, under CPE, the Cu_2O would be lost, and nitrate conversion stalls at a low rate (Figure 21c). Thus, by periodically reconstructing the catalyst during operation, PE keeps the nitrate reduction pathway in its most active state, dramatically accelerating the kinetics of the initial $NO_3^- \rightarrow NO_2^-$ conversion.

Beyond generating nitrite, the subsequent reduction of NO_2^- to NH_3 requires a delicate balance of *H coverage. A strongly negative potential supplies abundant *H for hydrogenation but also drives the HER and can destabilize the catalyst or intermediates; a milder potential avoids HER but may leave *H coverage too low to fully reduce NO_2^-.[185] To address this, Bu et al. developed a

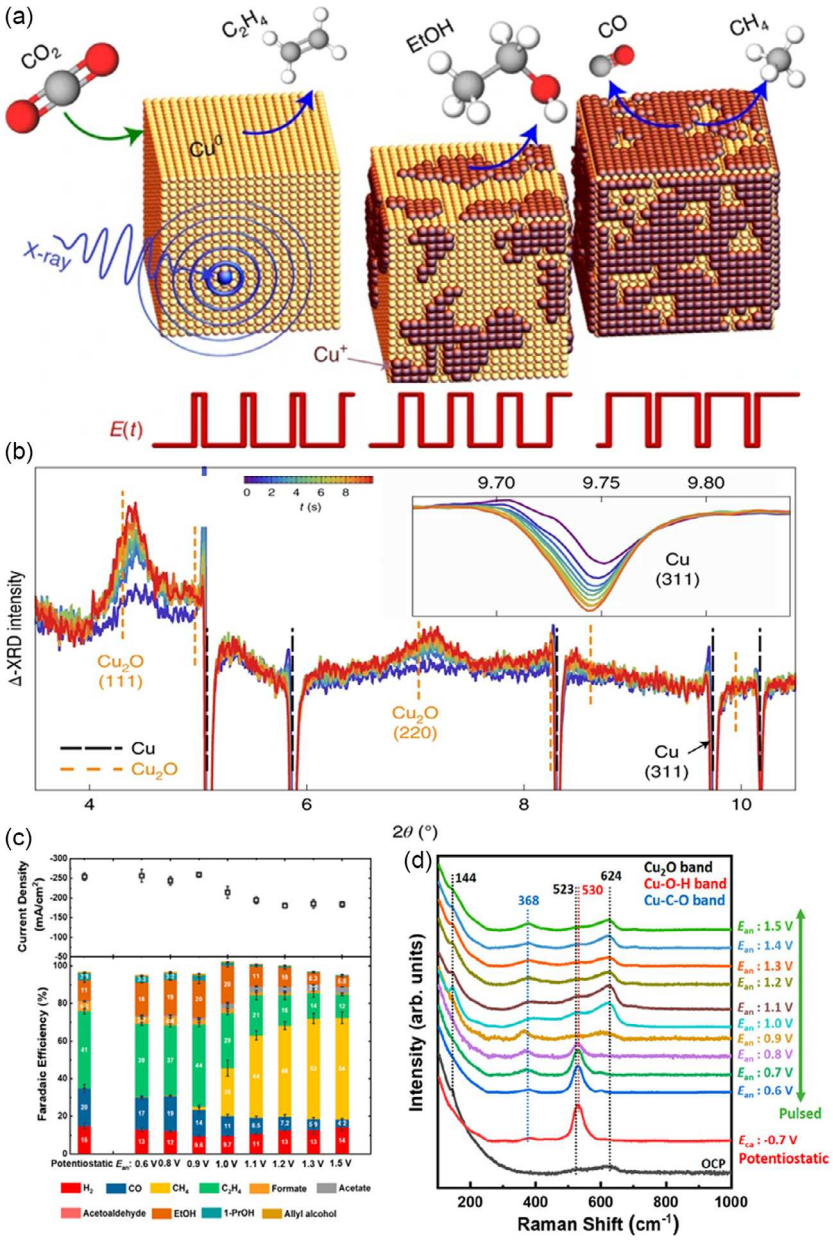

Figure 20. Schematic diagram and performance graph of pulsed CO_2RR. a) Schematic diagram of pulse regulation of catalyst surface structure. b) X-ray diffraction (XRD) spectrum under pulsed anode (E_a). The corresponding data at different times after the start of E_a is shown in the 2b (see color bars). Inset: zoomed-in region corresponding to the Bragg peak for Cu (311). Reproduced with permission.[180] Copyright 2022, Springer Nature. c) Current density and FE at a potentiostatic −0.7 V versus RHE and under PE conditions with the same $E_c = -0.7$ V versus RHE and different E_a. d) Operando surface-enhanced Raman spectra. Reproduced with permission.[192] Copyright 2021, American Chemical Society.

bifunctional catalyst under pulsing to decouple these steps (Figure 21d). In a Cu–Ni catalyst system, E_a was used to oxidize Ni into $Ni(OH)_2$ in situ ($E_a = +1.4$ V), and subsequent E_c (≈−1.0 V) then concurrently drove nitrate reduction on Cu and generated *H on the $Ni(OH)_2$ sites. The Cu active sites preferentially reduce NO_3^- (and NO_2^-), while adjacent $Ni(OH)_2$ provides a local supply of *H to hydrogenate the NO_2^- intermediate to NH_3. The PE periodically reforms the $Ni(OH)_2$ phase and yields a synergistic improvement. Using a Cu–Ni (1:1) electrode, the NH_3 FE reached ≈88%, and the ammonia production rate hit 583 μmol cm^{-2} h^{-1} at $E_c = -1.2$ V (Figure 21e,f). These metrics are markedly higher than any constant potential operation on either Cu or Ni alone. By integrating complementary active sites and leveraging the temporal separation of reactive steps, PE achieves a more optimal balance between intermediate generation and consumption in NO_3RR.

6.2.2. PE for Regulating Reaction Kinetics

In addition to preserving catalysts, PE fundamentally alters the mass transport and kinetics of electrochemical reactions by

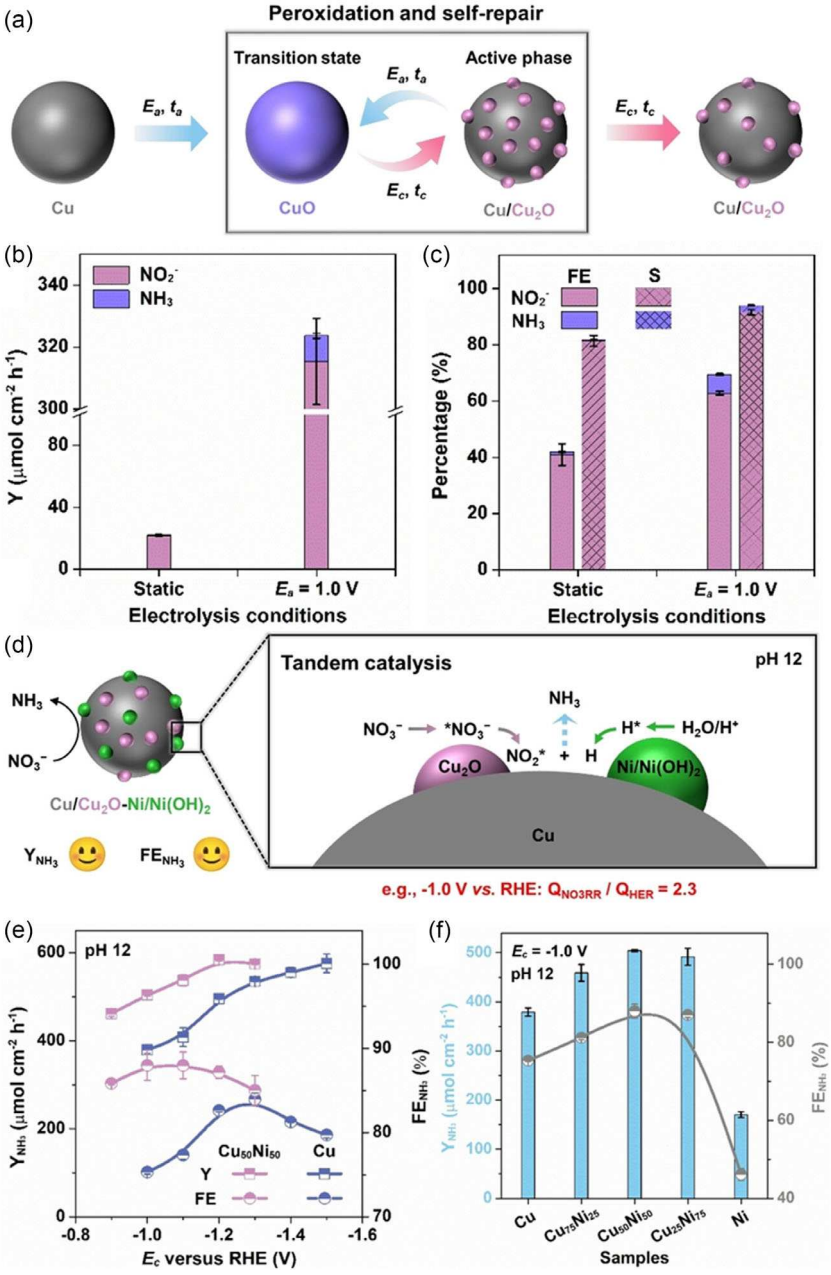

Figure 21. Schematic diagram and performance graph of pulsed NO_3RR. a) Schematic diagram illustrating the mechanism of Cu/Cu_2O formation during pulsing. b) Comparison of yield between PE ($E_a = 1.0$ V vs. RHE, $E_c = -0.1$ V vs. RHE; $t_a = t_a = 20$ s) and CPE (−0.1 V vs. RHE) electrolysis. c) Yield, FE, and selectivity of the reduction product under the conditions of 2b. d) Schematic diagram illustrating the mechanism of Cu/Cu_2O-$Ni/Ni(OH)_2$ formation during pulsing. e) The NH_3 yield rate and FE of Cu–Ni alloys at $E_c = -1.0$ V. f) The NH_3 yield rate and FE of different proportions Cu–Ni alloys at $E_c = -1.0$ V. (0.01 M KOH + 0.5 M Na_2SO_4 electrolyte, 400 rpm, $E_a = 1.4$ V, $E_c = -0.1$ V, $t_c = t_a = 5$ s). Reproduced with permission.[184] Copyright 2023 Wiley-VCH.

periodically disrupting the steady-state conditions at the interface.[166] In the CPE, reactant and ion transport to the electrode can become rate limiting as concentration gradients and EDL effects buildup.[186] PE, by contrast, introduces a transient perturbation that facilitates reactant migration, refreshes surface conditions, and accelerates reaction steps that are sluggish under CPE.

Under CO_2RR CPE, the rapid consumption of CO_2 at the cathode surface and the concomitant generation of OH^- cause a rise in local pH. This elevated pH converts CO_2 to (bi)carbonate in the near-surface region, creating a pronounced concentration gradient in the diffusion layer. This suppresses the CO_2RR reaction rate and selectivity, especially for C_2 products that require a high local CO coverage.

PE can alleviate these transport limitations.[187] Kim et al. used differential electrochemical mass spectrometry (DEMS) coupled with simulations to reveal how pulsing influences surface coverage of intermediates and local concentrations. In their study, a Cu film catalyst was subjected to alternating potentials of −0.8 and −1.15 V versus RHE in a CO_2-saturated electrolyte, and the

evolution of reaction species was tracked. Real-time mass signals showed that upon implementing PE, the CO_2 concentration near the electrode oscillated periodically instead of monotonically decaying (**Figure 22**a). During each E_a (−0.8 V), the local CO_2 was replenished from the bulk, and CO began accumulating on the Cu surface. During the E_c (−1.15 V), the stored CO_2 was rapidly consumed to produce CO and C_2 products, while the adsorbed CO coverage on Cu increased to a level higher than that under steady −1.15 V operation.[188] The PE created a dynamic alternation of surface conditions, the E_a favoring CO adsorption, and the E_c favoring C–C coupling of that intermediate. When both t_a and t_c are set to 10 s, the FE of CO_2RR increases from 68% under static conditions to 81%, while that of HER decreases from 22% under constant potential to 11%. This represents a significant shift in selectivity toward value-added products simply by modulating the potential periodically. To further elucidate the phenomena, the authors performed simulations of local pH and CO_2 concentration profiles during pulsing. The simulation revealed that the surface pH swung between ≈9.5 and ≈11.5 with each potential change (Figure 22b). Likewise, the local CO_2 concentration was predicted to oscillate between 30 mM (−0.8 V) and ≈13 mM (−1.15 V). Crucially, these swings were corroborated by the DEMS measurements (Figure 22c), confirming that pulsing indeed enforced a dynamic steady state quite unlike the monotonic depletion under CPE. Therefore, the alternating potentials ensure that neither the reactants are continuously depleted nor the unfavorable byproducts continuously accumulated.

In NO_3RR, the CPE creates a persistent electric field that repels negatively charged NO_3^- ions from the cathode, leading to a depletion of NO_3^- in the vicinity of the electrode.[40,189] This, coupled with the consumption of NO_3^-, establishes a steep concentration gradient where the surface NO_3^- level steadily drops. Additionally, positively charged products (e.g., NH_4^+) tend to accumulate near the cathode, further impeding incoming NO_3^-.[190] By periodically applying E_a, one can actively pull NO_3^- anions toward the cathode region and push ammonium product away, effectively "unsticking" the stagnant ion profiles (Figure 22d). Huang et al. conducted in situ Raman spectroscopy to unveil real-time local NO_3^- concentration changes. Under the CPE (−0.1 V vs. Ag/AgCl), the Raman signal for the nitrate ion (ν_{NO3} at 1050 cm^{-1}) steadily declined, indicating continuous depletion of NO_3^- at the interface as the reaction proceeded. However, when periodic +0.6 V pulses were applied to the anode, the nitrate Raman peak intensity recovered in each cycle (Figure 22e,f). This proves the replenishment of surface NO_3^- ions

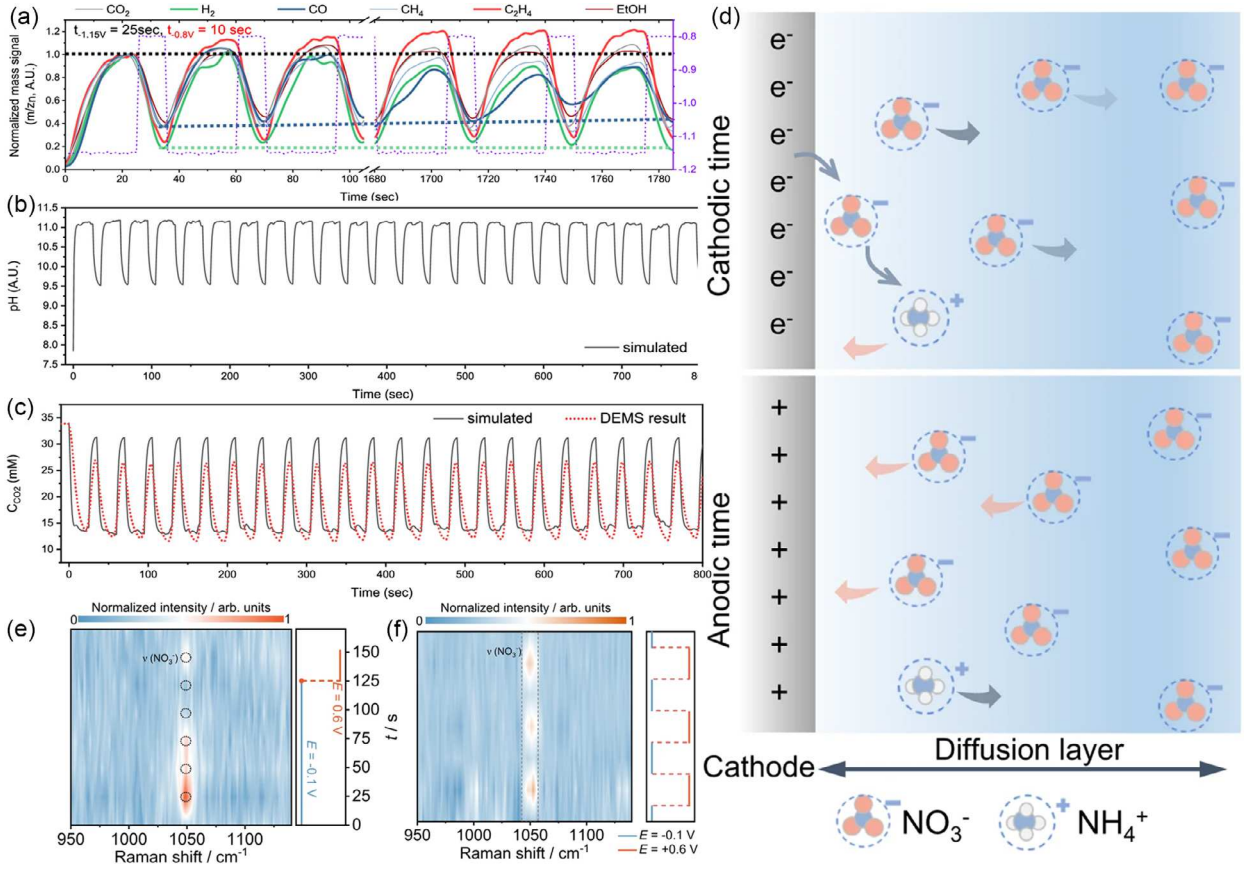

Figure 22. a) Used in simulation (black solid line) and measured (red dotted line) total current density. b) Simulated local pH and c) simulated (black solid line) and estimated local CO_2 concentration (red dotted line) based on DEMS result. Reproduced with permission.[187] Copyright 2020, American Chemical Society. d) Schematic diagram of the effect of pulse electrolysis on mass transfer in different species. e) In situ Raman spectra of $RuIn_3$/C. f) In situ Raman spectra of $RuIn_3$/C with three cycles. Reproduced with permission.[189] Copyright 2023, Springer Nature.

during the anodic interval. With pulsing at an average E_c of −0.1 V, the ammonia FE leapt from ≈65.8% to ≈97.6%, registering a nearly 1.5 times increase. At a more E_c (−0.2 V), the NH_3 production rate reached ≈2.7 mmol h^{-1} $mg_{Ru}{}^{-1}$ under PE, compared to only ≈1.2 mmol h^{-1} $mg_{Ru}{}^{-1}$ under CPE.

Thus, by breaking the spatio-temporal constraints of the diffusion layer, PE enables higher reaction rates and efficiencies for processes limited by ionic transport.[166] This paradigm is now being extended to other reactions where reactant delivery or intermediate removal is challenging. The ability of PE to modulate local concentration, electric field, and surface coverage on demand opens new opportunities to optimize complex electrocatalytic processes.[188] In the following section, we will see how these advantages of pulsing are leveraged in emerging C–N coupling reactions, where coordinating multiple reactants and multistep pathways is critical. This includes improved catalyst longevity, controlled intermediate buildup, and maintained reactant supply.

6.3. Applying Pulse Electrolysis to Catalysts and Key Species in C–N Coupling

Electrochemical C–N coupling by coreduction of carbon CO_2 and nitrogen sources presents complex, multistep reaction pathways. These processes inherit challenges from their CO_2RR and NO_xRR counterparts, but add further difficulty in synchronizing the generation and coupling of carbon- and nitrogen-based intermediates.[11,35] In this section, we discuss how PE leverages insights obtained from CO_2RR and NO_xRR and modulates catalyst–electrolyte microenvironment through 1) tuning catalyst oxidation states; 2) controlling local reactant concentrations, pH; and 3) adjusting surface intermediate coverages, thereby addressing the kinetic mismatches that hinder selective C—N bond formation.

6.3.1. Tuning Catalyst Valence States for Tandem C–N Coupling

PE's capability to tune the valence states of catalytically active species has also proved useful in C–N coupling reactions. He et al. exemplified this with the PE strategy to synthesize aromatic amines from CO_2 and $NO_2{}^-$ in a single reactor.[191] The reaction was designed in two steps: 1) cathodic reduction of $NO_2{}^-$ to NH_3 on a low-coordinated Cu nanocoral (LC-Cu NC) cathode, and 2) oxidative Chan–Lam coupling of the generated NH_3 with an arylboronic acid to form an aryl amine (**Figure 23**a).[174] A Cu(II) homogeneous catalyst is needed for the Chan–Lam C–N coupling, but it cannot survive under the CPE. By employing PE, the authors enabled these steps to proceed in one continuous process.[192]

Under the CPE, the Chan–Lam step stagnated, and the aniline yield was only ≈25%. By pulsing between $E_c \approx -1.1$ V (Ag/AgCl) and a brief anodic bias, the yield of aniline tripled to ≈75%. This threefold increase in aniline production underscores how valence modulation can unlock reaction pathways unattainable in static operation. The authors further demonstrated the versatility of this method by extending it to various arylboronic acid derivatives, achieving high yields of functionalized primary anilines under pulsed conditions (Figure 23b). They also integrated a third component into the reaction by using pulsing to drive a cascade where electroreduced $NO_2{}^-$ (as $*NH_2OH$) couples with an aldehyde (forming an oxime) and an alkyne to produce a 1,2,3-triazole heterocycle (Figure 23c). This demonstrated case highlights that PE enables multistep C—N bond-forming sequences in one pot. By alternately creating a strongly reducing surface (Cu^0/Cu^+) and a reoxidized Cu(II) catalyst, the system avoids the need for separate reagents or electrodes for the two steps. Such operando valence tuning is especially valuable for C–N coupling cascades.

6.3.2. Regulating the Local Microenvironment to Enhance C–N Coupling and Suppress HER

Beyond the catalyst surface, pulsing also regulates the local pH, ion distribution, and reactant flux to optimize C–N coupling conditions. In $CO_2/NO_3{}^-$ coelectrolysis, both CO_2 and $NO_3{}^-$ (or their reduced intermediates like *CO and $*NH_2$) must be sufficiently available at the interface to couple; due to the different reduction units of the two, the conditions that favor one often hinder the other.[156] PE offers a way out of this dilemma by time-multiplexing different conditions within each cycle, periodically refreshing the interfacial environment to alleviate build-ups of unfavorable conditions.

Hu et al. provided a compelling demonstration of microenvironment control via pulsing in the context of electrocatalytic urea synthesis.[173] In the CPE, they found that no single static potential could maximize urea formation: A strongly negative potential (−0.8 V vs. RHE) was needed to generate the key $*NH_2$ and *CO intermediates, but at the cost of intense HER and CO_2 loss. This also led to severe electrostatic repulsion of $NO_3{}^-$ anions from the negatively charged cathode, starving the surface of nitrate. On the other hand, a less negative potential (−0.2 V) greatly suppressed HER and allowed easier $NO_3{}^-$ transport to the cathode (lower repulsion), but produced far fewer CO/NH_2 intermediates for C–N coupling. The researchers recognized this trade-off and implemented a pulse regime alternating between −0.2 and −0.8 V to capture the benefits of each. Using a ion tetraphenylporphyrin/carbon nanotubes (Fe-TPP/CNT) molecular catalyst, pulsing between −0.2 and −0.8 V boosted the urea FE to 27.7%, compared to only 19.1% under a constant −0.8 V bias. Simultaneously, unwanted products, such as H_2, CO, and NH_3 byproducts, were evidently suppressed under pulse conditions, as evidenced by mass spectra shown in **Figure 24**a–c. Notably, the general trends held across multiple catalysts (ZnO, CuPd), attesting that the pulsing benefits are not idiosyncratic to Fe-porphyrin systems. Operando Attenuated Total Reflection surface-enhanced infrared absorption spectroscopy (Operando ATR-SEIRAS spectroscopy) studies showed increasing coverage of *CO and $*NH_2$ on the catalyst surface as pulsing progressed (Figure 24d). Theoretical modeling further revealed that pulsing induces a drop in local pH near the cathode, whereas a constant high cathodic bias maintains a strongly alkaline interface

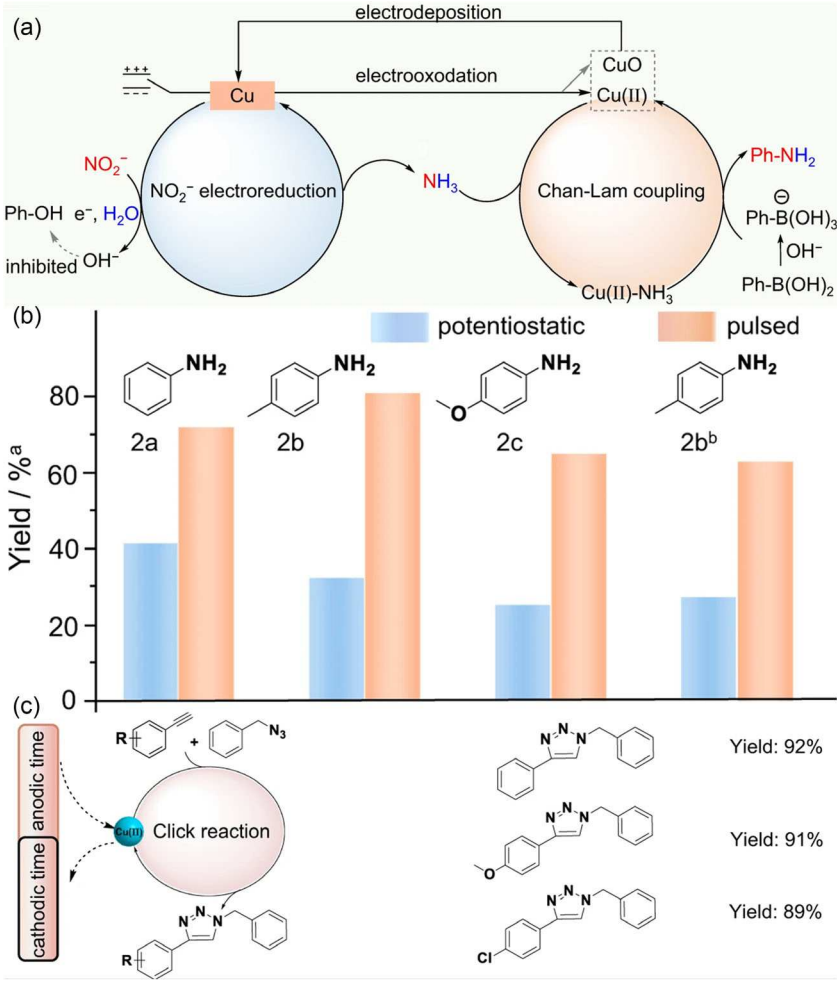

Figure 23. Mechanistic illustration and broad application of pulse-assisted one-pot synthesis strategies in two-step C–N coupling reactions. a) Schematic of the mechanism of the pulse reaction of NO_2^- with phenylboronic acid to form aromatic amines. b) Comparison of the yield of functionalized primary amines obtained by pulse strategy and by adding additional Cu(II) under constant potential. c) The pulsed electrochemical method for the Click reaction. Reproduced with permission.[174] Copyright 2023, Springer Nature.

(Figure 24e).[45] This in situ acidification under pulses prevents CO_2 from being SEQUESTered as carbonate, instead keeping CO_2 available for reduction. Simulations of NO_3^- migration showed that the local NO_3^- concentration was as high as 2.67 mol m^{-3} at a potential of −0.2 V (RHE), which is 34 times higher than the potential of −0.8 V (RHE) (0.078 mol m^{-3}) (Figure 24f). This dramatic enhancement underscores how relieving electrostatic repulsion during E_a (at −0.2 V) lets the reaction zone refuel with fresh NO_3^-. In summary, PE tailors the local reaction environment through accumulating reactants (CO_2, NO_3^-) in the double layer, lowering local pH (mitigating carbonate formation), and periodically sweeping away builtup charges, all of which create a more favorable milieu for C–N coupling.

6.3.3. Optimizing Intermediate Surface Coverage for Efficient C–N Coupling

The third aspect of pulsed modulation is its effect on the adsorption–desorption dynamics of reaction intermediates at the electrode surface. Pulsing can tune the coverage of key *C and *N intermediates by intermittently disrupting the equilibrium at the interface. Under CPE, intermediates may either accumulate to blocking levels or be removed too quickly, both scenarios that can hinder coupling.[26,98,193] By contrast, a well-designed PE can balance intermediate generation and consumption, ensuring that both coupling partners reside on the surface concurrently at optimal coverage. In fact, many benefits of pulsing (enhanced reactant delivery, electric double-layer perturbation) manifest as changes in surface intermediatepopulations. However, targeted evidence for intermediate coverage effects comes from studies that directly monitored surface species and reaction rates under pulsed versus static conditions.

Gerke et al. recently showed that pulsed potentials markedly improve the surface chemistry for CO_2/NO_3^- coupling to urea on a gold catalyst.[155] In their work, short pulses ($E_a = -0.2$ V, $E_c = -0.4$ V vs. RHE) increased the urea FE from 26% to 42.4%. Although the time-averaged potential in the pulse experiment was similar to the constant case (−0.3 V), the pulsed operation

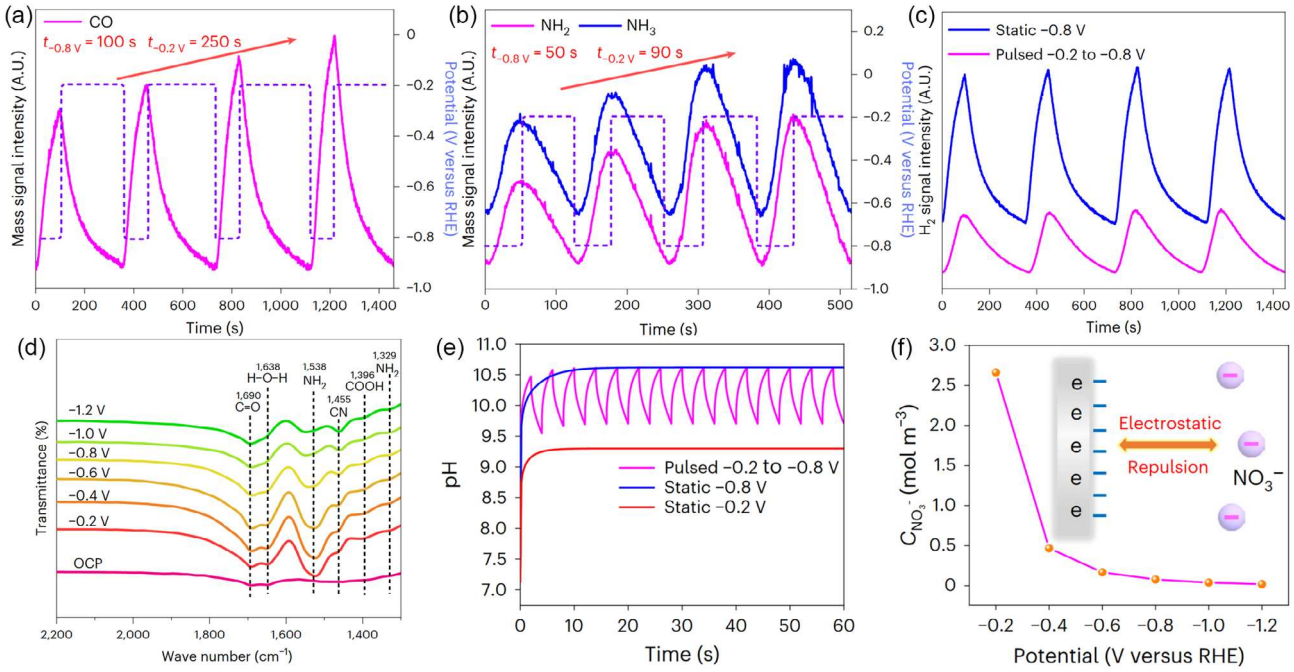

Figure 24. CO_2 and NO_3^- coreduction to urea catalyzed by Fe-TPP/CNT catalyst. a–c) Operando mass spectrum, Variation of a) CO, b) NH_3, and c) H_2 signals with time in PE. d) Operando ATR-SEIRAS spectroscopy measurements for the CO_2/NO_3^- coreduction. e) pH distribution of PE and static electrolysis within a 100 μm boundary layer. f) Simulated NO_3^- concentration around the electrode at different potentials. Reproduced with permission.[173] Copyright 2024, Springer Nature.

led to significantly higher urea selectivity, indicating a fundamentally different interface condition. Using time-resolved SEIRAS, the authors found that under pulsing, a broad Infrared Spectroscopy (IR) band for NO_3^- adsorption at ≈1350 cm^{-1} grew strongly, while a band for NO_2^- at ≈1270 cm^{-1} showed a negative-going signal (**Figure 25**a). This implies that during pulses, NO_3^- continually adsorbs/refills at the interface and NO_2^- (a key intermediate) is rapidly consumed as it forms, rather than accumulating. Under constant polarization, in contrast, these spectral features remained weak or absent (Figure 25b), suggesting a more stagnant interfacial state. In essence, the pulsed electric field reorients the interfacial ions and dipoles, transiently breaking the static double-layer structure. This facilitates a greater influx of NO_3^- to the surface and immediately drives its reduction onward, so that $*NO_2^-$ intermediates are promptly converted instead of poisoning the surface or being reduced to NH_3. The result is an elevated surface coverage of the $*CO/*NH_2$ pairing needed for urea formation, directly correlating with the higher observed FE for urea.[187]

Complementary evidence comes from Qiu et al., who applied pulses to a $CuSiO_x$ catalyst for urea synthesis.[194] They focused on overcoming the electrostatic screening and repulsion effects that limit NO_3^- access and intermediate buildup at negative electrodes. Under an optimally PE, they achieved a urea selectivity of 79.0% at −0.2 V, a 39% increase over the CPE. At a more reducing potential (−0.6 V), the pulsed approach yielded 1606 μg h^{-1} mg_{cat}^{-1} of urea, which was 2.4 times higher than that from the steady state (Figure 25c). Furthermore, the online DEMS test results showed that the NO_2^- signal at −0.2 V and the coupled intermediate signal at −0.6 V were enhanced (Figure 25d). These were attributed to pulses alleviating interfacial ion buildup and concentration polarization, again ensuring that NO_3^- ions are continuously replenished to combine with CO_2-derived species. A schematic comparison of constant versus pulsed operation illustrates how a static cathode quickly forms a depleted NO_3^- layer and high local pH, whereas pulsing keeps bringing NO_3^- to the surface and prevents charge saturation in the double layer, thereby maintaining abundant $*NO_3/*NO_2$ and *CO intermediates, leading to higher urea productivity (Figure 25e,f).[50]

In conclusion, PE has emerged as a powerful technique to optimize electrochemical C–N coupling reactions through multifaceted control of the reaction environment. The above examples demonstrate that alternating potentials can 1) stabilize or activate specific catalyst states; 2) dynamically adjust local pH and reactant concentrations; and 3) balance the generation and utilization of critical C–N intermediates. These effects work in concert to alleviate the fundamental challenges in CO_2/NO_3^- coreduction and related C–N formations, including catalyst deactivation, competing side reactions (like HER), mass transport limitations, and mismatched intermediate kinetics.[195,196] By tailoring conditions in the time domain, pulsed schemes achieve outcomes beyond the reach of conventional static electrolysis, from higher product yields and selectivities to lower energy inputs. This strategy thus offers a new level of control in electrocatalysis, opening avenues for more efficient and sustainable production of value-added organonitrogen compounds.

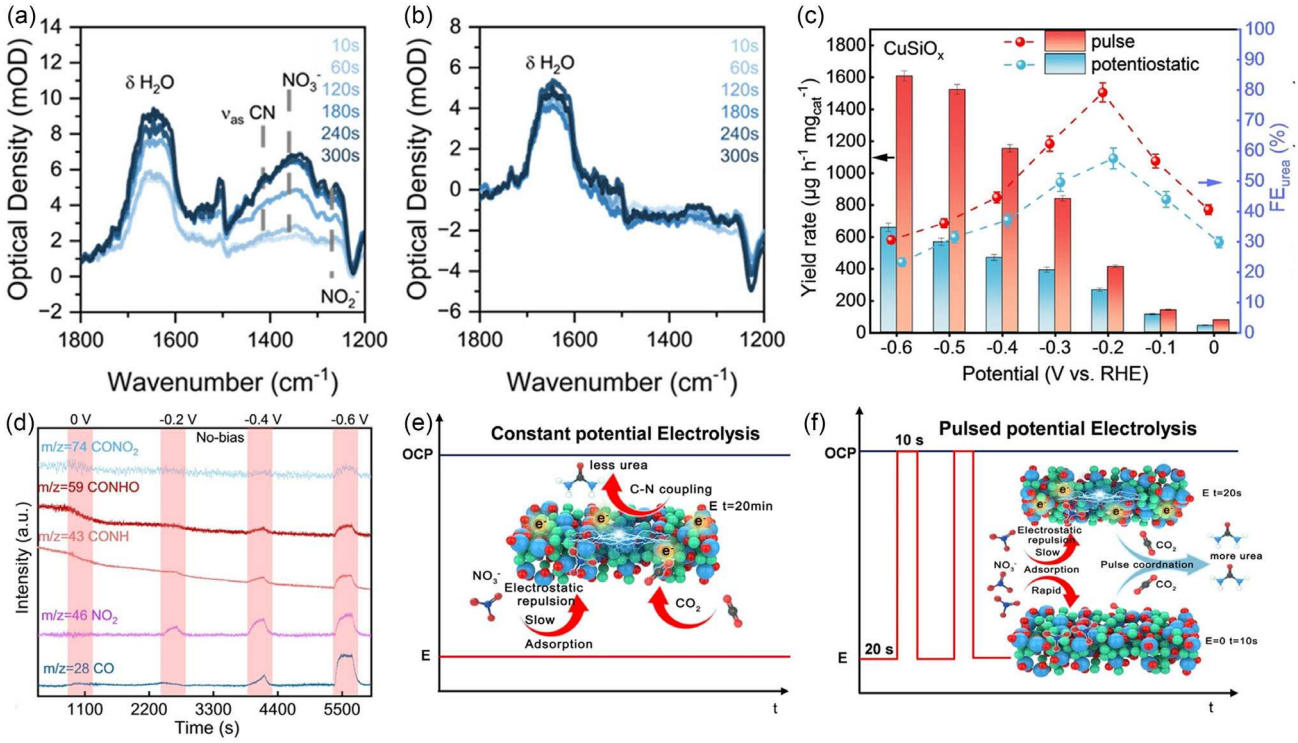

Figure 25. a) CPE (−0.4 V vs. RHE) and b) PE (−0.4 and −0.2 V vs. RHE)r in a CO_2 sat. 0.1 M KNO_3 electrolyte. Reproduced with permission.[155] Copyright 2023, American Chemical Society. c) Urea FEs and yields corresponding to $CuSiO_x$ at different constant and pulsed potentials. d) Online DEMS of $CuSiO_x$ in electrolyte of 0.1 M KNO_3 and 0.1 M $KHCO_3$. Schematic of e) electrostatic potential and f) PE. Reproduced with permission.[194] Copyright 2024 Wiley-VCH GmbH.

7. Conclusions and Future Perspectives

In this review, we systematically discuss how deliberate modulation of catalysts, electrolytes, and PE conditions, key modulators of the electrochemical microenvironment, can alleviate mass transport limitations, suppress side reactions, and enhance the reaction kinetics of C–N coupling, thereby optimizing overall catalytic performance. These three components share a tightly interdependent relationship wherein synergistic effects coexist with individual contributions. They can collectively enhance performance through cooperative interactions, while each also functions as a discrete variable capable of independently modulating the reaction pathway.

Rational catalyst microenvironment design enables regulation of surface defects to tune electronic structure, optimization of coordination structures, and construction of targeted morphologies. These modifications collectively increase the active surface area and foster a favorable local reaction environment, promoting the adsorption of key intermediates and ultimately governing the reaction kinetics. Likewise, the electrolyte can be tuned—through local pH, ion identity, and concentration—to reconfigure the EDL, suppress competitive side reactions, and stabilize key intermediates. Finally, dynamic PE provides time-dependent modulation of reaction conditions; by periodically reconstructing the catalyst surface and modulating local reactant concentrations, this approach mitigates catalyst deactivation and minimizes concentration gradients, thereby maintaining optimal conditions for C–N coupling throughout the reaction.

While microenvironment engineering strategies and approaches developed through CO_2RR and NO_xRR-centered studies have demonstrated successful translation to C–N coupling, the exact effects on the reaction mechanisms and performances might be inconsistent between coreduction and monoreduction reaction systems. For instance, the order of cation effects in C–N coupling differs from those observed in CO_2RR and NO_3RR. This disparity is likely due to distinct mechanisms by which cations influence these different reactions. Specifically, studies show that Cs^+ enhances the interfacial electric field in CO_2RR but slows protonation kinetics within the electrical double layer in NO_3RR. Consequently, the promotion effects of Cs^+ for C–N coupling are not as pronounced as that observed in CO_2RR. This phenomenon suggests more in-depth investigation to deconvolute the microenvironmental factors for the more complex C–N coupling reaction system is needed. To fully understand and effectively apply microenvironment engineering in future C–N coupling research, we propose several key future research directions.

7.1. Synergistic Microenvironment Optimization

While many studies have examined conventional catalyst morphologies, cation effects, and square-wave PE, the extensive tunability of electrolyte ion species and pulse waveforms presents new opportunities for improvement. Exploring alternative electrolyte ions (e.g., halides or organic ions) and nontraditional waveforms (such as sine or stepped waves) could further enhance

electrolyte modulation and pulsing strategies. Given the inherently synergistic nature of catalyst, electrolyte, and pulse parameters, it is crucial to co-optimize all three elements and investigate the mechanisms behind their interactions. Such an integrated approach will ultimately facilitate the creation of an ideal microenvironment conducive to efficient C–N coupling.

7.2. Development of In Situ Detection Techniques

Although microenvironment regulation has been achieved via pulsed methods, tailored catalysts, and electrolyte design, the diversity and transient nature of intermediates in C–N coupling systems necessitate more advanced in situ diagnostic methods. Improving the sensitivity and temporal resolution of analytical techniques to monitor catalytic surface changes and the dynamic evolution of intermediates within the reaction microenvironment is essential. Such enhanced capabilities would provide powerful insights into reaction mechanisms and facilitate the identification of active sites.

7.3. Multiscale Simulation and Modeling

C–N coupling systems are inherently complex, with reaction behavior closely linked to catalyst morphology, local pH, and ionic species in the microenvironment. This complexity demands sophisticated modeling approaches. By leveraging recent advances in computational science, multiscale modeling techniques that integrate artificial intelligence and machine learning can comprehensively account for factors like catalyst structure, mass transport, and electrolyte effects, thereby enabling a deeper understanding of the microenvironment's dynamic evolution. Insights from these models can in turn guide catalyst design, tailor the EDL at the electrode–electrolyte interface, and optimize pulse parameters (e.g., duty cycle). Ultimately, such computational guidance aims to enhance catalytic performance and expand the variety of C–N coupled products achievable.

Acknowledgements

J.B., X.C., and L.Y. acknowledge the Jiangsu Specially-Appointed Professor Program. L.Y. and N.S. acknowledge the W. M. Keck Foundation and National Science Foundation (Award #2247194) for financial support.

Conflict of Interest

The authors declare no conflict of interest.

Keywords: electrocatalysts · electrochemical C–N coupling · microenvironments · pH and cation effects · pulsed electrolysis

[1] N. Mac Dowell, P. S. Fennell, N. Shah, G. C. Maitland, *Nat. Clim. Change* **2017**, *7*, 243.
[2] M. H. Barecka, J. W. Ager, A. A. Lapkin, *iScience* **2021**, *24*, 102514.
[3] X. Zhang, Y. Wang, C. Liu, Y. Yu, S. Lu, B. Zhang, *Chem. Eng. J.* **2021**, *403*, 126269.
[4] C. Tang, Y. Zheng, M. Jaroniec, S.-Z. Qiao, *Angew. Chem., Int. Ed.* **2021**, *60*, 19572.
[5] P. De Luna, C. Hahn, D. Higgins, S. A. Jaffer, T. F. Jaramillo, E. H. Sargent, *Science* **2019**, *364*, eaav3506.
[6] A. Hermawan, T. Amrillah, V. N. Alviani, J. Raharjo, Z. W. Seh, N. Tsuchiya, *J. Environ. Manage.* **2023**, *334*, 117477.
[7] C. Chen, X. Zhu, X. Wen, Y. Zhou, L. Zhou, H. Li, L. Tao, Q. Li, S. Du, T. Liu, D. Yan, C. Xie, Y. Zou, Y. Wang, R. Chen, J. Huo, Y. Li, J. Cheng, H. Su, X. Zhao, W. Cheng, Q. Liu, H. Lin, J. Luo, J. Chen, M. Dong, K. Cheng, C. Li, S. Wang, *Nat. Chem.* **2020**, *12*, 717.
[8] R. I. Masel, Z. Liu, H. Yang, J. J. Kaczur, D. Carrillo, S. Ren, D. Salvatore, C. P. Berlinguette, *Nat. Nanotechnol.* **2021**, *16*, 118.
[9] M. Jiang, Q. Zhu, X. Song, Y. Gu, P. Zhang, C. Li, J. Cui, J. Ma, Z. Tie, Z. Jin, *Environ. Sci. Technol.* **2022**, *56*, 10299.
[10] Z. Tao, C. L. Rooney, Y. Liang, H. Wang, *J. Am. Chem. Soc.* **2021**, *143*, 19630.
[11] J. Li, Y. Zhang, K. Kuruvinashetti, N. Kornienko, *Nat. Rev. Chem.* **2022**, *6*, 303.
[12] C. Lv, L. Zhong, H. Liu, Z. Fang, C. Yan, M. Chen, Y. Kong, C. Lee, D. Liu, S. Li, J. Liu, L. Song, G. Chen, Q. Yan, G. Yu, *Nat. Sustainability* **2021**, *4*, 868.
[13] S. Qureshi, M. Mumtaz, F. K. Chong, A. Mukhtar, S. Saqib, S. Ullah, M. Mubashir, K. S. Khoo, P. L. Show, *Chemosphere* **2022**, *291*, 132806.
[14] A. D. Handoko, F. Wei, Jenndy, B. S. Yeo, Z. W. Seh, *Nat. Catal.* **2018**, *1*, 922.
[15] J. Li, N. Kornienko, *Chem. Sci.* **2022**, *13*, 3957.
[16] H. Mei, Q. Hua, L. Su, J. Li, Y. Ge, Z. Huang, *J. Mater. Chem. A* **2024**, *12*, 20507.
[17] B. Hu, R. Lu, W. Wang, Y. Zhou, D. K. D. Jaswanthi, Z. Wu, Z. Wang, L. Wang, J. Am, *Chem. Soc.* **2025**, *147*, 21764.
[18] Y. Luo, K. Xie, P. Ou, C. Lavallais, T. Peng, Z. Chen, Z. Zhang, N. Wang, X.-Y. Li, I. Grigioni, B. Liu, D. Sinton, J. B. Dunn, E. H. Sargent, *Nat. Catal.* **2023**, *6*, 939.
[19] H. Wang, Y. Jiang, S. Li, F. Gou, X. Liu, Y. Jiang, W. Luo, W. Shen, R. He, M. Li, *Appl. Catal., B* **2022**, *318*, 121819.
[20] C. Kim, J. C. Bui, X. Luo, J. K. Cooper, A. Kusoglu, A. Z. Weber, A. T. Bell, *Nat. Energy* **2021**, *6*, 1026.
[21] M. Schreier, P. Kenis, F. Che, A. S. Hall, *ACS Energy Lett.* **2023**, *8*, 3935.
[22] M. Liu, Y. Ma, S. Zhang, M. Chen, L. Wu, *Adv. Sci.* **2024**, *11*, 2309200.
[23] Q. Song, Y. Zhang, L. Gu, M. Kuang, J. Yang, *Coord. Chem. Rev.* **2025**, *522*, 216248.
[24] J. Pan, H. Ding, X. Yang, X. Liang, S. Wu, M. Zhang, S. Li, S. Zheng, F. Pan, *ACS Catal.* **2025**, *15*, 457.
[25] Y. Guo, Y. Li, X. Wang, L. Wang, Z. Wang, *Chem. Eng. J.* **2024**, *499*, 155920.
[26] Y. Wang, X. Zhu, Q. An, X. Zhang, X. Wei, C. Chen, H. Li, D. Chen, Y. Zhou, Q. Liu, H. Shao, S. Wang, *Angew. Chem., Int. Ed.* **2024**, *63*, e202410938.
[27] S. Paul, A. Adalder, U. K. Ghorai, *Mater. Chem. Front.* **2023**, *7*, 3820.
[28] D. Jiao, Y. Dong, X. Cui, Q. Cai, C. R. Cabrera, J. Zhao, Z. Chen, *J. Mater. Chem. A* **2023**, *11*, 232.
[29] J. Liu, X. Guo, T. Frauenheim, Y. Gu, L. Kou, *Adv. Funct. Mater.* **2024**, *34*, 2313420.
[30] X. Zhang, X. Zhu, S. Bo, C. Chen, M. Qiu, X. Wei, N. He, C. Xie, W. Chen, J. Zheng, P. Chen, S. P. Jiang, Y. Li, Q. Liu, S. Wang, *Nat. Commun.* **2022**, *13*, 5337.
[31] X. Wei, Y. Liu, X. Zhu, S. Bo, L. Xiao, C. Chen, T. T. T. Nga, Y. He, M. Qiu, C. Xie, D. Wang, Q. Liu, F. Dong, C.-L. Dong, X.-Z. Fu, S. Wang, *Adv. Mater.* **2023**, *35*, 2300020.
[32] N. Meng, X. Ma, C. Wang, Y. Wang, R. Yang, J. Shao, Y. Huang, Y. Xu, B. Zhang, Y. Yu, *ACS Nano* **2022**, *16*, 9095.
[33] M. Jiang, H. Wang, M. Zhu, X. Luo, Y. He, M. Wang, C. Wu, L. Zhang, X. Li, X. Liao, Z. Jiang, Z. Jin, *Chem. Soc. Rev.* **2024**, *53*, 5149.
[34] Y. Wu, Z. Jiang, Z. Lin, Y. Liang, H. Wang, *Nat. Sustainability* **2021**, *4*, 725.
[35] Y. Zhong, H. Xiong, J. Low, R. Long, Y. Xiong, *eScience* **2023**, *3*, 100086.
[36] J. Lan, Z. Wei, Y.-R. Lu, D. Chen, S. Zhao, T.-S. Chan, Y. Tan, *Nat. Commun.* **2023**, *14*, 2870.
[37] S. Kuang, T. Xiao, H. Chi, J. Liu, C. Mu, H. Liu, S. Wang, Y. Yu, T. J. Meyer, S. Zhang, X. Ma, *Angew. Chem., Int. Ed.* **2024**, *63*, e202316772.
[38] C. Lu, Y. Su, J. Zhu, J. Sun, X. Zhuang, *Chem. Commun.* **2023**, *59*, 6827.
[39] X. Tan, H. Zhu, C. He, Z. Zhuang, K. Sun, C. Zhang, C. Chen, *Chem. Sci.* **2024**, *15*, 4292.
[40] L. Gu, Y. Cong, Z. Wu, F. Xie, Y. Hua, H. Xu, J. Yang, *Adv. Funct. Mater.* **2025**, 2500316.
[41] Y. Li, M. S. Hassan, X. Zhao, A. L. Rogach, *Adv. Mater.* **2025**, *37*, 2418146.
[42] P.-P. Yang, M.-R. Gao, *Chem. Soc. Rev.* **2023**, *52*, 4343.

[43] S. R. Waghela, A. Adalder, K. Mitra, U. K. Ghorai, *ChemCatChem* **2025**, *17*, e202401565.
[44] H. Wu, A. Singh-Morgan, K. Qi, Z. Zeng, V. Mougel, D. Voiry, *ACS Catal.* **2023**, *13*, 5375.
[45] J. Ni, Q. Cheng, S. Liu, M. Wang, Y. He, T. Qian, C. Yan, J. Lu, *Adv. Funct. Mater.* **2023**, *33*, 2212483.
[46] L. Dong, W. Ge, Y. Fan, W. Zhang, H. Jiang, Y. Zhao, C. Li, *AIChE J.* **2024**, *70*, e18271.
[47] J. Cho, F. M. Alamgir, S. S. Jang, *ChemSusChem* **2025**, *18*, e202401673.
[48] A. S. Malkani, J. Anibal, B. Xu, *ACS Catal.* **2020**, *10*, 14871.
[49] J. Gu, S. Liu, W. Ni, W. Ren, S. Haussener, X. Hu, *Nat. Catal.* **2022**, *5*, 268.
[50] Y. Xu, W. Gao, Z.-X. Chen, Z. Yin, Z. Chen, X. Chang, M.-J. Cheng, B. Xu, *ACS Catal.* **2024**, *14*, 10829.
[51] Z. Li, L. Wang, L. Sun, W. Yang, *J. Am. Chem. Soc.* **2024**, *146*, 23901.
[52] M. He, R. Li, C. Cheng, C. Liu, B. Zhang, *Nat. Commun.* **2024**, *15*, 5231.
[53] C. Chen, H. Jin, P. Wang, X. Sun, M. Jaroniec, Y. Zheng, S.-Z. Qiao, *Chem. Soc. Rev.* **2024**, *53*, 2022.
[54] N. Ye, K. Wang, Y. Tan, Z. Qian, H. Guo, C. Shang, Z. Lin, Q. Huang, Y. Liu, L. Li, Y. Gu, Y. Han, C. Zhou, M. Luo, S. Guo, *Nat. Synth.* **2025**, *4*, 799.
[55] Y. Cheng, Q. Li, M. I. B. Salaman, C. Wei, Q. Wang, X. Ma, B. Liu, A. B. Wong, *J. Am. Chem. Soc.* **2025**, *147*, 12438.
[56] Z.-S. Zhu, S. Zhong, C. Cheng, H. Zhou, H. Sun, X. Duan, S. Wang, *Chem. Rev.* **2024**, *124*, 11348.
[57] W. Ye, Y. Zhang, L. Chen, F. Wu, Y. Yao, W. Wang, G. Zhu, G. Jia, Z. Bai, S. Dou, P. Gao, N. Wang, G. Wang, *Angew. Chem., Int. Ed.* **2024**, *63*, e202410105.
[58] Z. Chen, Y. Zhao, H. Huang, G. Liu, H. Zhang, Y. Yan, H. Li, L. Liu, M. Liu, D. Wang, J. Zeng, *J. Am. Chem. Soc.* **2025**, *147*, 18737.
[59] K. Jiang, S. Siahrostami, T. Zheng, Y. Hu, S. Hwang, E. Stavitski, Y. Peng, J. Dynes, M. Gangisetty, D. Su, K. Attenkofer, H. Wang, *Energy Environ. Sci.* **2018**, *11*, 893.
[60] J. Wang, M. Sun, H. Xu, F. Hao, Q. Wa, J. Su, J. Zhou, Y. Wang, J. Yu, P. Zhang, R. Ye, S. Chu, B. Huang, M. Shao, Z. Fan, *ACS Nano* **2024**, *18*, 7192.
[61] Y. Pan, R. Lin, Y. Chen, S. Liu, W. Zhu, X. Cao, W. Chen, K. Wu, W.-C. Cheong, Y. Wang, L. Zheng, J. Luo, Y. Lin, Y. Liu, C. Liu, J. Li, Q. Lu, X. Chen, D. Wang, Q. Peng, C. Chen, Y. Li, *J. Am. Chem. Soc.* **2018**, *140*, 4218.
[62] S. Wei, Y. Xu, T. Song, H. Dai, F. Li, X. Gao, Y. Zhai, S. Gong, R. Li, X. Zhang, K. Chan, *J. Am. Chem. Soc.* **2025**, *147*, 4219.
[63] J. Jiao, X. Kang, J. Yang, S. Jia, Y. Peng, S. Liu, C. Chen, X. Xing, M. He, H. Wu, B. Han, *J. Am. Chem. Soc.* **2024**, *146*, 15917.
[64] L. Lin, H. Li, Y. Wang, H. Li, P. Wei, B. Nan, R. Si, G. Wang, X. Bao, *Angew. Chem., Int. Ed.* **2021**, *60*, 26582.
[65] W. W. Kramer, C. C. L. McCrory, *Chem. Sci.* **2016**, *7*, 2506.
[66] T. L. Soucy, W. S. Dean, J. Zhou, K. E. Rivera Cruz, C. C. L. McCrory, *Acc. Chem. Res.* **2022**, *55*, 252.
[67] K. E. Rivera Cruz, Y. Liu, T. L. Soucy, P. M. Zimmerman, C. C. L. McCrory, *ACS Catal.* **2021**, *11*, 13203.
[68] J. Xu, S. Zhang, H. Liu, S. Liu, Y. Yuan, Y. Meng, M. Wang, C. Shen, Q. Peng, J. Chen, X. Wang, L. Song, K. Li, W. Chen, *Angew. Chem., Int. Ed.* **2023**, *62*, e202308044.
[69] F. Liu, J. Zhou, M. Sun, Z. Xu, H. Wang, N. Yao, Y. Wang, F. Hao, Y. Xiong, J. Wang, L. Guo, Q. Wa, G. Wang, X. Meng, M. Shao, C. Wang, H.-C. Chen, H. M. Chen, Y. Zhu, B. Huang, Z. Fan, *Angew. Chem., Int. Ed.* **2025**, *64*, e202504641.
[70] J. Wan, J. Yang, N. Yang, Y. Sun, C. Hu, Y. Zhao, X. Xu, H. Qi, X. Li, H. Zhang, *ACS Catal.* **2025**, *15*, 4507.
[71] J. Wan, Z. Zhao, H. Shang, B. Peng, W. Chen, J. Pei, L. Zheng, J. Dong, R. Cao, R. Sarangi, Z. Jiang, D. Zhou, Z. Zhuang, J. Zhang, D. Wang, Y. Li, *J. Am. Chem. Soc.* **2020**, *142*, 8431.
[72] J. Wan, Z. Zhao, H. Shang, B. Peng, W. Chen, J. Pei, L. Zheng, J. Dong, R. Cao, R. Sarangi, Z. Jiang, D. Zhou, Z. Zhuang, J. Zhang, D. Wang, Y. Li, *J. Am. Chem. Soc.* **2024**, *146*, 35010.
[73] Q. Li, L. Luo, X. Guo, R. Wang, J. Liu, W. Fan, Z. Feng, F. Zhang, *J. Am. Chem. Soc.* **2025**, *147*, 1884.
[74] L. Xie, Q. Hao, Y. Wu, H. Qin, L. Zheng, K. Liu, *Appl. Catal., B* **2025**, *375*, 125428.
[75] Z. Mei, K. Chen, Y. Tan, Q. Liu, Q. Chen, Q. Wang, X. Wang, C. Cai, K. Liu, J. Fu, M. Liu, *Chin. J. Catal.* **2024**, *62*, 190.
[76] Z.-Z. Wu, X.-L. Zhang, P.-P. Yang, Z.-Z. Niu, F.-Y. Gao, Y.-C. Zhang, L.-P. Chi, S.-P. Sun, J.-W. DuanMu, P.-G. Lu, Y.-C. Li, M.-R. Gao, *J. Am. Chem. Soc.* **2023**, *145*, 24338.
[77] P. Sebastián-Pascual, M. Escudero-Escribano, *J. Electroanal. Chem.* **2021**, *896*, 115446.
[78] B. Zhang, Z. Dai, Y. Chen, M. Cheng, H. Zhang, P. Feng, B. Ke, Y. Zhang, G. Zhang, *Nat. Commun.* **2024**, *15*, 2816.
[79] Y. Du, H. Lu, J. Wu, Y. Zou, Z.-F. Huang, J.-J. Zou, T. Mu, J. Gao, X.-D. Zhu, Y.-C. Zhang, *Angew. Chem., Int. Ed.* **2025**, *64*, e202420903.
[80] D. Richards, S. D. Young, B. R. Goldsmith, N. Singh, *Catal. Sci. Technol.* **2021**, *11*, 7331.
[81] H. H. Heenen, H. S. Pillai, K. Reuter, V. J. Bukas, *Nat. Catal.* **2024**, *7*, 847.
[82] M. Tan, Q. Hua, C. Zhang, H. Zhang, B. Huang, F. Feng, Y. Gao, X. Zhang, F. Zhang, N. Yang, Q. Huang, C. Ling, Z. Huang, Y. Ge, *Adv. Funct. Mater.* **2025**, 2510570.
[83] C. Jia, Y. Zhao, S. Song, Q. Sun, Q. Meyer, S. Liu, Y. Shen, C. Zhao, *Adv. Energy Mater.* **2023**, *13*, 2302007.
[84] Q. Cheng, S. Liu, Y. He, M. Wang, H. Ji, Y. Huan, T. Qian, C. Yan, J. Lu, *Nat. Commun.* **2025**, *16*, 3717.
[85] J. Sharp, A. Ciotti, H. Andrews, S. R. Udayasurian, M. García-Melchor, T. Li, *ACS Catal.* **2024**, *14*, 3287.
[86] Y. Pang, C. Su, L. Xu, Z. Shao, *Prog. Mater. Sci.* **2023**, *132*, 101044.
[87] H. Fei, J. Dong, D. Chen, T. Hu, X. Duan, I. Shakir, Y. Huang, X. Duan, *Chem. Soc. Rev.* **2019**, *48*, 5207.
[88] X. Long, F. Huang, T. Zhong, H. Zhao, P. Li, J. Fang, S. Tian, D. Shu, C. He, *Environ. Sci. Technol.* **2025**, *59*, 8555.
[89] T. Deng, S. Jia, C. Chen, J. Jiao, X. Chen, C. Xue, W. Xia, X. Xing, Q. Zhu, H. Wu, M. He, B. Han, *Angew. Chem., Int. Ed.* **2024**, *63*, e202313796.
[90] Z. Wang, W. Wang, Q. Yang, Y. Geng, Y. Du, K. Liu, Z. Wu, J. Lai, B. Li, H. Li, G. Zheng, L. Wang, *Adv. Energy Mater.* **2025**, *15*, 2405419.
[91] X. Su, F. Hong, Y. Fang, Y. Wen, B. Shan, *Angew. Chem., Int. Ed.* **2025**, *64*, e202422072.
[92] Y. Yu, Y. Sun, J. Han, Y. Guan, H. Li, L. Wang, J. Lai, *Energy Environ. Sci.* **2024**, *17*, 5183.
[93] Y. Han, Y. Wang, R. Xu, W. Chen, L. Zheng, A. Han, Y. Zhu, J. Zhang, H. Zhang, J. Luo, C. Chen, Q. Peng, D. Wang, Y. Li, *Energy Environ. Sci.* **2018**, *11*, 2348.
[94] Y. Zhao, Y. Ding, W. Li, C. Liu, Y. Li, Z. Zhao, Y. Shan, F. Li, L. Sun, F. Li, *Nat. Commun.* **2023**, *14*, 4491.
[95] X. Zhang, X. Zhu, S. Bo, C. Chen, K. Cheng, J. Zheng, S. Li, X. Tu, W. Chen, C. Xie, X. Wei, D. Wang, Y. Liu, P. Chen, S. P. Jiang, Y. Li, Q. Liu, C. Li, S. Wang, *Angew. Chem., Int. Ed.* **2023**, *62*, e202305447.
[96] H. Li, L. Xu, S. Bo, Y. Wang, H. Xu, C. Chen, R. Miao, D. Chen, K. Zhang, Q. Liu, J. Shen, H. Shao, J. Jia, S. Wang, *Nat. Commun.* **2024**, *15*, 8858.
[97] J. Mukherjee, S. Paul, A. Adalder, S. Kapse, R. Thapa, S. Mandal, B. Ghorai, S. Sarkar, U. K. Ghorai, *Adv. Funct. Mater.* **2022**, *32*, 2200882.
[98] Y. Huang, R. Yang, C. Wang, N. Meng, Y. Shi, Y. Yu, B. Zhang, *ACS Energy Lett.* **2022**, *7*, 284.
[99] L. Zhang, N. Jin, Y. Yang, X.-Y. Miao, H. Wang, J. Luo, L. Han, *Nano-Micro Lett.* **2023**, *15*, 228.
[100] C. Lv, C. Lee, L. Zhong, H. Liu, J. Liu, L. Yang, C. Yan, W. Yu, H. H. Hng, Z. Qi, L. Song, S. Li, K. P. Loh, Q. Yan, G. Yu, *ACS Nano* **2022**, *16*, 8213.
[101] J. Zhang, R. Yin, Q. Shao, T. Zhu, X. Huang, *Angew. Chem., Int. Ed.* **2019**, *58*, 5609.
[102] X. Wei, X. Wen, Y. Liu, C. Chen, C. Xie, D. Wang, M. Qiu, N. He, P. Zhou, W. Chen, J. Cheng, H. Lin, J. Jia, X.-Z. Fu, S. Wang, *J. Am. Chem. Soc.* **2022**, *144*, 11530.
[103] M. Mihaylov, K. Hadjiivanov, *Langmuir* **2002**, *18*, 4376.
[104] X. Song, X. Jin, T. Chen, S. Liu, X. Ma, X. Tan, R. Wang, L. Zhang, X. Tong, Z. Zhao, X. Kang, Q. Zhu, Q. Qian, X. Sun, B. Han, *Angew. Chem., Int. Ed.* **2025**, *64*, e202501830.
[105] N. Meng, Y. Huang, Y. Liu, Y. Yu, B. Zhang, *Cell Rep. Phys. Sci.* **2021**, *2*, 100378.
[106] X. Liu, J. Feng, X. Cheng, J. Zhang, J. Huo, D. Chen, A. Marcomini, Y. Li, Q. Xu, J. Lu, *Adv. Funct. Mater.* **2024**, *34*, 2400892.
[107] S. Banerjee, J. M. Gorham, P. Beccar-Varela, H. G. Hackbarth, M. A. Siegler, N. Drichko, J. T. Wright, N. M. Bedford, V. S. Thoi, *ACS Appl. Energy Mater.* **2023**, *6*, 9044.
[108] C. S. Gerke, Y. Xu, Y. Yang, G. D. Foley, B. Zhang, E. Shi, N. M. Bedford, F. Che, V. S. Thoi, *J. Am. Chem. Soc.* **2023**, *145*, 26144.
[109] Z. Wang, M. Wang, Q. Cheng, Y. He, S. Liu, J. Liu, X. Yuan, Y. Huan, T. Qian, C. Yan, *Angew. Chem., Int. Ed.* **2025**, *64*, e202416832.
[110] S. Paul, S. Sarkar, A. Adalder, A. Banerjee, U. K. Ghorai, *J. Mater. Chem. A* **2023**, *11*, 13249.
[111] Z. Shi, J. Guo, Z. Liu, Z. Xu, J. Yu, J. Ren, S. Chen, T. Liu, *Adv. Funct. Mater.* **2024**, *34*, 2406568.

[112] X. Qin, H. A. Hansen, K. Honkala, M. M. Melander, *Nat. Commun.* **2023**, *14*, 7607.
[113] S. K. Nabil, M. A. Muzibur Raghuman, K. Kannimuthu, M. Rashid, H. S. Shiran, M. G. Kibria, M. A. Khan, *Nat. Catal.* **2024**, *7*, 330.
[114] S. Yu, H. Yamauchi, S. Wang, A. Aggarwal, J. Kim, K. Gordiz, B. Huang, H. Xu, D. J. Zheng, X. Wang, H. Iriawan, D. Menga, Y. Shao-Horn, *Nat. Catal.* **2024**, *7*, 1000.
[115] B. Deng, M. Huang, X. Zhao, S. Mou, F. Dong, *ACS Catal.* **2022**, *12*, 331.
[116] W. Ge, L. Dong, C. Wang, Y. Zhu, Z. Liu, H. Jiang, C. Li, *ACS Catal.* **2024**, *14*, 10529.
[117] Y. Yao, E. P. Delmo, M. Shao, *Angew. Chem., Int. Ed.* **2025**, *64*, e202415894.
[118] Y. Guan, Y. Li, Z. Li, Y. Hou, L. Lei, B. Yang, *Adv. Mater.* **2025**, *37*, 2417567.
[119] J. Yang, J. Jiao, S. Liu, Y. Yin, Y. Cheng, Y. Wang, M. Zhou, W. Zhao, X. Tong, L. Jing, P. Zhang, X. Sun, Q. Zhu, X. Kang, B. Han, *Angew. Chem., Int. Ed.* **2024**, *63*, e202410145.
[120] J. M. Yoo, J. Ingenmey, M. Salanne, M. R. Lukatskaya, *J. Am. Chem. Soc.* **2024**, *146*, 31768.
[121] Z.-M. Zhang, T. Wang, Y.-C. Cai, X.-Y. Li, J.-Y. Ye, Y. Zhou, N. Tian, Z.-Y. Zhou, S.-G. Sun, *Nat. Catal.* **2024**, *7*, 807.
[122] M. C. O. Monteiro, F. Dattila, B. Hagedoorn, R. García-Muelas, N. López, M. T. M. Koper, *Nat. Catal.* **2021**, *4*, 654.
[123] K. Ye, G. Zhang, X.-Y. Ma, C. Deng, X. Huang, C. Yuan, G. Meng, W.-B. Cai, K. Jiang, *Energy Environ. Sci.* **2022**, *15*, 749.
[124] Y. Sun, J. Chen, X. Du, J. Cui, X. Chen, C. Wu, X. Yang, L. Liu, J. Ye, *Angew. Chem., Int. Ed.* **2024**, *63*, e202410802.
[125] W. Yan, T. Wu, J. Liu, Z. Zheng, M. Ma, *J. Am. Chem. Soc.* **2025**, *147*, 9990.
[126] B. Pan, J. Fan, J. Zhang, Y. Luo, C. Shen, C. Wang, Y. Wang, Y. Li, *ACS Energy Lett.* **2022**, *7*, 4224.
[127] J.-M. McGregor, J. T. Bender, A. S. Petersen, L. Cañada, J. Rossmeisl, J. F. Brennecke, J. Resasco, *Nat. Catal.* **2025**, *8*, 79.
[128] Z. Cui, A. J.-W. Wong, M. J. Janik, A. C. Co, *Sci. Adv.* **2025**, *11*, eadr6465.
[129] L. D. Chen, M. Urushihara, K. Chan, J. K. Nørskov, *ACS Catal.* **2016**, *6*, 7133.
[130] J. Feng, L. Wu, X. Song, L. Zhang, S. Jia, X. Ma, X. Tan, X. Kang, Q. Zhu, X. Sun, B. Han, *Nat. Commun.* **2024**, *15*, 4821.
[131] A. Murata, Y. Hori, *Bull. Chem. Soc. Jpn.* **2006**, *64*, 123.
[132] F.-Y. Chen, A. Elgazzar, S. Pecaut, C. Qiu, Y. Feng, S. Ashokkumar, Z. Yu, C. Sellers, S. Hao, P. Zhu, H. Wang, *Nat. Catal.* **2024**, *7*, 1032.
[133] S.-J. Qian, H. Cao, X.-M. Lv, J. Li, Y.-G. Wang, *J. Am. Chem. Soc.* **2025**, *147*, 21032.
[134] A. S. Fajardo, P. Westerhoff, S. Garcia-Segura, C. M. Sánchez-Sánchez, *Sep. Purif. Technol.* **2023**, *321*, 124233.
[135] W. Wen, S. Fang, Y. Zhou, Y. Zhao, P. Li, X.-Y. Yu, *Angew. Chem., Int. Ed.* **2024**, *63*, e202408382.
[136] W. Wu, Y. Wang, *J. Am. Chem. Soc.* **2025**, *147*, 11662.
[137] Y. Xie, P. Ou, X. Wang, Z. Xu, Y. C. Li, Z. Wang, J. E. Huang, J. Wicks, C. McCallum, N. Wang, Y. Wang, T. Chen, B. T. W. Lo, D. Sinton, J. C. Yu, Y. Wang, E. H. Sargent, *Nat. Catal.* **2022**, *5*, 564.
[138] Y. Chen, X.-Y. Li, Z. Chen, A. Ozden, J. E. Huang, P. Ou, J. Dong, J. Zhang, C. Tian, B.-H. Lee, X. Wang, S. Liu, Q. Qu, S. Wang, Y. Xu, R. K. Miao, Y. Zhao, Y. Liu, C. Qiu, J. Abed, H. Liu, H. Shin, D. Wang, Y. Li, D. Sinton, E. H. Sargent, *Nat. Nanotechnol.* **2024**, *19*, 311.
[139] F. Li, A. Thevenon, A. Rosas-Hernández, Z. Wang, Y. Li, C. M. Gabardo, A. Ozden, C. T. Dinh, J. Li, Y. Wang, J. P. Edwards, Y. Xu, C. McCallum, L. Tao, Z.-Q. Liang, M. Luo, X. Wang, H. Li, C. P. O'Brien, C.-S. Tan, D.-H. Nam, R. Quintero-Bermudez, T.-T. Zhuang, Y. C. Li, Z. Han, R. D. Britt, D. Sinton, T. Agapie, J. C. Peters, E. H. Sargent, *Nature* **2020**, *577*, 509.
[140] J. E. Huang, F. Li, A. Ozden, A. Sedighian Rasouli, F. P. García de Arquer, S. Liu, S. Zhang, M. Luo, X. Wang, Y. Lum, Y. Xu, K. Bertens, R. K. Miao, C.-T. Dinh, D. Sinton, E. H. Sargent, *Science* **2021**, *372*, 1074.
[141] Z. Wang, Y. Li, X. Zhao, S. Chen, Q. Nian, X. Luo, J. Fan, D. Ruan, B.-Q. Xiong, X. Ren, *J. Am. Chem. Soc.* **2023**, *145*, 6339.
[142] Y. Zhao, L. Hao, A. Ozden, S. Liu, R. K. Miao, P. Ou, T. Alkayyali, S. Zhang, J. Ning, Y. Liang, Y. Xu, M. Fan, Y. Chen, J. E. Huang, K. Xie, J. Zhang, C. P. O'Brien, F. Li, E. H. Sargent, D. Sinton, *Nat. Synth.* **2023**, *2*, 403.
[143] J. Martínez, A. Ortiz, I. Ortiz, *Appl. Catal., B* **2017**, *207*, 42.
[144] T. Hu, C. Wang, M. Wang, C. M. Li, C. Guo, *ACS Catal.* **2021**, *11*, 14417.
[145] Y. Lv, S.-W. Ke, Y. Gu, B. Tian, L. Tang, P. Ran, Y. Zhao, J. Ma, J.-L. Zuo, M. Ding, *Angew. Chem., Int. Ed.* **2023**, *62*, e202305246.
[146] R. Zhang, C. Li, H. Cui, Y. Wang, S. Zhang, P. Li, Y. Hou, Y. Guo, G. Liang, Z. Huang, C. Peng, C. Zhi, *Nat. Commun.* **2023**, *14*, 8036.
[147] M. Wang, K. Torbensen, D. Salvatore, S. Ren, D. Joulié, F. Dumoulin, D. Mendoza, B. Lassalle-Kaiser, U. Işci, C. P. Berlinguette, M. Robert, *Nat. Commun.* **2019**, *10*, 3602.
[148] P. Li, Z. Jin, Z. Fang, G. Yu, *Energy Environ. Sci.* **2021**, *14*, 3522.
[149] V. J. Ovalle, Y.-S. Hsu, N. Agrawal, M. J. Janik, M. M. Waegele, *Nat. Catal.* **2022**, *5*, 624.
[150] Y. Xu, Z. Xia, W. Gao, H. Xiao, B. Xu, *Nat. Catal.* **2024**, *7*, 1120.
[151] F. Zhang, W. Zhang, J. A. Yuwono, D. Wexler, Y. Fan, J. Zou, G. Liang, L. Sun, Z. Guo, *Nat. Commun.* **2024**, *15*, 3393.
[152] Q. Wu, Z. J. Xu, *Angew. Chem Int. Ed.* **2025**, e202505022
[153] X. Tu, X. Zhu, S. Bo, X. Zhang, R. Miao, G. Wen, C. Chen, J. Li, Y. Zhou, Q. Liu, D. Chen, H. Shao, D. Yan, Y. Li, J. Jia, S. Wang, *Angew. Chem., Int. Ed.* **2024**, *63*, e202317087.
[154] J. T. Bender, A. S. Petersen, F. C. Østergaard, M. A. Wood, S. M. J. Heffernan, D. J. Milliron, J. Rossmeisl, J. Resasco, *ACS Energy Lett.* **2023**, *8*, 657.
[155] C. S. Gerke, M. Klenk, P. Zapol, V. S. Thoi, *ACS Catal.* **2023**, *13*, 14540.
[156] M. Xu, F. Wu, Y. Zhang, Y. Yao, G. Zhu, X. Li, L. Chen, G. Jia, X. Wu, Y. Huang, P. Gao, W. Ye, *Nat. Commun.* **2023**, *14*, 6994.
[157] B. Sun, Z. Li, D. Xiao, H. Liu, K. Song, Z. Wang, Y. Liu, Z. Zheng, P. Wang, Y. Dai, B. Huang, A. Thomas, H. Cheng, *Angew. Chem., Int. Ed.* **2024**, *63*, e202318874.
[158] Y. Chen, Y. Liu, S. Hu, D. Wu, M. Zhang, Z. Cheng, *Sci. Total Environ.* **2024**, *913*, 169722.
[159] W.-G. Cui, F. Gao, G. Na, X. Wang, Z. Li, Y. Yang, Z. Niu, Y. Qu, D. Wang, H. Pan, *Chem. Soc. Rev.* **2024**, *53*, 10253.
[160] N. Govindarajan, A. Xu, K. Chan, *Science* **2022**, *375*, 379.
[161] Q. Wu, C. Dai, F. Meng, Y. Jiao, Z. J. Xu, *Nat. Commun.* **2024**, *15*, 1095.
[162] A. P. Atkins, A. J. J. Lennox, *Curr. Opin. Electrochem.* **2024**, *44*, 101441.
[163] F. Rocha, Q. de Radiguès, G. Thunis, J. Proost, *Electrochim. Acta* **2021**, *377*, 138052.
[164] T. Liu, J. Wang, X. Yang, M. Gong, *J. Energy Chem.* **2021**, *59*, 69.
[165] Y. Jännsch, J. J. Leung, M. Hämmerle, E. Magori, K. Wiesner-Fleischer, E. Simon, M. Fleischer, R. Moos, *Electrochem. Commun.* **2020**, *121*, 106861.
[166] Z. Li, L. Wang, T. Wang, L. Sun, W. Yang, *J. Am. Chem. Soc.* **2023**, *145*, 20655.
[167] J. C. Bui, C. Kim, A. J. King, O. Romiluyi, A. Kusoglu, A. Z. Weber, A. T. Bell, *Acc. Chem. Res.* **2022**, *55*, 484.
[168] J. Zhang, S. Xia, Y. Wang, J. Wu, Y. Wu, *iScience* **2024**, 110005.
[169] Z. Masaud, G. Liu, L. E. Roseng, K. Wang, *Chem. Eng. J.* **2023**, *475*, 145882.
[170] X. Wu, X. Li, J. Lv, X. Lv, A. Wu, Z. Qi, H. B. Wu, *Small* **2024**, *20*, 2307637.
[171] X. Li, C. Liu, B. Li, J. Li, S. Wang, X. Huang, *Chem. A Eur. J.* **2025**, *31*, e202501156.
[172] K. Wan, X. Jiang, X.-P. Li, Z. Cao, Z.-H. He, W. Wang, H. Wang, X. Lai, Z.-T. Liu, *Green Chem.* **2025**, *27*, 6027.
[173] Q. Hu, W. Zhou, S. Qi, Q. Huo, X. Li, M. Lv, X. Chen, C. Feng, J. Yu, X. Chai, H. Yang, C. He, *Nat. Sustainability* **2024**, *7*, 442.
[174] M. He, Y. Wu, R. Li, Y. Wang, C. Liu, B. Zhang, *Nat. Commun.* **2023**, *14*, 5088.
[175] C. A. Obasanjo, G. Gao, B. N. Khiarak, T. H. Pham, J. Crane, C.-T. Dinh, *Energy Fuels* **2023**, *37*, 13601.
[176] F. Xue, X. Lai, Y. Xu, *ChemCatChem* **2024**, *16*, e202400590.
[177] B. A. Yusuf, W. Yaseen, S. Meng, J. Xie, F. O. Fapohunda, R. Nankya, A. I. Muhammad, M. Xie, Y. Xu, *Coord. Chem. Rev.* **2023**, *492*, 215273.
[178] Q. Lei, L. Huang, J. Yin, B. Davaasuren, Y. Yuan, X. Dong, Z.-P. Wu, X. Wang, K. X. Yao, X. Lu, Y. Han, *Nat. Commun.* **2022**, *13*, 4857.
[179] A. R. Woldu, Z. Huang, P. Zhao, L. Hu, D. Astruc, *Coord. Chem. Rev.* **2022**, *454*, 214340.
[180] J. Timoshenko, A. Bergmann, C. Rettenmaier, A. Herzog, R. M. Arán-Ais, H. S. Jeon, F. T. Haase, U. Hejral, P. Grosse, S. Kühl, E. M. Davis, J. Tian, O. Magnussen, B. Roldan Cuenya, *Nat. Catal.* **2022**, *5*, 259.
[181] S. Yang, Y. Shen, X. Mao, C. Li, Z. Liu, B. Wang, D. Zhu, H. Li, C. Li, *AIChE J.* **2025**, *71*, e18829.
[182] R. Zhao, Q. Yan, L. Lu, L. Yu, H. Chen, T. Yan, L. Liu, J. Xi, *ACS Catal.* **2024**, *14*, 17046.
[183] Y. Qu, T. Dai, Y. Cui, G. Ding, Y. Zhu, Z. Wang, Q. Jiang, *Small* **2024**, *20*, 2308246.
[184] Y. Bu, C. Wang, W. Zhang, X. Yang, J. Ding, G. Gao, *Angew. Chem., Int. Ed.* **2023**, *62*, e202217337.
[185] Z. Zhang, B. Ge, M. Liu, T. Yang, S. Wang, Y. Liu, Y. Yang, S. Gao, *ACS Appl. Mater. Interfaces* **2025**, *17*, 26501.

[186] C. Guo, S. Liu, Z. Chen, B. Li, L. Chen, C. V. Singh, B. Liu, Q. Mao, *Chem. Commun.* **2021**, *57*, 1384.
[187] C. Kim, L.-C. Weng, A. T. Bell, *ACS Catal.* **2020**, *10*, 12403.
[188] R. Casebolt DiDomenico, K. Levine, C. Bundschu, L. Reimanis, T. Arias, T. Hanrath, *ACS Catal.* **2024**, *14*, 785.
[189] Y. Huang, C. He, C. Cheng, S. Han, M. He, Y. Wang, N. Meng, B. Zhang, Q. Lu, Y. Yu, *Nat. Commun.* **2023**, *14*, 7368.
[190] Y. Xiong, Y. Wang, J. Zhou, F. Liu, F. Hao, Z. Fan, *Adv. Mater.* **2024**, *36*, 2304021.
[191] T. Irrgang, R. Kempe, *Chem. Rev.* **2020**, *120*, 9583.
[192] H. S. Jeon, J. Timoshenko, C. Rettenmaier, A. Herzog, A. Yoon, S. W. Chee, S. Oener, U. Hejral, F. T. Haase, B. Roldan Cuenya, *J. Am. Chem. Soc.* **2021**, *143*, 7578.
[193] X. Liu, Y. Jiao, Y. Zheng, M. Jaroniec, S.-Z. Qiao, *Nat. Commun.* **2022**, *13*, 5471.
[194] W. Qiu, S. Qin, Y. Li, N. Cao, W. Cui, Z. Zhang, Z. Zhuang, D. Wang, Y. Zhang, *Angew. Chem., Int. Ed.* **2024**, *63*, e202402684.
[195] R. A. Talmazan, J. Refugio Monroy, F. del Río-Portilla, I. Castillo, M. Podewitz, *ChemCatChem* **2022**, *14*, e202200662.
[196] Y. Gu, Q. Ma, X. Li, X. Ye, R. Zhang, J. Liu, X. Luo, Q. Yao, Y. Cao, *Appl. Surf. Sci.* **2025**, *692*, 162740.
[197] S. Ringe, E. L. Clark, J. Resasco, A. Walton, B. Seger, A. T. Bell, K. Chan, *Energy Environ. Sci.* **2019**, *12*, 3001.

Manuscript received: June 29, 2025
Revised manuscript received: July 27, 2025
Version of record online: